

# Creation of a Geant4 Muon Tomography Package for Imaging of Nuclear Fuel in Dry Cask Storage

---

Fuel Cycle Research and Development

Lefteri Tsoukalas  
Purdue University

Dan Vegas, Federal POC  
Mike Miller, Technical POC

# PURDUE UNIVERSITY

---

School of Nuclear Engineering

400 Central Drive

West Lafayette, IN 47907

## FINAL REPORT

<b>Project Title:</b>	Creation of a Geant4 Muon Tomography Package for Imaging of Nuclear Fuel in Dry Cask Storage (13-5376)
<b>Institution:</b>	School of Nuclear Engineering, Purdue University
<b>Workscope:</b>	FC-3
<b>PICSNE Workpackage:</b>	NU-13-IN-PU_0301-03
<b>Project Period:</b>	December 1, 2013 to November 30, 2015
<b>Principal Investigator:</b>	Prof. Lefteri H. Tsoukalas, 765-496-9696, tsoukala@purdue.edu

West Lafayette, IN  
March 2016

<b>PURDUE UNIVERSITY</b>			Document No:		
<b>School of Nuclear Engineering</b>			Document Title: Final Report		
<b>DOCUMENT REVISION SHEET</b>					
Revision	Description of Revision	Date	Initials		Notes
			Prepared	Reviewed	
1	Original Version	March 2016	SC	LHT	For submission to NEUP

## Executive Summary

This is the final report of the NEUP project “Creation of a Geant4 Muon Tomography Package for Imaging of Nuclear Fuel in Dry Cask Storage”, DE-NE0000695. The project started on December 1, 2013 and this report covers the period December 1, 2013 through November 30, 2015. The project was successfully completed and this report provides an overview of the main achievements, results and findings throughout the duration of the project. Additional details can be found in the main body of this report and on the individual Quarterly Reports and associated Deliverables of the project, uploaded in PICS-NE.

### Status:

The research activities have been performed according to the schedule planning. All Tasks been completed and all deliverables have been submitted in PICS-NE according to the schedule. Quad charts and quarterly reports including attachments from publications have also been submitted successfully.

### Project Team:

The project team comprised of two Nuclear Engineering Professors (PI and co-PI) and three PhD graduate students.

### Milestones:

All milestones have been completed and submitted in PICS-NE.

### Main achievements:

Main results and findings have been submitted to a number of conferences and journals. The project team participated in various research competition and local community events. In particular:

1. Participation to Sigma Xi Research Competition 2014
  - *Best Poster Award*
2. Participation to BigTen Grad Expo
3. Participation to Homeland Security annual meeting

4. Participation and paper contribution to ANS winter meeting 2014
5. Participation and paper contribution to ANS annual meeting 2015
6. Participation and paper contribution to ANS annual meeting 2016
7. Participation and poster contribution to Waste Management Symposium 2015
8. Participation and poster contribution to Waste Management Symposium 2016
9. Participation and poster contribution to Sigma Xi Research Competition 2016
10. Participation and paper contribution to ICAPP conference 2016

➤ *Best Paper Award*

11. Three of the project team graduate students, Phil Forsberg, Bryan Sims and Stylianos Chatzidakis, were awarded the prestigious Outstanding Teaching, Outstanding Service and Outstanding Research Awards from Purdue's College of Engineering.
12. One of the project team graduate student, Stylianos Chatzidakis, was awarded the prestigious Roy G. Post Foundation scholarship for contributions to nuclear waste management.
13. Two of the project team graduate students, Phil Forsberg and Bryan Sims, were awarded the prestigious NNSA Graduate Fellowship.

Main results and findings:

In the duration of this project, a methodology was developed to demonstrate the applicability of muons for nuclear nonproliferation monitoring of spent nuclear fuel dry casks. Purpose is to use muons to differentiate between spent nuclear fuel dry casks with different amounts of loading, not feasible with any other technique. Muon scattering and transmission are used to perform monitoring and imaging of the stored contents of dry casks loaded with spent nuclear fuel. It is shown that one missing fuel assembly can be distinguished from a fully loaded cask with a small overlapping between the scattering distributions with 300,000 muons or more. A Bayesian monitoring algorithm was derived to allow differentiation of a fully loaded dry cask from one with a fuel assembly missing in the order of minutes and zero probability of error. Muon scattering and transmission are used to reconstruct the stored contents of sealed dry casks from muon measurements. A combination of muon scattering and muon transmission imaging can improve resolution and a missing fuel assembly can be identified for vertical and horizontal dry

casks. The apparent separation of the images reveals that the muon scattering and transmission can be used as discrimination between casks, satisfying the diversion criteria set by IAEA.

### Publications:

#### Peer-reviewed journals:

1. S. Chatzidakis, C.K. Choi, L.H. Tsoukalas (2016). *Interaction of Cosmic Ray Muons with Spent Nuclear Fuel Dry Casks and Determination of Lower Detection Limit*. Nuclear Instruments and Methods in Physics Research A, under review.
2. S. Chatzidakis, C.K. Choi, L.H. Tsoukalas (2016). *Analysis of Spent Nuclear Fuel Imaging Using Multiple Coulomb Scattering of Cosmic Muons*. IEEE Transactions on Nuclear Science, under review.
3. S. Chatzidakis, S. Chrysikopoulou, L.H. Tsoukalas (2015). *Developing a cosmic ray muon sampling capability for muon tomography and monitoring applications*. Nuclear Instruments and Methods in Physics Research A, Vol. 804, 33-42.
4. S. Chatzidakis, P. Forsberg, L.H. Tsoukalas (2014). *Artificial neural networks and chaos dynamics for signal encryption*. Nuclear Technology, Vol. 192 (1), 61-73.

#### Conferences:

1. S. Chatzidakis, C.K. Choi, L.H. Tsoukalas (2016). *Investigation of imaging spent nuclear fuel dry casks using cosmic ray muons*. Transactions of the American Nuclear Society, to appear.
2. S. Chatzidakis, L.H. Tsoukalas (2016). *Theoretical investigation of spent nuclear fuel monitoring using cosmic ray muons*. International Congress on Advances in Nuclear Power Plants, April 17-20, San Francisco, CA.
3. S. Chatzidakis, P.T. Forsberg, B.T. Sims, L.H. Tsoukalas (2015). *Monte Carlo simulations of cosmic ray muons for dry cask monitoring*. Transactions of the American Nuclear Society, Vol. 112, 534-536.

4. S. Chatzidakis, M. Alamaniotis, L.H. Tsoukalas (2014). *A Bayesian approach to monitoring spent fuel using cosmic ray muons*. Transactions of the American Nuclear Society, Vol. 111, 369-370.

Dissertations:

1. S. Chatzidakis, Cosmic Ray Muons for Spent Nuclear Fuel Monitoring, PhD Dissertation, School of Nuclear Engineering, Purdue University, 2016.

## **Final Report**



## CHAPTER 1. INTRODUCTION

High energy cosmic rays continuously penetrate into the Earth's magnetosphere, collide with atoms and molecules in the upper layers of the atmosphere and generate a cascade of secondary rays and relativistic particles. This process produces pions and kaons which decay almost instantaneously to elementary particles called muons and give rise to a considerable muon flux that reaches sea level. Muons, frequently called "cosmic ray muons" when generated naturally in the atmosphere by cosmic radiation, are charged particles, having approximately 200 times the mass of electron, and reach ground level at an approximate rate of  $10,000 \text{ particles m}^{-2} \text{ min}^{-1}$  [1]. Muons are the dominant charged particles arriving at sea level, the rest being electrons, positrons and photons from cascade events, and due to their very high momentum can penetrate deeply underground [2]. The muon spectrum has been experimentally measured and covers a wide range of energies, from 0.2 to 20,000 GeV and zenith angles from  $0^\circ$  to  $89^\circ$ . The very large energies of individual cosmic ray muons account for their ability to penetrate large thicknesses of high density materials allowing the distribution of material within the object to be inferred from muon measurements. Cosmic ray muons have been the subject of rigorous investigation over the years for a number of monitoring and imaging applications including archaeology, volcano imaging, material identification and medica

diagnosis. E. P. George first used muon attenuation to infer rock depth covering underground tunnels [3]. L. Alvarez placed a muon detector in a chamber beneath the Second Pyramid of Egypt and measured cosmic ray muon flux attenuation in an effort to determine presence and location of hidden chambers [4]. More recently, cosmic ray muons have been shown to have the potential to allow for non-destructive assessment of nuclear material accountancy with the aim to independently verify and identify undeclared nuclear materials hidden in cargo containers [5] or fuel pellets, fuel rods and fuel assemblies stored within sealed dense containers [6]. Recently it was demonstrated that the subsequent scattering and transmission of muons can provide a measurable signal about the structural and chemical composition of the stored materials [4-8]. Novel applications of cosmic ray muons have been proposed for medical examination of comatose patients towards tissue density monitoring and determination of the molten nuclear fuel location in nuclear reactors having suffered from the effects of a severe accident similar to the one happened in Chernobyl and Fukushima [8].

The recent exponential expansion dry storage of spent nuclear fuel assemblies stored in heavily shielded casks and the safeguards requirement to maintain continuity of knowledge calls for innovative technologies to fill this critical gap. Spent nuclear fuel contains significant quantities of plutonium that if retrieved could be used for non-peaceful uses and must satisfy stringent safety, security and environmental criteria. The International Atomic Energy Agency (IAEA) through its safeguards program has established criteria to verify that nuclear material is not diverted from peaceful uses.

Table 1-1 shows the significant quantity of nuclear material and the time required for

detection [9]. The significant quantity for spent nuclear fuel is 8 kg of Pu and any diversion has to be detected within 3 months.

Table 1-1. IAEA target criteria for nonproliferation of nuclear material [9].

Item	Quantity (kg)	Form	Time to detect (months)
$^{235}\text{U}$	75	LEU (<20%)	12
$^{235}\text{U}$	25	HEU ( $\geq 20\%$ )	1
Pu	8	Fresh fuel	1
Pu	8	Spent fuel	3
$^{233}\text{U}$	8	Fresh fuel	1
$^{233}\text{U}$	8	Spent fuel	3

Monitoring spent nuclear fuel stored in shielded dry casks using cosmic ray muons has the potential to allow for non-destructive assessment of the stored fuel assemblies, investigate whether the stored content agrees with the declared content, minimize the risks of nuclear proliferation and reduce potential homeland threats [10]. Over the past five decades approximately 65,000 metric tons of uranium (MTU) have been generated by the 100+ nuclear reactors in the U.S., 75% of which is stored in used fuel pools while the remaining 25% is under dry storage conditions. As of today, no permanent repository exists and all studies and work at Yucca Mountain has been suspended resulting in increased spent nuclear fuel accumulation at reactor sites. After the spent nuclear fuel has been placed inside the dry cask, direct visual inspection is not possible [6]. Conventional methods for examining the interior of materials e.g., photons, are limited – maximum mean free path is approximately  $25 \text{ g/cm}^2$  for all materials resulting to less than 2 cm penetration in lead [5]. Increasing the photon energy does not increase penetrating distance due to an increase in pair production phenomena [11]. Similarly, electrons cannot penetrate far into matter due to large momentum transfers and radiation emission

(Bremsstrahlung). For example, 1 GeV electrons can penetrate water only within 1 m and commercially available portable Betatrons can generate electron with energies less than 10 MeV. Protons have been shown to penetrate several meters in dense materials and their potential has been demonstrated for large vessel imaging [11]. However, production of high-energy protons requires large, expensive and immovable accelerators. Cosmic ray muons present certain advantages over the previously mentioned particles and ionizing radiation. Among other, muons have the ability to penetrate high density materials, are freely available, no radiological sources are required and consequently there is a total absence of any artificial radiological dose.

In this work, the applicability of muons for monitoring spent nuclear fuel stored within dry casks is investigated. Muon scattering and transmission are used to perform monitoring and imaging of the stored contents of dry casks loaded with spent nuclear fuel. Cosmic ray muons passing through matter lose energy from inelastic collisions with electrons and are deflected from nuclei due to multiple Coulomb scattering. The strong dependence of scattering on atomic number  $Z$  and the simplicity of measuring muon scattering angles indicate that multiple Coulomb scattering could be an excellent candidate for spent nuclear fuel monitoring and cosmic ray muons can play a central role in monitoring spent nuclear fuel without the limitations of the existing techniques.

### Report outline

Chapter 2 presents an overview of spent nuclear fuel and dry cask characteristics. A brief description of the spent nuclear fuel historical background is discussed to present the reasons that necessitate spent nuclear fuel monitoring. The main characteristics and

components of wet and dry storage, future trends and the types of current dry cask designs are presented. Chapter 2 includes a brief introduction to cosmic rays muons and their properties, their generation from cosmic rays and their interactions with matter, i.e., ionization and multiple Coulomb scattering.

In Chapter 3 information pertinent to muon-matter interactions is presented. A description of the energy loss and multiple Coulomb scattering that occur when muons pass through matter are presented and discussed. Details on GEANT4 simulations of commercial dry casks, validation results and estimation of the scattering variance are described together with the derivation of the scattering variance distribution and the properties of the estimator. Chapter 3 concludes with simulations of muon-dry cask interactions performed to investigate the asymptotic behavior of the scattering variance and the determination of a decision boundary between a fully loaded dry cask and one with a fuel assembly missing.

In Chapter 4 the Bayesian framework for monitoring spent nuclear fuel dry casks is presented. In this chapter, a monitoring algorithm which minimizes the risk of making an incorrect decision based on Bayesian principles is derived. The algorithm performance is evaluated in terms of error, miss and false alarm rates. The Receiver Operating Characteristic and Minimax curves are generated and comparison with non-probabilistic learning algorithms is performed. The Bayesian algorithm can identify a dry cask with a fuel assembly missing in the order of minutes and zero probability of error. The dependence of the lower detection limit on the number of muons measured is investigated.

Chapter 5 provides the framework for imaging spent nuclear fuel dry casks using muon scattering and transmission. The Point-of-Closest-Approach algorithm is used to reconstruct the stored contents of sealed dry casks from muon measurements. A combination of PoCA and muon transmission imaging can improve resolution a missing fuel assembly can be identified for vertical and horizontal dry casks.

Finally, the main conclusions of the material presented are summarized in Chapter 6.

Supportive material is available in the Appendix.

## CHAPTER 2. BACKGROUND

This chapter provides details on spent nuclear fuel characteristics and cosmic ray muons. A brief description on the spent nuclear fuel historical background is discussed to present the reasons that necessitate spent nuclear fuel monitoring. Sections 2.1 and 2.2 provide the main characteristics and components of commercial dry storage and future trends. The types and characteristics of commercial dry cask designs are evaluated and analyzed in Section 2.2. A brief introduction to cosmic rays muons, their properties and generation from cosmic rays, muon spectrum and existing muon detectors appears in Section 2.3. Finally, this chapter concludes with a review of the previous work on the use of muons for monitoring and imaging applications and a summary in Sections 2.4 and 2.5, respectively.

### a. Spent nuclear fuel

#### i. Historical background

Spent nuclear fuel management has a long history of controversy and is at the center of public debate about the future of nuclear energy in the United States. Since the early 1950s, based on recommendations by U.S. Atomic Energy Commission and National Academy of Sciences [12], efforts have been made to design and construct a geological disposal facility to host spent nuclear fuel from operating reactors.

A number of salt mines have been rigorously investigated, including an area in New Mexico, which eventually hosted the Waste Isolation Pilot Plant (WIPP), the first facility to receive nuclear waste shipments. However, the WIPP was eventually limited only to defense related nuclear waste [12]. Other potential candidates included areas in Michigan, Texas, Utah and Nevada. Up to this point, nuclear industry, utilities and the public were convinced that spent nuclear fuel will remain in spent fuel pools in operating reactors for only a few years until a final disposal facility is built. Under this assumption, spent nuclear fuel pools were designed with limited capacity and no provisions for dry on-site storage were made. Concerns on nuclear proliferation resulted in abandoning the reprocessing option and delays in identifying a permanent geological disposal site resulted in spent fuel pool capacity shortage at operating reactors. Lack of funding, technical difficulties and strong political opposition ultimately demonstrated that nuclear waste management can become a very problematic issue to deal with [12].

In 1982, the Nuclear Waste Policy Act (NWPA) was the outcome of an effort to address the nuclear waste problem and the upcoming shortage of spent nuclear fuel pool capacity. The NWPA was revisited and an amendment act in 1987 designated the Yucca Mountain, located on Federal land in Nye County in southern Nevada, approximately 160 km northwest of Las Vegas, as the sole site to be considered for geological disposition of spent nuclear fuel. Research studies continued on the selected site of Yucca Mountain and a license application was submitted to the NRC in 2008 which was withdrawn a year later. As of today, no permanent repository exists and all studies and work at Yucca Mountain have been suspended [13-16].



## ii. Spent nuclear fuel and projections

The current fleet of commercial nuclear reactors in the U.S. utilizes nuclear fuel in the form of uranium dioxide ( $\text{UO}_2$ ) cylindrical pellets in various degrees of enrichment (i.e., 3-5%) and enclosed in cylindrical rods made of zirconium alloy. A fuel assembly consists of an array of fuel rods (i.e., zircalloy and  $\text{UO}_2$ ) rectangular in shape. PWR assemblies are square arrays of 15x15 or 17x17 fuel rods [17]. BWR assemblies are smaller, 8x8 rods. PWR and BWR reactor cores contain more than 200 and 700 nuclear fuel assemblies, respectively.

Spent nuclear fuel consists of nuclear fuel that has been discharged from the reactor core. Fresh fuel assemblies (i.e., not irradiated) do not require cooling or radiation shielding and can be moved using cranes in open air. However, spent nuclear fuel contains significant quantities of fission products and emits radiation, gammas and neutrons. Heat is generated from the radioactive decay of the fission products. Spent nuclear fuel has to be kept under continuous cooling for a sufficient amount of time, usually more than 5 years, to dissipate decay heat and reduce radiation levels. About one-third of the core is discharged to the spent fuel pool every 18-24 months, depending on the selected fuel cycle scheme. When spent fuel pools reach their storage capacity, reactor operators need to provide additional storage capacity to allow plant operation under NRC license. As a result, many utilities have created dry storage facilities, the so-called Independent Spent Fuel Storage Installations (ISFSIs). The facilities have provisions for storing dry storage containers, dry casks, loaded with spent nuclear fuel assemblies.

There is a steady increase in the volume of spent nuclear fuel stored on-site (at reactor) as currently there is no permanent disposal option. In the aftermath of Fukushima events, which demonstrated the vulnerabilities of spent fuel pools, a trend towards increased use of dry cask storage is apparent, as shown in Figure 2-1.

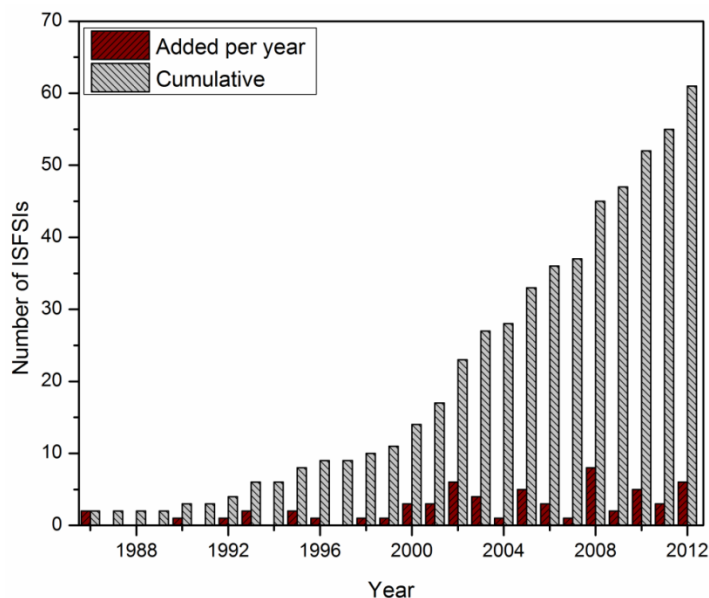


Figure 2-1. Number of dry storage facilities over time [12].

Current number of dry cask storage containers in utilities is approximately 1,200 and projections by EPRI show that by 2020 more than 2,400 dry casks will have been installed [12]. Figure 2-2 shows that the need for on-site dry cask storage will rise sharply in the next years. Beginning of 2009 there existed approximately 60,000 MTU (approximately 210,000 spent fuel assemblies) in storage. 47,500 MTU were in wet storage and 13,000 MTU stored in ~1200 dry casks at 44 plant sites in 31 states [15]. This inventory will increase to 130,000 MTU (~420,000 spent fuel assemblies) by 2040

even if no new nuclear power plants are built. Over 7,000 casks will be required by 2040.

By 2020 essentially all plants will be required to have ISFSIs to store fuel.

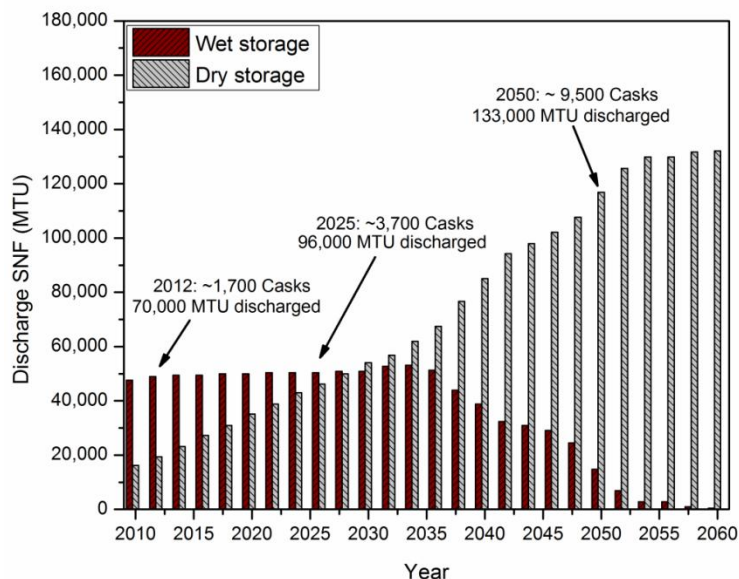


Figure 2-2. Projections over wet and dry storage [12].

#### b. Dry cask storage

A variety of dry cask designs have been produced for use in ISFSIs over the years. These can be classified in three categories (i) vertical metal storage casks, (ii) vertical metal canisters shielded in vertical concrete or metal overpack and, (iii) horizontal metal canisters shielded in concrete modules [16]. In the early 1980s, during the initial development stage of the dry storage concept, spent nuclear fuel assemblies were stored in casks without canister, a method known as “bare fuel”. These casks were intended only for storage and should spent nuclear fuel assemblies needed to be transported off-site or the cask was damaged, then fuel assemblies had to be unloaded one by one into a spent fuel pool and then stored into another cask. This process was eventually proven time

consuming and cost ineffective, especially for decommissioned reactors where no spent nuclear fuel pools were available. This problem is now mitigated with the design and development of canister-based storage systems. Such storage systems consist of a canister that provides structural support for the spent nuclear fuel assemblies and an overpack where the loaded canister is placed. Dual Purpose Canisters (DPC) are licensed for storage and transportation and Multi-Purpose Canister (MPC) systems are currently under investigation with the intention to be used in all stages of waste management without the need to remove the fuel assemblies from the canister, i.e., on-site storage, transportation and disposal [14]. Commercial dry casks vary in design and characteristics depending on cask manufacturer and can provide space for 24-32 PWR or 56-86 BWR assemblies. They can be stored either vertically or horizontally and weigh more than 100 tons when loaded (fuel assemblies weigh approximately 0.5 – 1 MTU each). Dry casks in vertical and horizontal orientation are schematically shown in Figure 2-3 and the main components are illustrated: fuel assemblies, canister and overpack.

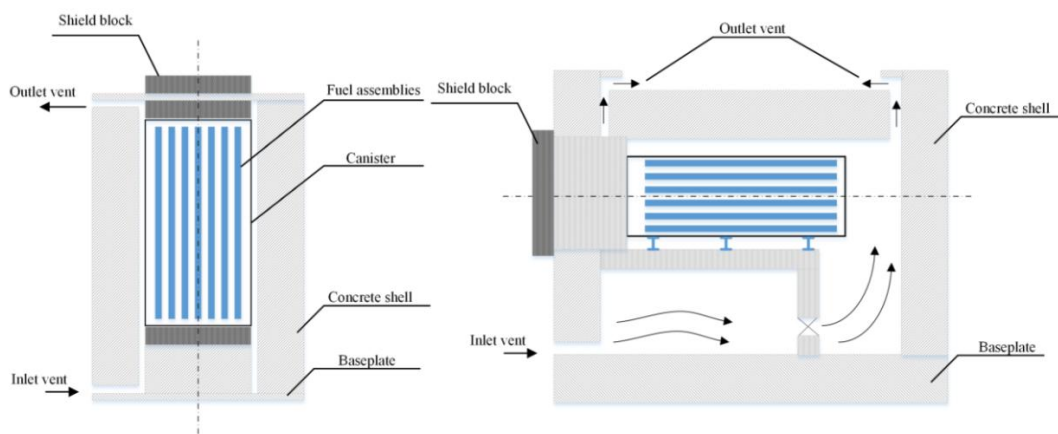


Figure 2-3. Typical vertical and horizontal dry cask storage configurations [14].

During transfer of spent nuclear fuel to a dry cask, the canister is placed inside the pool, spent nuclear fuel is placed inside the canister and after drainage and vacuum drying the canister is filled with an inert gas such as helium. The canister lid is welded and tested to ensure leak-tightness and is then placed in the overpack for final storage. A fuel basket within the canister provides structural support to the fuel assemblies, criticality control and improved heat transfer. The canister, approximately 1-1.5 cm thick, serves as a containment to prevent contamination in case of fuel cladding rupture. The overpack provides radiation shielding, structural and protection of the canister against environmental conditions. The space between the overpack and the canister allows for air circulation and heat dissipation to the environment. A stored container is approximately 6 meters in height and 2.5 meters in diameter. More than 20 dry cask design models that fall within the above three categories have been approved by NRC for use in ISFSIs [18]. Five vendors are currently supply dry storage casks to the U.S. (i) Holtec International, (ii) NAC International, (iii) Transnuclear Inc., (iv) General Nuclear Systems Inc. (GNSI/GNB) and, (v) BNG Fuel Solutions Corp. A classification of the corresponding design models is shown in Figure 2-4 and the main characteristics of each model are presented in Table 2-1. Dimensions and main components are shown in Tables 2-2 and 2-3. A brief description (indicative and not exhaustive, for facilitating the subsequent discussion only) of the main characteristics of commercial dry casks is presented below.

#### i. VSC-24

The VSC-24 (Ventilated Storage Cask) is a storage only, vertically oriented cask with 24 PWR SNF assemblies storage capacity. It consists of a ventilated concrete cask and a

multi-assembly sealed basket. The cask body is a steel reinforced concrete cylindrical structure with an internal carbon steel liner with overall external dimensions ranging from 5.0 to 5.72 meters height and 3.35 meters outer diameter. Thickness and inner diameter are 0.74 and 1.79 meters, respectively. The cask body ensures the necessary functions of structural support, radiation shielding and heat transfer. The multi-assembly basket is a welded array of 24 carbon steel square storage sleeves to provide structural support to the SNF assemblies. The basket thickness is 25 mm and outside diameter is 1.59 m. The storage sleeves have side length 234 mm and thickness 5.1 mm. The annulus between the basket and the cavity is approximately 102 mm wide to allow adequate natural circulation. Maximum heat load, burn up and initial enrichment are 1 kW/assembly, 45 GWd/MTU and 4.2%  $^{235}\text{U}$ , respectively. The cask weight is approximately 144 tons when fully loaded. The fuel assemblies are stored in a fuel basket located inside the cask body which consists of welded borated stainless steel plates in an array of 24 square channels. An illustration of the VSC-24 is shown in Figure 2-5.

Table 2-1. Main characteristics of commercial dry casks [18].

Cask Model	Orientation	Fuel Support	Cask body
VSC-24	Vertical	Carbon Steel (Canister)	Reinforced concrete
CASTOR V/21	Vertical	Stainless Steel (Basket)	Cast Iron
NUHOMS	Horizontal	Stainless Steel (Canister)	Concrete
TN	Vertical	Stainless Steel (Basket)	Carbon Steel
HI-STORM	Vertical	Stainless Steel (Canister)	Concrete
HI-STAR	Vertical	Stainless Steel (Canister)	Carbon Steel

Table 2-2. Main dimensions of dry casks currently in use [18].

Description	VSC-24	CASTOR V/21	NUHOMS-32PT	NUHOMS-61BT
Fuel type	PWR	PWR	PWR	PWR
Assemblies	24	21	32	61
Maximum heat load (kW)	24	21	24	18.3
Minimum cooling time (years)	5	5	5	4
Maximum fuel burnup (GWd/MTU)	45	35	45	40
Weight (tons)				
Loaded	144	117	N/A	N/A
Empty	N/A	102	N/A	N/A
Orientation	Vertical	Vertical	Horizontal	Horizontal
Cask body				
Geometry	Cylindrical	Cylindrical	Rectangular	Rectangular
Material	Reinforced concrete	Cast Iron	Reinforced concrete	Reinforced concrete
Lid	Carbon steel, bolted	Stainless steel, bolted		
Outer diameter (m)	3.35	2.385	6.100 long	N/A
Inner diameter (m)	1.79	1.527	1.700 wide	N/A
Height (m)	5.0-5.72	4.886	4.600	N/A
Thickness (m)	0.74	0.380	0.910 top 0.610 side	N/A
Fuel Basket				
Geometry	Cylindrical	Cylindrical	Cylindrical	Cylindrical
Material	Carbon steel	Stainless steel	Stainless steel	Stainless steel
Outer diameter (m)	1.59	1.524	1.71	1.71
Inner diameter (m)	1.54	N/A	N/A	N/A
Height (m)	4.17-4.84	4.110	4.98	4.98
Thickness (m)	0.025	N/A	0.0127-0.0159	N/A
Gamma shielding	Concrete	Cask body	Concrete	Concrete
Neutron shielding	Concrete	Polyethylene rods	Concrete	Concrete

Table 2-2. Main dimensions of dry casks currently in use (cont'd).

Description	TN-32	TN-40	TN-68	HI-STORM	HI-STAR
Fuel type	PWR	PWR	BWR	PWR/BWR	PWR/BWR
Assemblies	32	40	68	24-32/68	24/68
Maximum heat load (kW)	32.7	27	30	27-36.9/36.9	19/18.5
Minimum cooling time (years)	7	10	7	3	5
Maximum fuel burnup (GWd/MTU)	45	45	60	68.2/65	42.1/37.6
Weight (tons)					
Loaded	105	103	104	163	77
Empty	N/A	N/A	N/A	N/A	N/A
Orientation	Vertical	Vertical	Vertical	Vertical	Vertical
Cask body					
Geometry	Cylindrical	Cylindrical	Cylindrical	Cylindrical	Cylindrical
Material	Carbon steel	Carbon steel	Carbon steel	Concrete	Carbon Steel
Lid	Bolted	Bolted	Bolted	Bolted	Bolted
Outer diameter (m)	2.48	N/A	N/A	3.37	2.44
Inner diameter (m)	1.75	N/A	N/A	1.77	1.75
Height (m)	5.13	N/A	N/A	6.08	5.159
Thickness (m)	0.317	N/A	N/A	0.800	0.345
Fuel Basket					
Geometry	Cylindrical	Cylindrical	Cylindrical	Cylindrical	Cylindrical
Material	Stainless steel	Stainless steel	Stainless steel	Stainless steel	Stainless steel
Outer diameter (m)	1.75	N/A	N/A	1.74	1.74
Inner diameter (m)	N/A	N/A	N/A	1.71	1.71
Height (m)	4.15	N/A	N/A	4.83	4.83
Thickness (m)	N/A	N/A	N/A	0.127	0.127
Gamma shielding	Carbon steel	Carbon steel	Carbon steel	Cask body	Cask body
Neutron shielding	Borated resin	Borated resin	Borated resin	Cask body	B <sub>4</sub> C



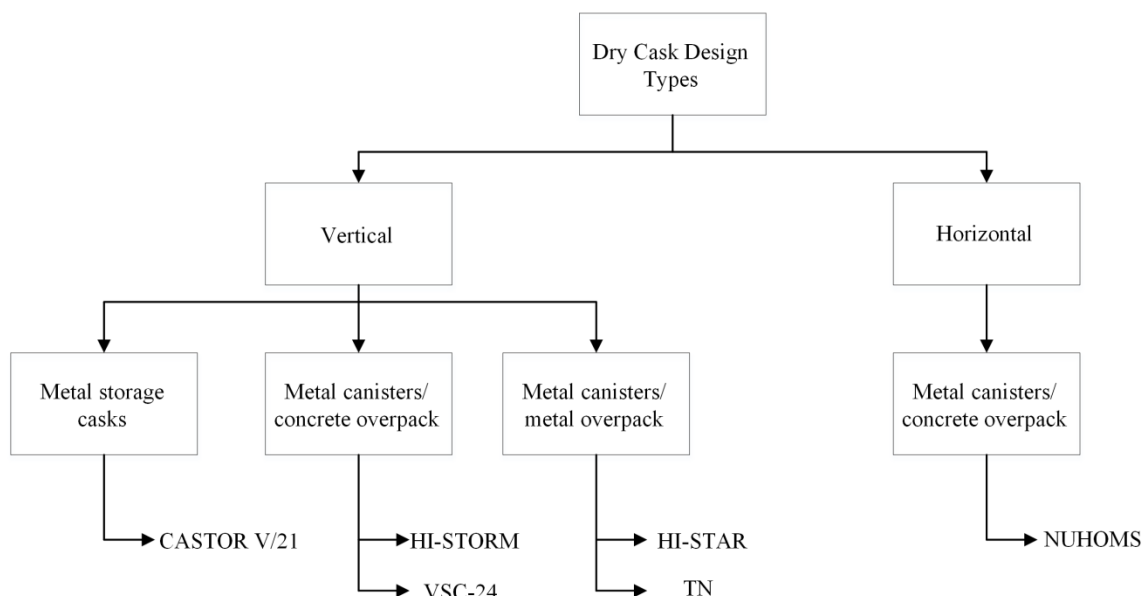


Figure 2-4. Classification of dry cask designs.

## ii. CASTOR-V/21

CASTOR V/21 is a storage only, vertically oriented metal cask with storage capacity of 21 PWR SNF assemblies. The cask body is a one piece cylindrical structure made of ductile cast iron. The overall external dimensions are 4.88 m height and 2.38 m diameter. Thickness and inner diameter are 0.379 and 1.527 meters, respectively. The cask body ensures the necessary functions of structural support, radiation shielding and heat transfer. Externally, it is covered circumferentially with heat transfer fins and it is coated with epoxy resin for corrosion protection. The cask is sealed with two stainless steel lids bolted to the cask. Elastomer seals are used to ensure leak tightness. Gamma shielding is provided by the cask body itself and neutron shielding is provided by polyethylene rods installed circumferentially inside the cask body. The fuel assemblies are stored in a fuel basket located inside the cask body. It consists of welded borated stainless steel plates in an array of 21 square channels. The basket diameter 1.524 m fits tightly in the cask

cavity. Maximum heat load, burn up and initial enrichment are 1 kW/assembly, 35 GWd/MTU and 4.2%  $^{235}\text{U}$ , respectively. The cask weight is approximately 117 tons when fully loaded. An illustration of the CASTOR V/21 is shown in Figure 2-5.

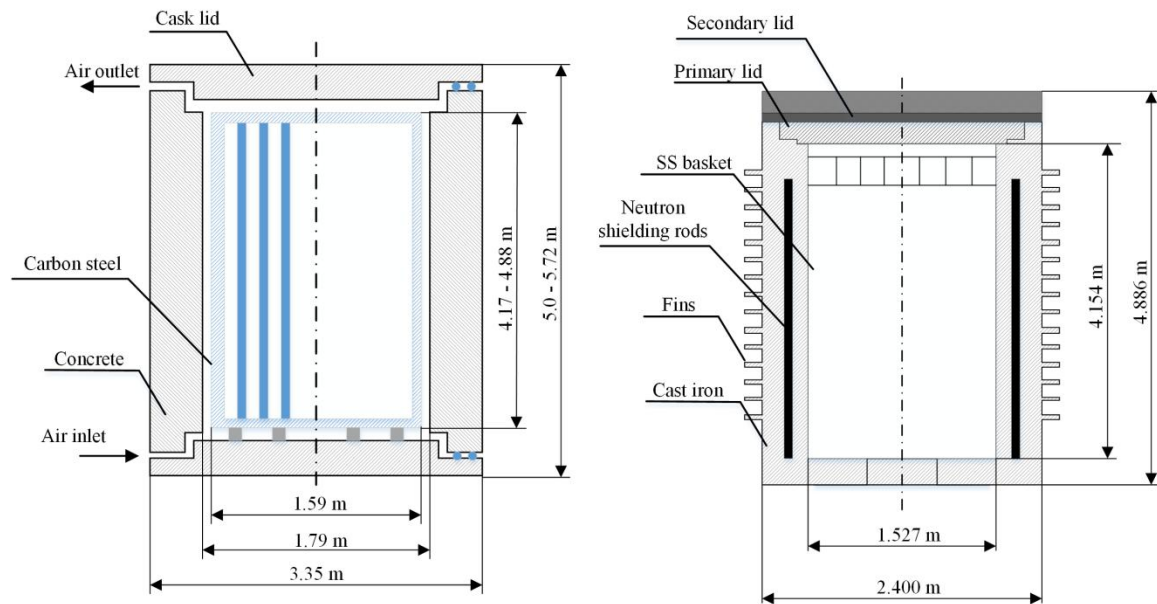


Figure 2-5. VSC-24 and CASTOR-V/21 main characteristics [18].

### iii. NUHOMS<sup>®</sup>

This cask system is used for horizontal dry storage of PWR/BWR fuel assemblies. A metal canister is placed in a concrete horizontal module. Each model is described by a designation following NUHOMS-XXY where XX refers to the number of fuel assemblies stored in the metal canister and Y refers to the type of fuel stored, either P for PWR or B for BWR. When the canister can be used for transportation the letter T is added at the end of the code designation and when the canister can accommodate high burn-up fuels the HB characters are added at the end of the code designation. For example NUHOMS-32P or NUHOMS-24PHB means that the canister can accommodate

32 PWR fuel assemblies or 24 high burn-up PWR assemblies, respectively. Current canisters are designed to accommodate 24 or 32 PWR and 52 or 61 BWR fuel assemblies. The canister provides support and criticality control for the fuel assemblies. It is made of stainless steel approximately 12.7 - 15.9 mm thick. The canister lid is welded and after draining and drying it is backfilled with helium to provide appropriate inert environment. The internal basket consists of borated sleeves to ensure subcriticality. The maximum heat load is in the range of 18-24 kW. The canister is housed in a prefabricated reinforced concrete structure. This structure provides canister support and environmental protection and also serves as gamma and neutron shielding. The structure is 0.91 m thick, 6.1 m long, 1.7 m wide and 4.6 m high. The structure is anchored to the concrete foundation to ensure stability under accident conditions.

#### iv. TN

The casks of the TN family (TN-24P, TN-40, TN-32, TN-68) are storage/transport metal casks that can store up to 40 PWR or 68 BWR SNF assemblies. The cask body is a cylindrical structure made of carbon steel. The overall external dimensions for the TN-32 cask are 5.13 m height and 2.48 m outer diameter. Thickness and inner diameter are 0.317 and 1.75 meters, respectively. The cask body ensures the necessary functions of structural support, radiation shielding and heat transfer. Externally, it is covered circumferentially with a neutron shield, consisting of borated polyester compound enclosed in aluminum boxes. The neutron shield is 0.114 meters thick. The cask is sealed with two carbon steel lids bolted to the cask. Gamma shielding is provided by the cask body itself (0.203 m thickness). The fuel assemblies are stored in a fuel basket located

inside the cask body. It consists of welded stainless steel and boral plates in an array of 32 square channels. The basket diameter 1.75 m fits tightly in the cask cavity. Maximum heat load, burn up and initial enrichment are 1 kW/assembly, 45 GWd/MTU and 4.0%  $^{235}\text{U}$ , respectively. The cask weight is approximately 105 tons when fully loaded.

#### v. HI-STORM 100/HI-STAR 100

HI-STAR is a vertical metal cask for both storage and transportation. The HI-STAR can store up to 24 PWR or 68 BWR assemblies. The cask consists of a steel cylindrical vessel with bolted closure plates. HI-STORM is a storage only vertical concrete overpack that houses the spent fuel assemblies in a stainless steel canister. THE HI-STORM can store up to 32 PWR or 68 BWR assemblies. The canister can be transferred to the HI-STAR cask for off-site transportation. The canister consists of a cylindrical stainless steel structure with a honeycomb fuel basket that is equipped with neutron absorbers. The canister is sealed with a stainless steel welded lid.

#### c. Cosmic ray muons

Cosmic ray muons are elementary particles of two charged types, positive and negative, having approximately 200 times the mass of electron. Muons are unstable particles, interact with matter through electromagnetic and weak interactions and have a lifetime of 2.2  $\mu\text{s}$ . Muons reach sea level from every direction at approximately one muon per minute per  $\text{cm}^2$  (10,000 per minute per  $\text{m}^2$ ) and their spectrum extends from sub-GeV to hundreds of GeVs with average energy in the order of 3 - 4 GeV [18-21]. A summary of muon characteristics and other related particles is shown in Table 2-3.

Table 2-3. Properties of subatomic particles [19].

	Particle	Symbol	Antiparticle	Rest Mass (MeV/c <sup>2</sup> )	Lifetime (s)
Baryons	Proton	p	-	938.3	Stable
	Neutron	n	-	939.6	920
	Charged pion	$\pi^-$	$\pi^+$	139.6	$2.60 \times 10^{-8}$
	Neutral pion	$\pi^0$	-	135.0	$0.83 \times 10^{-16}$
Leptons	Electron	$e^-$	$e^+$	0.511	Stable
	Neutrino (electron)	$\nu_e$	$\nu_e$	$\sim 0$	Stable
	Muon	$\mu^-$	$\mu^+$	105.7	$2.20 \times 10^{-6}$
	Neutrino (Muon)	$\nu_\mu$	$\nu_\mu$	$\sim 0$	Stable
	Tau	$\tau^-$	$\tau^+$	1777	$2.90 \times 10^{-13}$
	Neutrino (Tau)	$\nu_\tau$	$\nu_\tau$	$\sim 0$	Stable

#### i. Cosmic ray muon production

Cosmic ray muons are produced naturally in the atmosphere, approximately at 15 km above sea level, as a result of a steady flux of relativistic charged particles, known as primary cosmic rays, that fall constantly and from all directions upon the Earth. The very large individual energies of cosmic ray particles, millions of times greater than the energy of  $\gamma$ -rays emitted by radioactive materials, and their great penetrating power set the rays apart from all other kinds of radiation. Recent measurements show that primary cosmic radiation comprises of 98% protons and heavier nuclei and 2% of electrons [22]. Out of the 98% of protons and heavier nuclei, 87% are protons, 12% are helium nuclei and the rest are heavier nuclei. The magnetosphere and the ozone layer of the atmosphere create a protective layer that filters and shields from cosmic radiation. However, a small amount penetrates into the atmosphere where it collides with the molecules of the atmosphere creating extensive showers of secondary and tertiary particles that eventually reach sea-

level. The secondary particle shower includes among others protons, neutrons, pions, kaons, gammas, electrons and positrons.

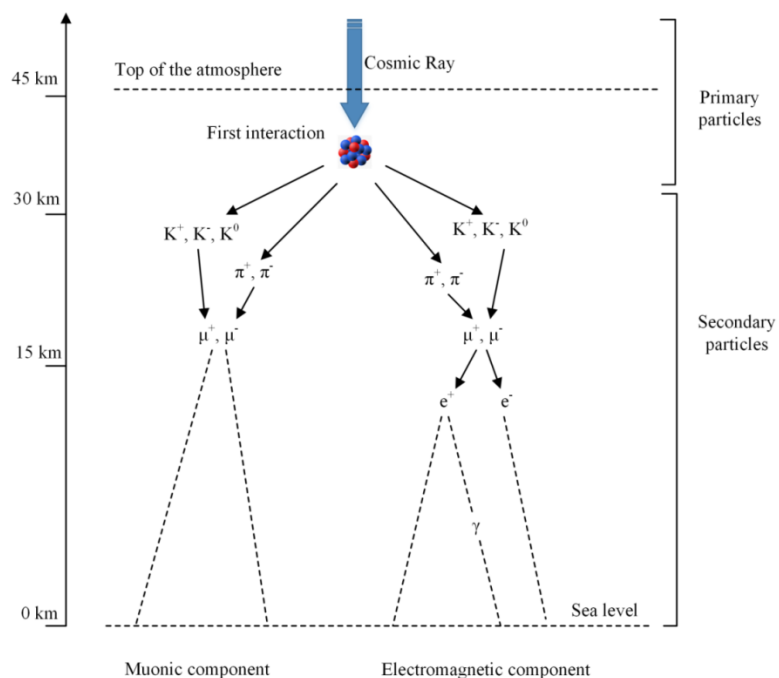
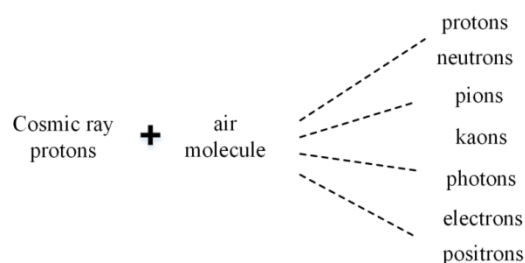


Figure 2-6. Secondary particle shower generation from primary cosmic rays.

Pions and kaons decay almost instantaneously to muons giving rise to a considerable muon flux that reaches sea level. Muons make up most of the cosmic radiation at sea level, the rest being electrons, positrons and photons from cascade events. A particle shower producing secondary particles is shown in Figure 2-6 and is represented schematically as follows:



Positive and negative pions are 264 times heavier than the electron and the neutral pion is 273 times heavier than the electron. Charged pions decay to muons and neutrinos:

$$\pi^+ \rightarrow \mu^+ + \nu_\mu \quad (2-1)$$

$$\pi^- \rightarrow \mu^- + \bar{\nu}_\mu \quad (2-2)$$

Neutral pions decay very rapidly producing two gamma rays:

$$\pi^0 \rightarrow \gamma + \gamma \quad (2-3)$$

The muon decay forms an electron or positron and corresponding neutrinos:

$$\mu^- \rightarrow e^- + \bar{\nu}_e + \nu_\mu \quad (2-4)$$

$$\mu^+ \rightarrow e^+ + \nu_e + \bar{\nu}_\mu \quad (2-5)$$

The negative muon can also be absorbed by a nucleus the same way electrons do. Bound negative muons can then interact with protons:

$$\mu^- + p \rightarrow n + \nu_\mu \quad (2-6)$$

Therefore, the negative muon has two ways of disappearing. Muons are also been generated in accelerators [21]. Proton accelerators irradiate nuclear targets producing pions which subsequently decay into muons. Accelerator generated muons are high intensity but low energy and short stopping range whereas cosmic ray muons are low intensity but high energy and long stopping range. A variety of applications have been initiated using these two types of muon sources. Accelerator produced muons have found applications to solid state physics and non-destructive elemental analysis. Cosmic ray muons have been used for obtain density profiles of large objects, e.g., volcanoes, or to identify the location of high-Z objects in a low-Z background. The first approach exploits

the stopping of muons in matter. The second approach takes advantage of the great penetrating abilities of muons to penetrate large dense objects [21].

## ii. Muon spectrum

Muons produced in the atmosphere arrive on ground level with a wide range of energies and zenith angles. The muon spectrum has been experimentally measured and shown to vary significantly with energy and zenith angle. The most representative experimental measurements are compiled in Table 2-4. The experiments cover a wide range of energies, from 0.2 to 20,000 GeV, zenith angles from  $0^\circ$  to  $89^\circ$  and 10 m to 1270 m altitude. It appears that the majority of the experiments were performed in low altitude and vertical or near vertical direction and only few experiments were realized in higher zenith angles. The experimental measurements of Nandi & Sinha [23], Tsuji et al. [24], Haino et al. [25] and Jokisch et al. [26] are shown in Figures 2-7 and 2-8. Above 10 GeV, the spectrum follows a power law profile which is practically independent of the zenith angle. For energies less than 10 GeV, the spectrum slope changes and zenith angle dependency increases. The influence of zenith angle is small up to  $30^\circ$  but becomes significant for larger angles. The muon spectrum is also influenced on geomagnetic effects which limit the primary proton flux and solar cycle which modulates the primary proton flux [19]. Geomagnetic effects filter the primary particles; this is equivalent to having a cut-off on the energy of the particles of  $\sim 15$  GeV near the equator reducing to 0 GeV on the poles. Solar activity follows sinusoidal profile with a period of 11 years and is inversely proportional to the primary flux, i.e., maximum solar activity minimizes the primary proton flux. Less important are atmospheric temperature/pressure variations. The



above dependencies become significant for muon energies less than 10 GeV. Less significant is the variation with respect to altitude [19].

Table 2-4. Compilation of muon spectrum experimental measurements.

No.	Authors	Year	Altitude (m)	Momentum range (GeV/c)	Zenith angle range (°)	Nominal zenith angle (°)
1	Baber et al. [27]	1968	52	3-1000	0	0
2	Allkofer et al. [28]	1971	10	0.2-1000	0	0
3	Allkofer and Dau [29]	1972	10	0.3-26	0	0
4	Nandi et al. [23]	1972	70	5-1200	0-0.3	0
5	Ayre et al. [30]	1975	70	20-500	0-0.08	0
6	Baxendale et al. [31]	1975	70	7-500	0	0
7	Kellogg et al. [32]	1978	10	50-1700	25.9-34.1	30
				50-1700	70.9-79.1	75
8	Jokisch et al. [26]	1979	10	1-1000	68-82	75
9	Rastin [33]	1984	52	4-3000	0	0
10	Matsuno et al. [34]	1984	10	100-20000	86-90	89
11	De Pascale et al. [35]	1993	600	0.2-100	0	0
12	Tsuji et al. [24]	1998	5	1.5-250	0-1	0
				2-250	26-34	30
				3-250	59-61	60
				3-250	69-81	75
				3-150	79-81	80
13	Kremer et al. [36]	1999	360	0.2-120	0	0
			1270	0.2-120	0	0
14	Haino et al. [25]	2004	30	0.6-400	0	0
15	L3 collaboration [37]	2005	450	20-3000	0-58	

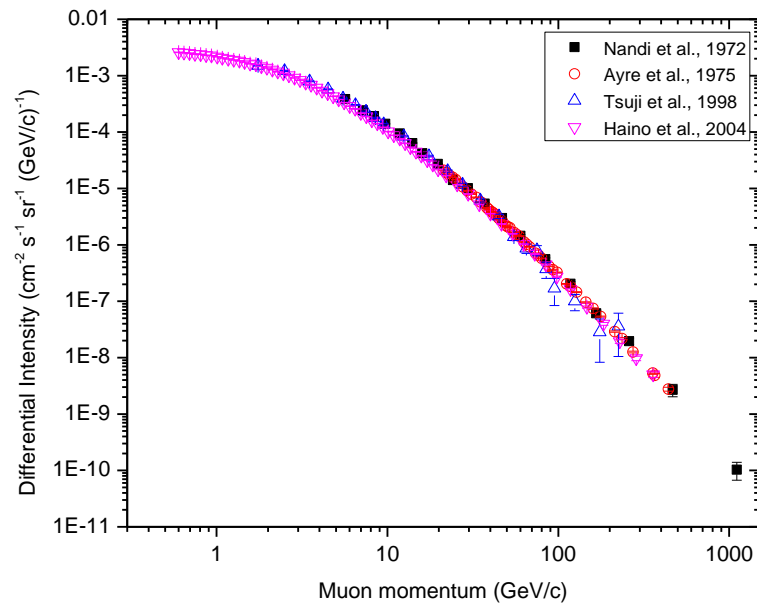


Figure 2-7. Experimentally measured muon differential intensity at  $0^\circ$  zenith angle.

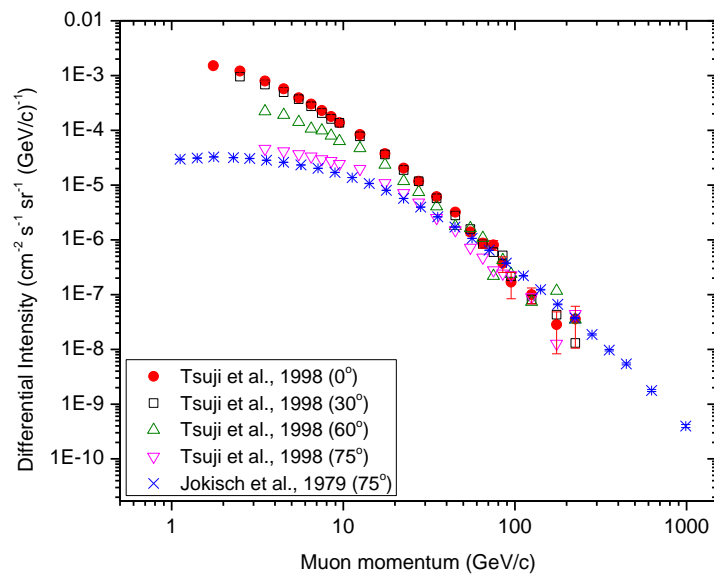


Figure 2-8. Experimentally measured muon differential intensity at different zenith angles.

### iii. Muon detectors

Several detector types have been proposed for muon detection. These include scintillators, drift tubes, resistive plate chambers and, solid state detectors. Existing muon detectors have used drift-wire chambers, e.g., the Large Muon Tracker developed at LANL [38]. Delay line chambers [8] have been used and small prototypes with gas electron multiplier detectors have been developed by the HEP lab at Florida Tech to determine muon positional information [39]. For spent nuclear fuel monitoring, muon detectors could be placed around a dry cask, as shown in Figure 2-9. The size, geometry and detector position affect resolution and measurement time.

Cox et al. [40] summarized the requirements for muon detector development concluding that coincidence timing in the order of nanoseconds, spatial resolution in the order of sub-mm and energy determination will be required for future applications. They noted that efficient detectors with large area and sensitive over hundreds of GeV would be needed to optimize statistics and reduce the time taken to collect adequate number of muons. Increasing detector separation distance decreases solid angle and increases detector volume. A time of flight technique was proposed for extracting energy information. It was concluded that picosecond timing resolution would be required to differentiate between GeV and several GeV muon energies.

### d. Previous work

Recently, cosmic ray muons are investigated for volcano imaging and cargo scanning applications. Their use is even extended to determination of molten nuclear fuel location in nuclear reactors having suffered from the effects of a severe accident similar to the one

happened in Fukushima [41-50]. Nagamine [45] used large horizontal muon detectors at on one side of the Mt. Tsukaba and based on muon attenuation principles reconstructed the internal structure of the volcano. Muons are also being investigated to image Mt. Vesuvius [46].

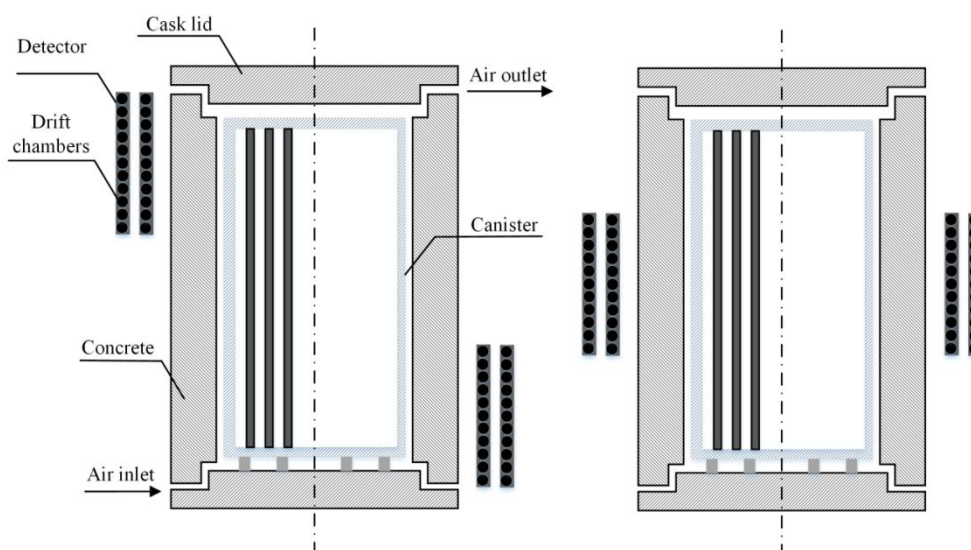


Figure 2-9. Placement of muon detectors around a dry cask. Left: detectors positioned at  $45^\circ$  zenith angle. Right: detectors positioned at  $89^\circ$  zenith angle.

Earlier muon radiographic techniques were based on attenuation principles. A new promising method based on multiple Coulomb scattering was pioneered, developed and demonstrated at LANL for detection of high-Z materials hidden in a large volume of low-Z materials, a situation representative of shielded material hidden in a cargo container [51, 52]. The muon scattering angles are sensitive to muon momentum, geometry and radiation length and by reconstructing the incoming and outgoing muon trajectories the scattering event can be estimated. The location can be assigned to a voxel leading to the development of imaging algorithms suitable for cargo scanning and molten fuel location [41-43]. Hogan et al. [51] demonstrated the detection of high Z targets against low Z

backgrounds using a large muon detector with resolution of 400  $\mu\text{m}$  (FWHM). It was pointed out that momentum measurement could improve image resolution and it could be achieved indirectly by measuring muon scattering in several layers of materials with known thickness. Shultz et al. developed a geometry based reconstruction algorithm, inspired by earlier work on nuclear scattering radiography, the Point-of-the-Closest-Approach (PoCA) [52]. A more detailed algorithm based on statistical reconstruction techniques that exploits measured muon scattering and displacement information was proposed and the results produced improved reconstruction images [42]. However, computation and memory usage issues limited its use [44]. Computational performance was improved by an updated version of the imaging algorithm based on expectation maximization [42]. Alternative techniques to imaging have been proposed and include the development of monitoring algorithms suitable to provide a fast yes/no decision [53-55]. Classifiers may allow high-Z material detection without tomographic reconstruction. Muon radiography efficiency can be increased using additional information sources such as momentum estimation, attenuation and detection of characteristic gamma rays emitted during the generation of a muonic atom. Morris et al. [49] combined muon stopping and muon scattering to determine areal density and material identification. Using the Mini Muon Tracker, muon transmission and muon scattering measurements were performed in lead, concrete and steel blocks having three thicknesses. The scattering distribution was approximated using a seven group momentum model. The parameters of the model were fitted to actual data. The negative of the natural logarithm of transmission was shown to be proportional to material thickness and combined with measurements of the thickness of the object in radiation lengths can provide the areal density and the material.

#### e. Summary

This chapter presented historical and background information on spent nuclear fuel and its storage at ISFSIs. The characteristics of spent nuclear fuel and dry casks were reviewed. A brief introduction to cosmic ray muons and their properties were discussed. Some details on muon spectrum and muon detectors were outlined. Previous work on muon monitoring and imaging applications that provided much of the inspiration for the present work was summarized.

## CHAPTER 3. PRELIMINARY CALCULATIONS

This chapter provides information pertinent to muon-matter interactions. A description of the muon energy loss and theory of multiple Coulomb scattering are presented and discussed in Section 3-1. Section 3.2 provides a description of GEANT4 dry cask simulations, validation results and estimation of the scattering variance. The derivation of the scattering variance distribution and the properties of the estimator are presented in Section 3.3. This chapter concludes with simulations of muon-dry cask interactions performed to investigate the asymptotic behavior of the scattering variance and determination of a decision boundary between a fully loaded dry cask and one with a fuel assembly missing.

### a. Muon interactions with matter

#### i. Ionization and energy loss

Muons are subject to electromagnetic interactions with matter. The energy loss rate is characterized by Coulomb interactions with the medium nuclei and electrons. Muons travelling through matter cause thousands of ionizations and excitations of the atoms. A muon undergoes a series of collisions with the nuclei and electrons of the medium, losing energy and changing its direction. The collisions are random processes and each muon

will not suffer the same energy loss (Figure 3-1). Three energy loss mechanisms are needed to describe the energy loss rate of a charged particle through matter: nuclear collisions, electronic collisions and radiative processes [56].

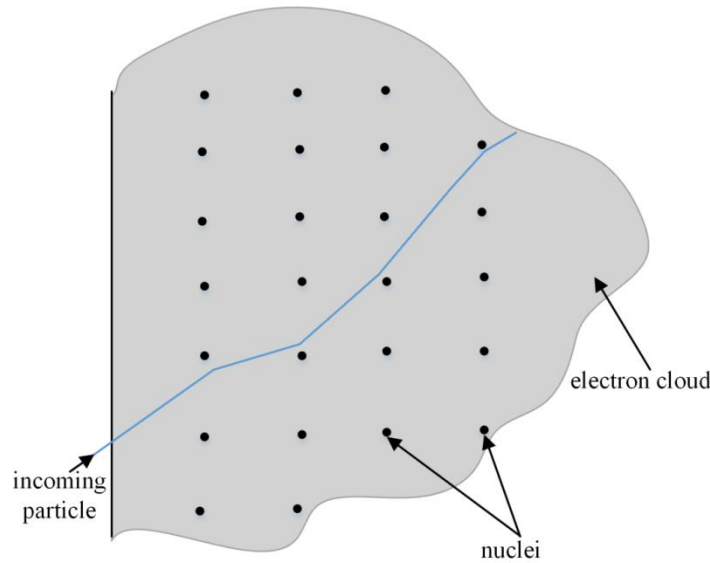


Figure 3-1. Passage of a charged particle through matter [56].

Nuclear collisions involve energy losses in discrete steps and significant change in direction. Electronic collisions involve continuous energy losses and small angular deflection of the trajectory of the particle. The relative importance of the above energy loss mechanisms varies rapidly with the energy and atomic number of the particle. As rule of thumb, nuclear collision energy loss dominates for low particle energies whereas electronic energy loss dominates for high particle energies. The total energy loss is the sum of all the interactions with matter, i.e., nuclear, electronic and radiative [54]:

$$\frac{dE}{dx} = \left. \frac{dE}{dx} \right|_n + \left. \frac{dE}{dx} \right|_e + \left. \frac{dE}{dx} \right|_r \quad (3-1)$$



The main parameters governing the amount of energy lost in each collision depend on the energy and mass of the particle as well as the characteristics of the material. Muons are high energy singly charged particles and slow down completely due to Coulombic interactions. A comparison of the nuclear and electronic energy loss mechanisms is shown in Figure 3-2. In region I, for small kinetic energies, nuclear energy loss dominates. For higher energies, electronic losses become important (regions II and III) and for even higher energies, radiation processes represent the main energy loss mechanism (region IV). For energies corresponding to particle velocities significantly lower than the Bohr velocity (region I) the elastic collisions with the matter nuclei dominate. As the particle energy increases, the nuclear energy loss is decreasing as  $1/E$ . Further increase in energy increases the contribution of the electronic energy loss which soon becomes the main loss mechanism. For energies significantly higher than the Bohr velocity where the electronic loss dominates (region III), the collisions produces a sudden transfer of energy to the electron which can be seen as a small external perturbation. The energy loss decreases with increasing particle energy because the particle spends less time in the vicinity of the electron.

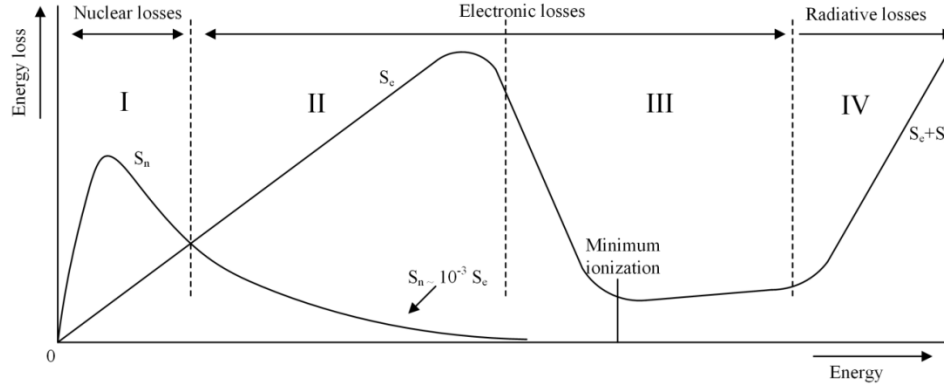


Figure 3-2. Relative importance of nuclear and electronic energy loss mechanisms [56].

The complete energy loss, known as Bethe-Bloch formula, includes corrections for relativistic and non-participation of the strongly bound inner shell electrons and provides a complete picture of the energy loss mechanisms. The Bethe formula applies to particle energies in the region III and is described by:

$$-\frac{dE}{dx} = 4\pi N_A r_e^2 m_e c^2 Z_1^2 \frac{Z_2}{A_2} \frac{1}{\beta^2} \left[ \frac{1}{2} \ln \frac{2m_e c^2 \beta^2 \gamma^2 T_{max}}{I^2} - \beta^2 - \frac{\delta}{2} \right] \quad (3-2)$$

where  $N_A$ ,  $r_e$ ,  $m_e$ ,  $Z_1$ ,  $Z_2$ ,  $A_2$  are Avogadro's number, Bohr radius, electron mass, incoming particle charge, medium atomic number and mass, respectively.  $T_{max}$  is the maximum energy loss in a single collision with an electron:

$$T_{max} = \frac{2m_e c^2 \beta^2 \gamma^2}{1 + 2\gamma m_e/M + (m_e/M)^2} \quad (3-3)$$

The Bethe-Bloch stopping power formula in a simplified form can be written as:

$$-\frac{dE}{dx} = Z_1^2 \frac{Z_2}{A_2} \frac{1}{\beta^2} f(I, \beta) \quad (3-4)$$

There is only a weak dependence of  $Z_2/A_2$  which for most materials is very close to 0.5 (Table 3-1) and therefore the stopping power, i.e., energy loss per unit mass, is

approximately constant. For singly charged particles the stopping power at its minimum is approximately 2 MeV/cm<sup>2</sup>/g. The energy loss per unit length slightly increases with increasing muon energy and for dense materials such as uranium is in the order of ~30 MeV/cm. The muon energy loss using the Bethe formula for a variety of materials and muon energies is shown in Table 3-1. For a commercial dry cask consisting mainly of concrete with total thickness  $L_{\text{concrete}}=140$  cm and  $\text{UO}_2$  with thickness  $L_{\text{UO}_2}=90$  cm, a 5 GeV muon will lose approximately:

$$dE_{\text{concrete}} * L_{\text{concrete}} + dE_{\text{UO}_2} * L_{\text{UO}_2} = 4.77 * 140 + 17.11 * 90 = 2207 \text{ MeV}$$

Table 3-1. Muon energy loss for different materials.

	Z/A	Energy loss (MeV/cm)		
	(-)	3 GeV/c	5 GeV/c	10 GeV/c
Air	0.499	0.0023	0.0025	0.0028
Water	0.555	2.13	2.28	2.5
Concrete	0.502	4.46	4.77	5.23
Iron	0.481	14.22	15.22	16.66
$\text{UO}_2$	0.465	15.99	17.11	18.73
Uranium	0.395	28.5	30.51	33.4

A total energy of ~2 GeV is lost every time a muon passes completely through a fully loaded dry cask. Muons with energies lower than 2 GeV will not be able to penetrate and these muons could be used to apply attenuation techniques for dry cask monitoring. Muons with energies higher than 2 GeV will be able to penetrate and multiple Coulomb scattering, described below, could be used to infer the stored contents. A muon passing through an object having sufficient thickness will eventually lose all of its energy and will stop within the medium. The mean range of a muon with initial kinetic energy E can be calculated:

$$R = \int_0^R dx = \int_0^E \frac{dE}{(-dE/dx)} \quad (3-5)$$

The range for 3 GeV muons in various materials is shown in Table 3-2. It is noted that muons will stop only after traversing large thicknesses of matter even in the case of dense materials such as uranium. For example, a 3 GeV muon will stop after penetrating 1 meter of uranium.

## ii. Multiple Coulomb scattering

Muons passing through matter, besides losing energy from inelastic collisions with the medium electrons, are deflected from nuclei due to Coulomb scattering. As muons move through a medium they travel in almost straight lines unless they are deflected by a nucleus. The frequency of nucleus-muon interactions increases with decreasing muon energy. Large angle deflections from nuclei can also occur if a muon impact parameter is similar to nuclei size. The overall deflection is the sum of all the small random contributions during a particle's path. The scattering and displacement distribution has been derived by the theory of Moliere [57] and can be approximated as Gaussian with zero mean. Moliere derived the scattering distribution starting from Rutherford's single scattering formula together with the small angle approximation. The Thomas-Fermi model of the atom was used to account for the screening of the Coulomb potential by the atomic electrons. The projected angles in x and y planes are independent and identically distributed and can be approximated with a zero mean Gaussian distribution:

$$P(\theta_x|0, \sigma_{\theta_x}^2) = \frac{1}{\sqrt{2\pi}\sigma_{\theta_x}} e^{\left(-\frac{\theta_x^2}{2\sigma_{\theta_x}^2}\right)} \quad (3-6)$$

The scattering displacement is also normally distributed. In this case, the standard deviation is given by:

$$\sigma_{\Delta x} = \frac{H}{\sqrt{3}} \sigma_{\theta_x} \quad (3-7)$$

The correlation coefficient is:

$$\rho = \frac{Cov(\Delta\theta, \Delta x)}{\sigma_{\Delta\theta} \sigma_{\Delta x}} = \frac{\sqrt{3}}{2} \quad (3-8)$$

The  $D = \begin{bmatrix} \Delta\theta \\ \Delta x \end{bmatrix}$  bivariate distribution is given by:

$$P(D|0, \Sigma) = \frac{1}{2\pi|\Sigma|^{1/2}} \exp\left(-\frac{1}{2} D^T \Sigma^{-1} D\right) \quad (3-9)$$

where  $\Sigma$  is the covariance matrix.

$$\Sigma = \begin{bmatrix} \sigma_{\Delta\theta}^2 & \rho\sigma_{\Delta\theta}\sigma_{\Delta x} \\ \rho\sigma_{\Delta\theta}\sigma_{\Delta x} & \sigma_{\Delta x}^2 \end{bmatrix} \quad (3-10)$$

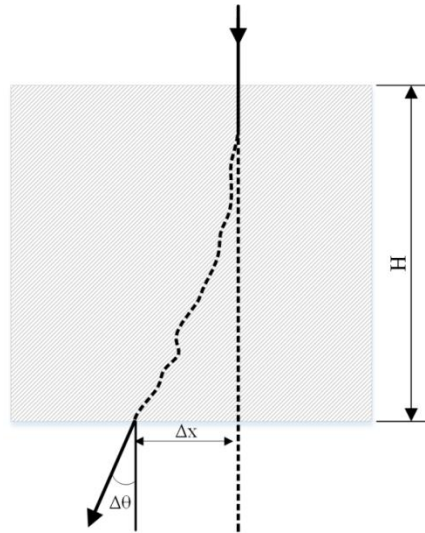


Figure 3-3. Muon trajectory as it passes through matter.

The root mean square (RMS) scattering angle of the Gaussian part in Moliere's scattering distribution is given by [57]:

$$\theta_{RMS}^M = \chi_c \sqrt{B} \quad (3-11)$$

where:

$$B = 1.153 + 2.583 \log(\chi_c/\chi_a)^2 \quad (3-12)$$

Moliere defined the characteristic angle which was corrected by Bethe to account for the inelastic scattering off atomic electrons and for homogeneous targets is:

$$\chi_c^2 = \frac{4\pi N_A \rho X z^2 Z(Z+1)e^4}{Ap^2\beta^2c} \quad (3-13)$$

where  $N_A$  is Avogadro's number,  $Z$  and  $A$  the atomic and mass number,  $\rho$  is the density of the materials,  $X$  material thickness. Moliere used the Thomas-Fermi model to account for the screening of the Coulomb potential by the atomic electrons and derived an expression for the screening angle:

$$\chi_a^2 = \chi_0^2(R + 3.76\eta^2) \quad (3-14)$$

where  $R=1.13$ .  $R$  is constant for all  $Z$  and:

$$\chi_0 = 1.13\alpha(m_e c/p)Z^{1/3} \quad (3-15)$$

$$\eta = \frac{zZe^2}{\hbar v} \quad (3-16)$$

A considerably simpler expression has been given by Rossi and Greisen that has been extensively used [58]:

$$\theta_{RMS}^{RG} = \frac{21.2 \text{ MeV}}{\beta c p} \sqrt{\frac{X}{X_0}} \quad (3-17)$$

In 1975, Highland [59] suggested that a correction term to the Rossi-Greisen formula which results to the following expression, currently adopted by Particle Data Group:

$$\theta_{RMS}^H = \frac{13.6\sqrt{2} \text{ MeV}}{\beta cp} \sqrt{\frac{X}{X_0}} \left[ 1 + 0.088 \ln \left( \frac{X}{X_0} \right) \right] \quad (3-18)$$

Finally, Lynch and Dahl [60] suggested that a form where the  $\ln(X/X_0)$  is replaced by  $\ln(ZX/X_0)$ :

$$\theta_{RMS}^L = \frac{13.6\sqrt{2} \text{ MeV}}{\beta cp} \sqrt{\frac{X}{X_0}} \left[ 1 + 0.038 \ln \left( \frac{ZX}{X_0} \right) \right] \quad (3-19)$$

In the above expressions,  $p$  is the particle's momentum in MeV/c,  $c$  is the speed of light,  $\beta$  is the ratio of particle's speed to the speed of light,  $X$  is the thickness of the traversed medium and,  $X_0$  is the radiation length.

### iii. Radiation length

Radiation length is a characteristic amount of matter, usually measured in  $\text{g/cm}^2$  or cm, and represents the average distance required for an electron to lose  $1/e$  of its energy. In the present work, radiation length was calculated using [61]:

$$\frac{1}{X_0} = 4\alpha r_e^2 \frac{N_A}{A} \{Z^2 [L_{rad} - f(Z)] + ZL'_{rad}\} \quad (3-20)$$

where  $Z$ ,  $A$ ,  $r_e$ ,  $N_A$  are the atomic number, atomic mass, Bohr radius and Avogadro number, respectively and:

$$L_{rad} = \ln(184.15Z^{-1/3}) \quad (3-21)$$

$$L'_{rad} = \ln(1194Z^{-2/3}) \quad (3-22)$$

for materials relevant to sealed containers. The function  $f(Z)$  is an infinite sum but for elements up to Uranium can be accurately represented by:

$$f(Z) = \alpha^2 [(1 + \alpha^2)^{-1} + 0.20206 - 0.0369\alpha^2 + 0.0083\alpha^4 - 0.002\alpha^6] \quad (3-23)$$

For compounds, i.e.,  $\text{UO}_2$ , the radiation length can be determined using:

$$\frac{1}{X_0} = \sum_i \frac{w_i}{X_i} \quad (3-24)$$

where  $w_i$  and  $X_i$  are the weight fraction and radiation length of the  $i$ -th element. For multiple layers of materials, as is the case of a spent nuclear fuel dry cask, the combined radiation length is calculated using:

$$\frac{d_0 \rho_0}{X_0} = \sum_j \frac{d_j \rho_j}{X_j} \quad (3-25)$$

where  $d_j$ ,  $\rho_j$  and  $X_j$  are the thickness, density, and radiation length of the  $j$ th layer. Radiation length follows a decreasing trend with increasing material density, and therefore it is expected that the more dense the material the larger the scattering angle. This indicates that a partially loaded container would result in a smaller than normal scattering angle than a fully loaded. The trend of the radiation length in cm and  $\text{g/cm}^2$  is presented in Figure 3-4.

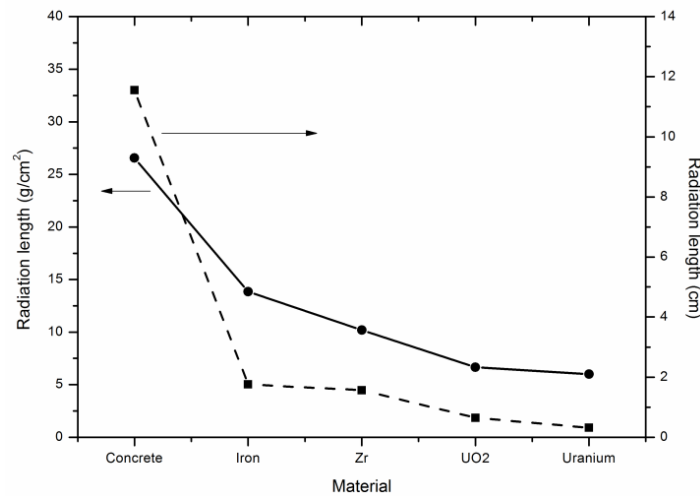


Figure 3-4. Radiation length for different materials.



Muon scattering per unit length increases with increasing material density. Muon scattering depends on the material and on the muon energy as shown in Table 3-3. Larger muon energy results in smaller scattering angles. This suggests that a muon with smaller muon energy passing through a dense material would give the same scattering angle with a muon having large energy passing through a less dense material. The dependency on muon energy could be used as a potential means to infer muon energy and techniques towards this goal have been recommended [52].

Dry casks loaded with spent nuclear fuel are comprised of multiple layers of inhomogeneous materials. To compare the effect of different dry casks on the muon scattering variance, the radiation length number is defined:

$$R = \frac{X}{X_0} \quad (3-26)$$

Table 3-2. Characteristics of 3 GeV muons in various materials.

Material	Volume density, g·cm <sup>-3</sup>	Radiation length, cm	Muon energy loss, MeV/cm	Muon range, m	Muon scattering, mrad
Air	0.0012	30516.67	0.0028	~10 <sup>5</sup>	0.64
Concrete	2.30	11.55	4.64	6.4	0.77
Iron	7.87	1.76	13.90	2.1	1.09
Lead	11.35	0.56	16.50	1.8	1.67
Uranium	18.95	0.32	28.51	1.1	1.72

Table 3-3. Scattering angle (mrad<sup>2</sup>) at different energies for materials relevant to dry casks.

	4 GeV	10 GeV	100 GeV
Air	0.1437·10 <sup>-3</sup>	0.2300·10 <sup>-6</sup>	0.2300·10 <sup>-8</sup>
Concrete	0.8232	0.1317	0.0013
Iron	6.2952	1.0072	0.0100
UO <sub>2</sub>	18.5052	2.9608	0.0296
Uranium	39.8837	6.3814	0.0638

The radiation length number is the ratio of the overall path traversed by a muon,  $X$ , divided by the overall radiation length,  $X_0$ , of the dry cask. This dimensionless number suggests that dry casks with the same radiation length number would result in the same scattering variance for muons passing through them and having identical energies. Radiation length numbers for six common dry cask designs have been calculated using equations (3-10) to (3-15). The first three belong to the class of casks having a concrete overpack, i.e., VSC-24, HI-STORM, NUHOMS, and the rest are casks with metallic body, i.e., CASTOR, TN, HI-STAR. The dry casks are considered to consist of the cask body and the spent nuclear fuel assemblies. Canister structure and inner basket have been neglected due to their small thickness. Figure 3-5 shows the simplified dry cask geometry. Two reference casks, one that corresponds to casks with concrete overpack and a second one corresponding to casks with metallic body, have been constructed in such a way that would provide similar radiation length number to the actual ones. The exact calculation results can be found in Appendix A. It appears that dry casks have an overall ratio  $X/X_0$  ranging from 10 when empty up to 180 when fully loaded (Figure 3-6).

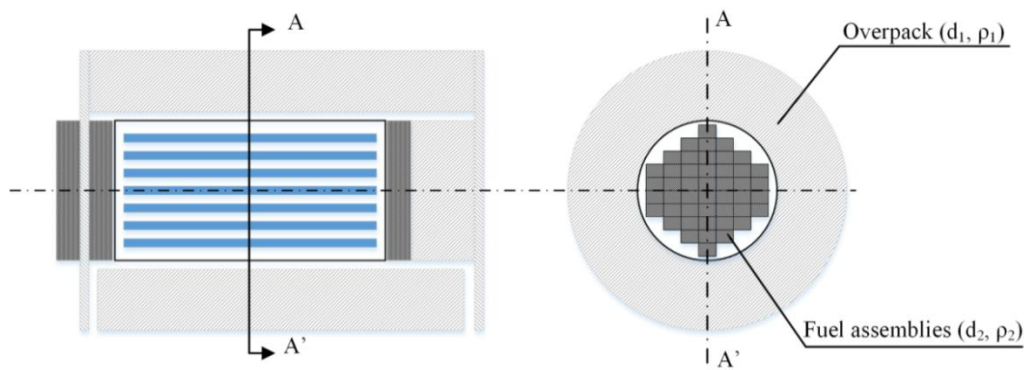


Figure 3-5. Simplified dry cask geometry for calculation of radiation length number  $R$ .

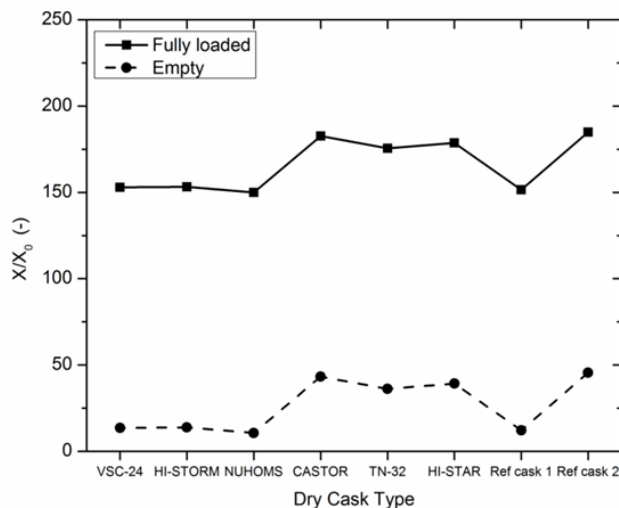


Figure 3-6. Ratio  $R=X/X_0$  for various commercial fully loaded and empty dry casks

#### b. GEANT4 simulations

##### i. GEANT4 Monte Carlo code

The GEANT4 Monte Carlo code [62-64] was used to perform muon simulations and estimate muon paths through spent nuclear fuel dry casks. GEANT4 is a Monte Carlo code developed for use by the High Energy Physics community. GEANT4 does not provide a built in library with muon energy and angular distributions. To generate muons from the actual measured muon spectrum a cosmic ray muon sampling capability, a “Muon Generator”, was developed [65]. The “Muon Generator” is based on a phenomenological model that captures the main characteristics of the experimentally measured spectrum coupled with a set of statistical algorithms. The muons generated can have zenith angles in the range  $0-90^\circ$  and energies in the range 1-100 GeV. The muon angular and energy distributions are reproduced using the “Muon Generator” and

integrated into GEANT4. The “Muon Generator” offers a way to allow easy coupling with GEANT4 interface. It generates the necessary user-defined histograms for use with the GEANT4 *G4GeneralParticleSource* macro file. The coupling is presented in Appendix B. Using the “Muon Generator”, simulations of muon-dry cask interactions can be performed.

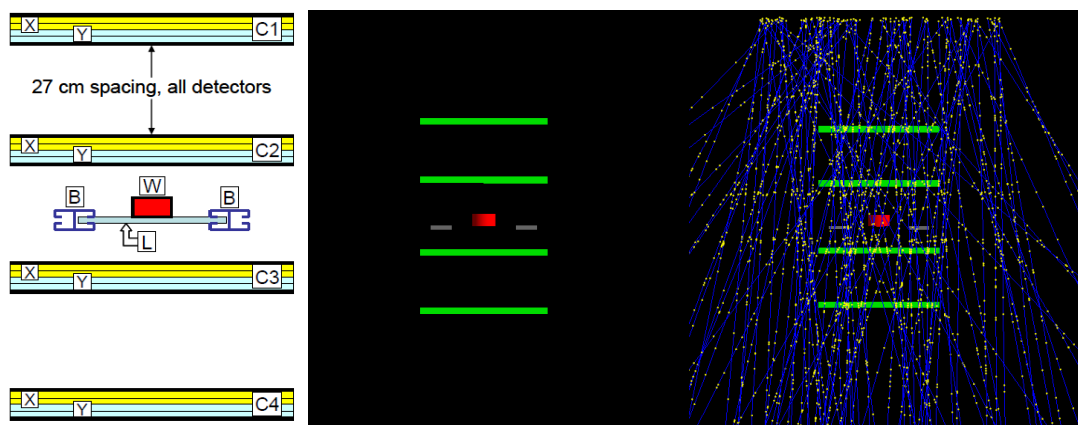
## ii. Experimental Validation

The use of GEANT4 to simulate the passage of muons through a test object was validated. As no experimental results of dry casks are currently available, a muon scattering demonstration by LANL was used as a benchmark. The test object was a tungsten cylinder, 11 cm in diameter and 5.7 cm in height, placed on a plastic platform. The platform was supported by two steel beams, 3 mm thickness each. The LANL muon prototype consisted of four wire chambers with active area  $60 \times 60 \text{ cm}^2$ , filled with a gas mixture 65% argon and 35% isobutene, assembled into a stack and separated vertically by 27 cm. The detectors were triggered by plastic scintillators and resolution of the apparatus was found to be  $400 \text{ }\mu\text{m}$  FWHM. Figure 3-8a shows the detector prototype, the tungsten object and the steel beams. More details on the experiment setup can be found in [7]. The detector geometry, the test object and the supporting beams were modelled in GEANT4. The muon spectrum and angular distribution were reproduced using the “Muon Generator”. The muon source was a plane located above the muon detectors with area twice that of the detectors. The GEANT4 model of the detectors and muon trajectories are shown in Figures 3-7b and 3-7c. 100,000 muons were recorded, same as the experiment, and the PoCA reconstruction method was used. A voxel size of  $1 \text{ cm}^3$  and an object volume of  $60 \times 60 \times 30 \text{ cm}^3$  were used. Experimental and simulated results

appear in Figure 3-8. The simulated reconstructed images agree with those obtained from the experiment. The shape of the tungsten cylinder is correctly reconstructed. The supported beams appear as well.

### iii. Dry cask modeling

Figure 3-9 depicts the GEANT4 model of a commercial fully loaded with spent nuclear fuel dry cask. Monoenergetic and polyenergetic simulated muons incident upon the dry cask are also shown. The muon-dry cask interactions are depicted in yellow color. The dry cask consists of a concrete overpack, shown in red color, and fuel assemblies made of  $\text{UO}_2$ , shown in white color. The dry cask has concrete (density  $2.3 \text{ g/cm}^3$ ) walls, 3.658 m high and with inner and outer radius of 0.8635 m and 1.685 m, respectively. The fuel assemblies are rectangular in shape, 214.5x214.5 mm, and comprise of 15x15  $\text{UO}_2$  fuel rods, 3.658 m high and 10.7 mm in diameter. Canister structure, inner basket and fuel cladding have been neglected as it is not expected to significantly interact with muons due to their very small thickness. Plutonium and fission products have not been taken into account as they represent a very small fraction ( $\sim 3\%$ ) compared to uranium in the fuel assemblies.



(a) (b) (c)  
 Figure 3-7. LANL experimental apparatus with tungsten object and steel beams [7] (left)  
 - GEANT4 model (center) - Muon source and muon trajectories (right).



Figure 3-8. Experiment [7] (left) - Simulation without noise (center) - Simulation with 400  $\mu\text{m}$  FWHM Gaussian noise (right).

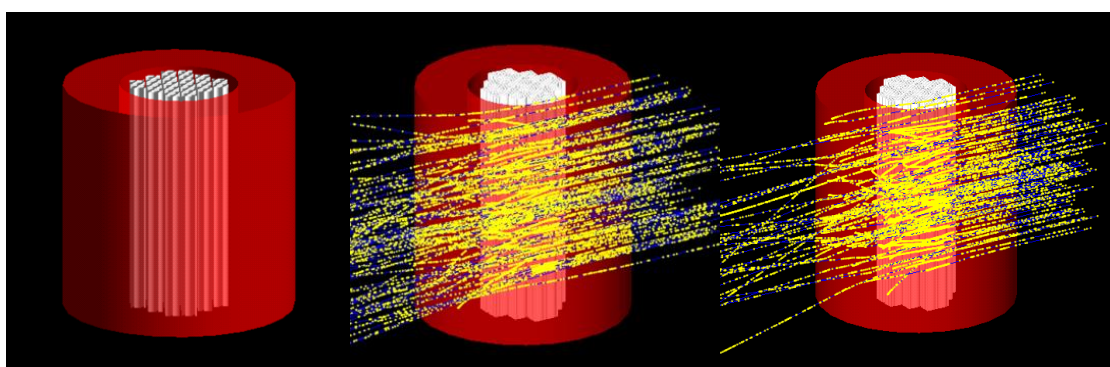
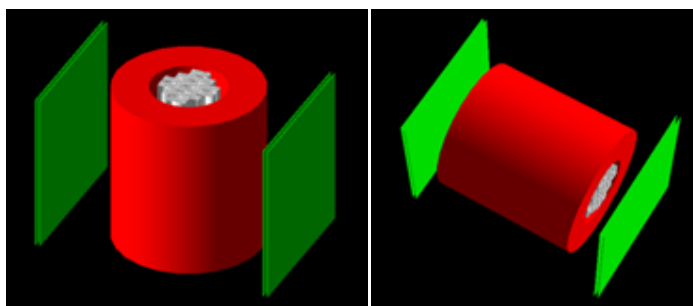


Figure 3-9. GEANT4 model of a fully loaded dry cask (left) - Visualization of muon paths through a dry cask (right).

Muon detection requires placement of detectors on two opposite sides of the object that is to be inspected. Cosmic ray muons pass through the first detector plane and their initial trajectories are recorded. The muons then pass through concrete and  $\text{UO}_2$ , exiting through another layer of concrete before hitting and interacting with the second plane of detectors where their final trajectories are also recorded. Using this information, calculations are performed to determine where the muon interactions occurred together with their displacement and scattering angles. The detectors (green color), illustrated in Figure 3-10,

are modeled as parallel planes of position sensitive chambers, e.g., drift-wire chambers or gas-electron multiplier detectors, that can record the position of each muon before and after interaction with the dry cask. Each muon will result in four recorded position measurements. The detectors used in the present work are idealized gas chambers, 1 cm thick, filled with argon gas at standard temperature and pressure and can record muon position, direction and momentum. Only the muon component of cosmic rays was simulated, other secondary particles were neglected. The muon source covers the detector active area and is initiated at a distance 20 cm from the first detector plane. The detector measurements are then processed to determine the scattering variance. Simulations were performed for three detector sizes having areas  $1.2 \times 1.2 \text{ m}^2$  (small)  $2.4 \times 2.4 \text{ m}^2$  (medium) and  $3.6 \times 3.6 \text{ m}^2$  (large). Only muons that pass through all detector planes were recorded. The detector position for vertical and horizontal dry casks is shown in Figure 3-10. The detectors cover different amount of area depending on their size, as shown in Figure 3-11. For example, in a horizontal dry cask, the small detector covers only part of the spent nuclear fuel whereas the large detector covers practically the whole dry cask.



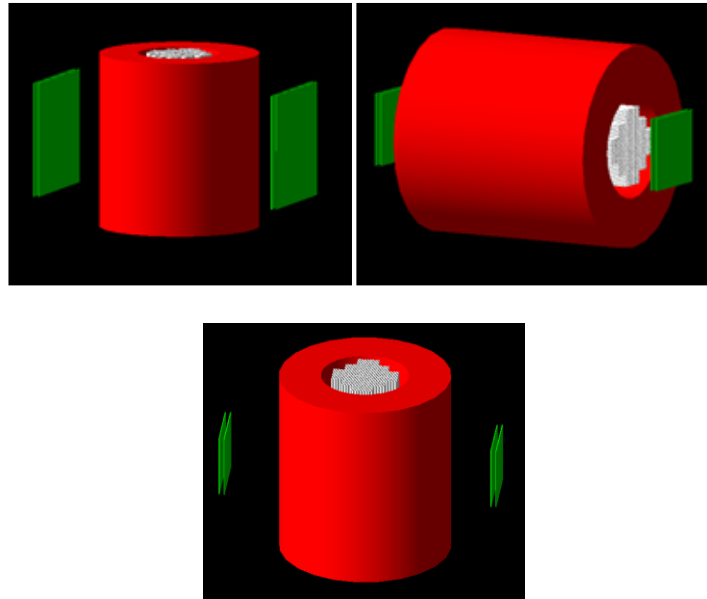


Figure 3-10. GEANT4 model of a vertical fully loaded dry cask and muon detectors (left)  
 - GEANT4 model of a horizontal fully loaded dry cask and muon detectors (right).

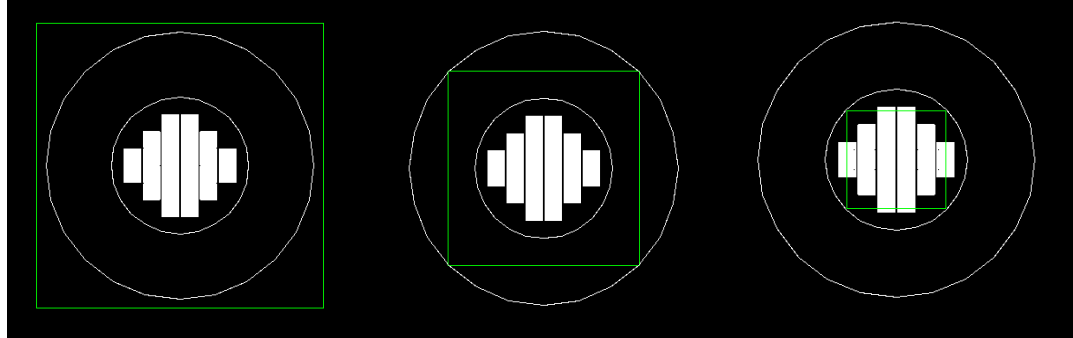


Figure 3-11. GEANT4 model of a vertical fully loaded dry cask and muon detectors (left)  
 - GEANT4 model of a horizontal fully loaded dry cask and muon detectors (right).

### c. Muon scattering variance

#### i. Scattering variance estimation and distribution

Figure 3-12 depicts dry cask simulations for 4 GeV muons incident upon a dry cask. One case considers a typical commercial dry cask fully loaded with 24 PWR fuel assemblies



while the other one is empty. A muon beam is initiated at  $45^\circ$  zenith angle and scattering patterns are visualized. The fully loaded cask has a wider distribution of deflection angles than its counterpart making it feasible to separate these two cases, albeit extreme for visualization purposes, with minimal processing. This simulation was based on monoenergetic - monodirectional muons initiated from a point source at  $45^\circ$  zenith angle. To take into account the energy spectrum and the angular distribution of actual muons,  $10^6$  muons having energies 1-60 GeV were simulated using the “Muon Generator” coupled with GEANT4. PWR fuel loadings, i.e., fully loaded, half loaded, one row of fuel assemblies missing, one fuel assembly missing and empty, were simulated to obtain accurate estimates of the scattering variance.

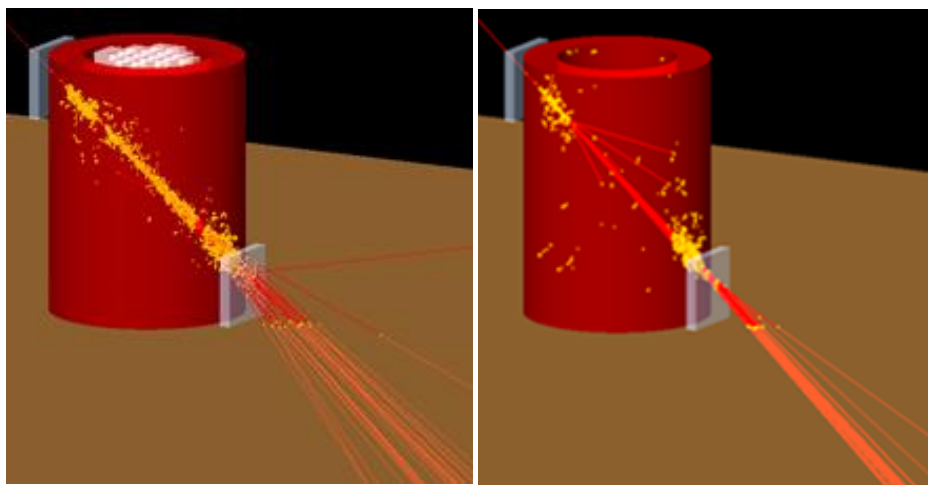


Figure 3-12. GEANT4 simulations. Fully loaded (left) and empty (right) dry cask. Detectors are located around the cask (light grey) and yellow points signify interactions with dry cask.

For each case, the scattering variance was estimated. This estimate is a function of random variables and therefore is a random variable itself. The random variable  $W$

represents the scattering variance and follows Gamma distribution with expected value and variance:

$$E[W] = \sigma^2 \quad (3-27)$$

$$Var[W] = \frac{2\sigma^4}{N} \quad (3-28)$$

The scattering variance estimator can be shown to be unbiased and to minimize the mean squared error, therefore it is a minimum variance unbiased estimator. Having knowledge of the scattering variance estimator, we can calculate how many muons need to be simulated to obtain a good estimate of the true value. This can be achieved using Chebyshev's inequality:

$$P(|W - E[W]| \geq \varepsilon) \leq \frac{Var(W)}{\varepsilon^2} \quad (3-29)$$

Using Chebyshev's inequality,  $10^6$  muons will provide scattering variance estimates that are within 1% of the true value at a 99% confidence level. The results of the scattering variance estimates for each case are shown in Table 3-4. Scattering variance decreases with decreasing amounts of fuel loading, in agreement with theory. The difference between a fully loaded dry cask and one with a fuel assembly missing is very small and high statistics will be required to differentiate between these two cases. In Table 3-5, the relative difference between a fully loaded dry cask and dry casks with smaller amounts of fuel is shown. The relative difference when one fuel assembly is missing is in the order of 1% to 5% depending on detector size and dry cask orientation. The results of the displacement variance are shown in Tables 3-6 and 3-7.

Table 3-4. GEANT4 estimated scattering variances for various fuel loadings and muon detector sizes ( $10^6$  muons).

	Vertical (mrad <sup>2</sup> )			Horizontal (mrad <sup>2</sup> )		
	Small	Medium	Large	Small	Medium	Large
Fully loaded	4373.164	5048.470	4119.453	2680.254	3853.753	3343.153
FA missing	4315.194	4981.015	4059.512	2545.822	3754.225	3292.644
Row missing	3438.542	4205.093	3475.069	1964.067	3401.041	3101.739
Half loaded	2652.753	3288.292	2792.103	1357.913	3003.923	2878.459
Empty	965.565	1542.145	1493.074	1.044	2101.649	2370.501

Table 3-5. Relative difference of scattering variance from fully loaded cask ( $10^6$  muons).

	Vertical			Horizontal		
	Small (%)	Medium (%)	Large (%)	Small (%)	Medium (%)	Large (%)
FA missing	1.32	1.33	1.45	5.01	2.58	1.51
Row missing	21.37	16.7	15.64	26.72	11.74	7.22
Half loaded	39.34	34.86	32.22	49.33	22.05	13.89
Empty	77.9	69.45	63.75	99.9	45.46	29.09

Table 3-6. GEANT4 estimated displacement variances for various fuel loadings and muon detector sizes ( $10^6$  muons).

	Vertical (mrad <sup>2</sup> )			Horizontal (mrad <sup>2</sup> )		
	Small	Medium	Large	Small	Medium	Large
Fully loaded	27848.12	32136.50	26345.69	12390.26	19245.07	16082.39
FA missing	27655.98	31854.38	26034.34	12559.77	19127.2	15993.11
Row missing	22319.62	26983.69	22328.85	11246.14	17916.14	15242.45
Half loaded	17264.84	20949.18	17828.14	7722.30	15498.58	13849.76
Empty	6597.98	9571.597	9340.414	8.875	9215.86	10263.38

Table 3-7. Relative difference of displacement variance from fully loaded cask ( $10^6$  muons).

	Vertical			Horizontal		
	Small (%)	Medium (%)	Large (%)	Small (%)	Medium (%)	Large (%)
FA missing	0.68	0.87	1.18	-1.36	0.61	0.55
Row missing	19.85	16.03	15.24	9.23	6.90	5.22
Half loaded	38.00	34.81	32.32	37.67	19.46	13.88
Empty	76.30	70.21	64.54	99.92	52.11	36.18

## ii. Differentiation between dry casks

Custom Monte Carlo simulations of muon-dry cask interactions were performed to investigate the asymptotic behavior of the scattering variance and whether the distributions between a fully loaded dry cask and one with a fuel assembly missing are adequately separated to allow for the determination of a decision boundary. The scattering variance estimates from GEANT4 calculated in the previous section were used as reference values for the calculation the scattering distributions resulting from muons having energies in the range of 1-60 GeV. Each simulation was repeated 5,000 times and the obtained scattering variance distributions are shown in Figure 3-15 for  $10^5$ ,  $2 \times 10^5$  and  $3 \times 10^5$  muons. The distributions initially overlap significantly for  $10^5$  muons and it is not possible to discriminate between the two cases. Significant overlap will lead to misclassifications, i.e., a fully loaded cask may be classified as having fuel assemblies missing (false alarm) or inversely a cask with missing fuel assemblies may be classified as fully loaded (miss). The distance increases with increasing number of muons. One missing fuel assembly can however be distinguished from a fully loaded cask with a small overlapping between the distributions when more than  $3 \times 10^5$  muons are measured. This indicates that the removal of a standard fuel assembly could be identified using muons providing that enough muons are collected. The increasing separation of the distributions reveals that the scattering variance can be used as a feature for discrimination between casks and the development of a classifier for that purpose is possible.

#### d. Summary

The major interactions between muons and matter were presented. Electromagnetic interactions can result in energy loss and multiple Coulomb scattering, processes which can be used to obtain information about the stored contents of a container. The scattering variance distribution was derived and the properties of the scattering variance estimator were evaluated. The scattering variance follows Gamma distribution and the maximum likelihood estimator was shown to be minimum variance unbiased estimator. Monte Carlo simulations were performed to obtain estimates of the scattering variance for various dry casks scenarios. The scattering variance estimates were used as reference values for the calculation of the scattering distributions. It was shown that the increasing separation of the distributions reveals that the scattering variance can be used as a feature for discrimination between casks and the development of a classifier for that purpose is possible. It is shown that the scattering distributions between a fully loaded dry cask and one with a fuel assembly missing initially overlap significantly but their distance eventually increases with increasing number of muons. One missing fuel assembly can be distinguished from a fully loaded cask with a small overlapping between the distributions which is the case of 300,000 muons. This indicates that the removal of a standard fuel assembly can be identified using muons providing that enough muons are collected. The separation of the distributions reveals that the scattering variance can be used as a feature for discrimination between casks and the development of a classifier for that purpose is possible.

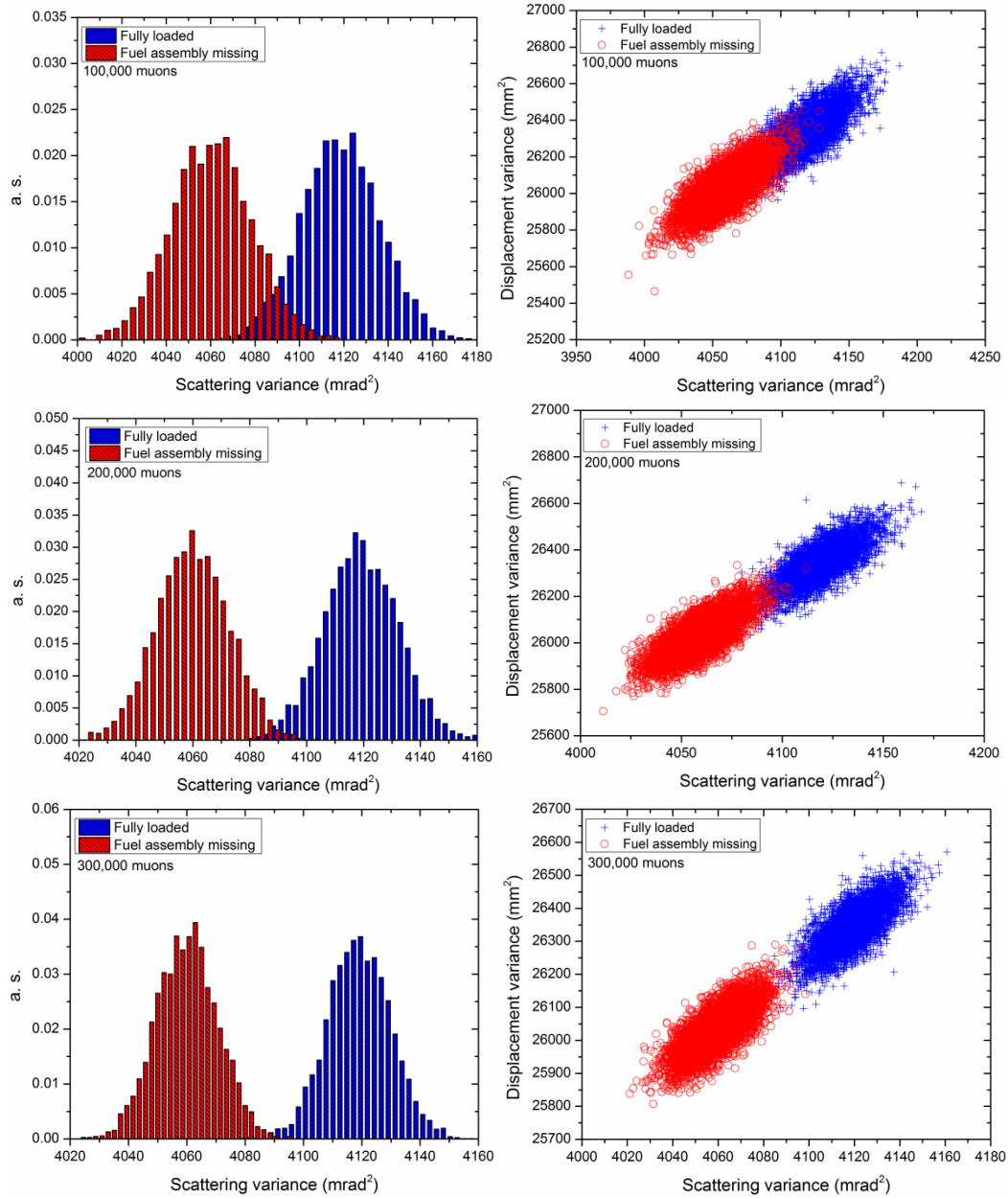


Figure 3-13. Scattering and displacement variance distributions as a function of the number of muons measured (top:  $10^5$  muons, middle:  $2 \times 10^5$  muons, bottom:  $3 \times 10^5$  muons).

## CHAPTER 4. SPENT NUCLEAR FUEL MONITORING

In the previous chapter it was shown that muon scattering distributions are adequately separated and a decision boundary can be drawn rendering the classification of different spent nuclear fuel dry casks feasible. In this chapter, a monitoring algorithm for binary classification of spent nuclear fuel dry casks is derived from Bayesian principles. The mathematical framework is outlined in Section 4.1 and the monitoring algorithm derivation is presented in Section 4.2. The objective is to design an algorithm that is optimal in the sense it minimizes the overall risk associated with a classification decision. The algorithm performance is evaluated in Section 4.3. Finally, the Minimax and ROC curves are presented and discussed in Sections 4.4 and 4.5, respectively.

### a. Bayesian monitoring framework

Bayesian decision theory assumes the existence and knowledge of the a-priori (prior) distributions of the tested hypotheses, classes or categories. The prior distributions represent the prior knowledge we may have before additional information is obtained for the measurement dataset. The monitoring algorithm is formulated as a binary hypothesis testing where a spent nuclear fuel dry cask belongs to one of two classes with the objective to determine a decision rule to classify the dry casks depending on their spent nuclear fuel content. The goal is to decide between the two hypotheses  $H_0$  and  $H_1$  based on the observation of a measurement vector  $\mathbf{Y}$ . In the Bayesian framework, the

observations, i.e., measurements, are modelled as random samples drawn from probability distributions. The Bayesian classification model is a mapping from the measurement vector to the predicted classes [68]. Given a binary classifier, there are four possible outcomes. If the true class is  $H_0$  and classified as  $H_0$ , then it is counted as true positive; if it is classified as  $H_1$ , then it is counted as a false alarm (false negative). If the true class is  $H_1$  and classified as  $H_0$ , then it is counted as a miss (false positive); if it is classified as  $H_1$ , then it is counted as detection (true negative). This can be represented using a two-by-two confusion matrix [69]:

True class \ Predicted class	$H_0$	$H_1$
	$H_0$	$H_1$
$H_0$	True positive (TP)	Miss (False positive, FP)
$H_1$	False alarm (False negative)	Detection (True negative)
Column total:	P	N

From the confusion matrix several quantities can be calculated. The true positive rate is estimated as the number of positives correctly classified over the total positives:

$$\text{true positive rate} = \frac{TP}{P} \quad (4-1)$$

The false positive rate is the ratio of negatives incorrectly classified over the total negatives:

$$\text{false positive rate} = \frac{FP}{N} \quad (4-2)$$

The overall error rate:



$$\text{Error rate} = 1 - \frac{TP + TN}{P + N} \quad (4-3)$$

The classification process involves extracting features from observations, and then the design of a decision rule that satisfies certain optimality criterion. Each decision presents a certain cost and a decision rule that minimizes the overall cost is sought. When the distributions of the random samples are not known, they can be deduced using an estimation method, e.g., maximum likelihood, which estimates the major parameters of the distributions, e.g., mean and standard deviation. In the present work, the probability distributions are known from the theory of multiple Coulomb scattering and the scattering mean and variance have been derived in the previous chapter. To verify the efficiency and the performance of the classifier, testing data drawn from the scattering variance distributions are used to calculate a number of performance metrics, including error rate and false alarm rate.

#### b. Monitoring algorithm

Bayes' theorem allows the calculation of the posterior distribution using the class conditional distributions and the prior distributions. Bayes' theorem is the starting point to form a Bayesian monitoring algorithm to classify dry casks into different classes based on the content of spent nuclear fuel assemblies. Bayes' inference utilizes the connection between the prior knowledge and the observation. For discrete random variables, Bayes' theorem takes the form [68]:

$$p_{\Theta|Y}(\theta|y) = \frac{p_{Y|\Theta}(y|\theta)p_{\Theta}(\theta)}{p_Y(y)} \quad (4-4)$$

where  $p$  represents the probability mass function. For continuous random variables [68]:

$$f_{\Theta|Y}(\theta|y) = \frac{f_{Y|\Theta}(y|\theta)f_{\Theta}(\theta)}{f_Y(y)} \quad (4-5)$$

where  $f$  is the probability density function. To facilitate the subsequent discussion, the following notation is used:

1. Parameter  $\theta$  where  $\theta \in \Lambda = \{0, 1, \dots, M-1\}$ .

2. Prior distributions  $\pi_0, \pi_1, \dots, \pi_{M-1}$  with:

$$\sum_{j=1}^{M-1} \pi_j = 1$$

3. Conditional distributions:

$$f_j(y) = p(Y = y|H_j)$$

4. Posterior distributions:

$$\pi_j(y) = p(H_j|Y = y)$$

By Bayes' theorem we can show that:

$$p(H_j|Y = y) = \frac{p(Y = y|H_j)p(H_j)}{p(Y = y)}$$

and

$$\pi_j(y) = \frac{f_j(y)\pi_j}{\sum_j f_j(y)\pi_j}$$

5. Decision rule  $\delta: \Gamma \rightarrow \Lambda$ . The decision rule is a function that takes an input  $y \in \Gamma$  and sends  $y$  to a value  $\delta(y) \in \Lambda$ .

6. Cost function  $C(i,j)$  or  $C_{i,j}$ . The cost function  $C_{i,j}$  represents the cost of choosing  $H_i$  when  $H_j$  holds. For a binary hypothesis, the cost function can be represented by the following table:

True class \ Predicted class	$H_0$	$H_1$
$H_0$	$C_{00}$	$C_{01}$
$H_1$	$C_{10}$	$C_{11}$

For example,  $C_{01}$  is the cost associated with selecting class  $H_0$  when  $H_1$  is the true class.

This case can be thought as a miss in the detection framework since we decide that nothing is there when something is. The cost of a false alarm would be  $C_{10}$ . The cost of a correct decision is  $C_{00}$  and  $C_{11}$ , in most cases zero. A uniform cost function will take the following form:

True class \ Predicted class	$H_0$	$H_1$
$H_0$	0	1
$H_1$	1	0

Typically, in object detection or classification, every decision is accompanied by a cost. If, for example, there is a dry cask with missing fuel assemblies that we are not able to detect, then there is cost associated with this decision. This situation we call it a miss. In the case were there is a fully loaded dry cask but we decide that there are missing fuel assemblies, then we have a false alarm. The cost associated with each decision is described by the cost function and the form of the cost function depends on the situation. For example, it is preferable to have false alarm than a miss in the case of spent nuclear fuel dry cask monitoring. It is reasonable to seek to minimize the cost associated with

each decision. Let, the measurement vector  $\mathbf{Y}$  admit the following probability functions depending whether  $H_0$  or  $H_1$  hypothesis holds:

$$H_0: \mathbf{Y} \sim f_0(\mathbf{y}) \quad (4-6)$$

$$H_1: \mathbf{Y} \sim f_1(\mathbf{y}) \quad (4-7)$$

Given  $\mathbf{Y}$  we must decide whether  $H_0$  or  $H_1$  holds. This is accomplished through the determination of a decision rule which partitions the measurement space in two disjoint sets  $R_0$  and  $R_1$ . Figure 4-1a shows two distributions and a hypothetical decision boundary that separates the 1-D space in two sets  $R_0$  and  $R_1$ . For a decision rule taking two values, e.g., 0 and 1, when  $\delta(\mathbf{y})=0$  we decide that  $H_0$  holds and when  $\delta(\mathbf{y})=1$  we decide that  $H_1$  holds. There can be infinitely many decision boundaries that partition the measurement space in two sets. Among all decision boundaries we search for the one that minimizes some optimality criterion.

Given the cost function, the overall Bayesian risk is defined as the expectation of the cost of selecting  $\delta$ :

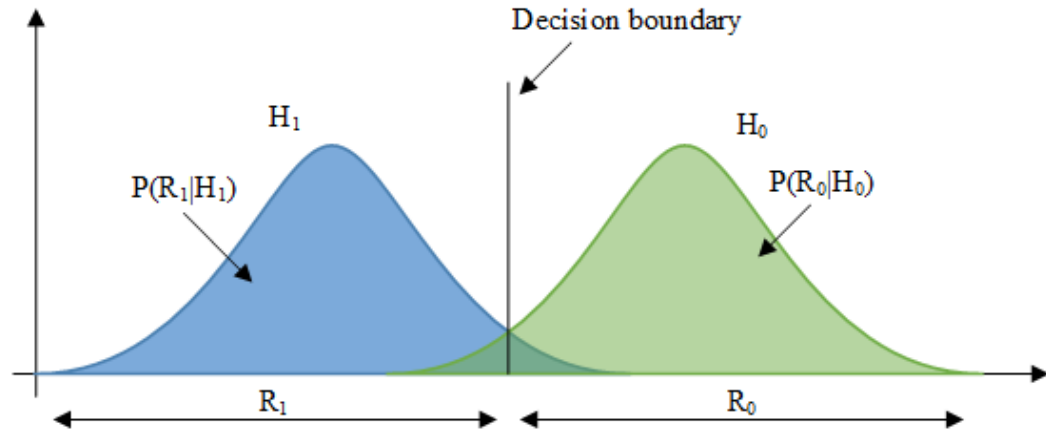
$$R(\delta) = \mathbb{E}_{\mathbf{Y}|\Theta} [C(\delta(\mathbf{Y}), \Theta)] \quad (4-8)$$

The Bayesian risk under hypothesis  $H_j$  is:

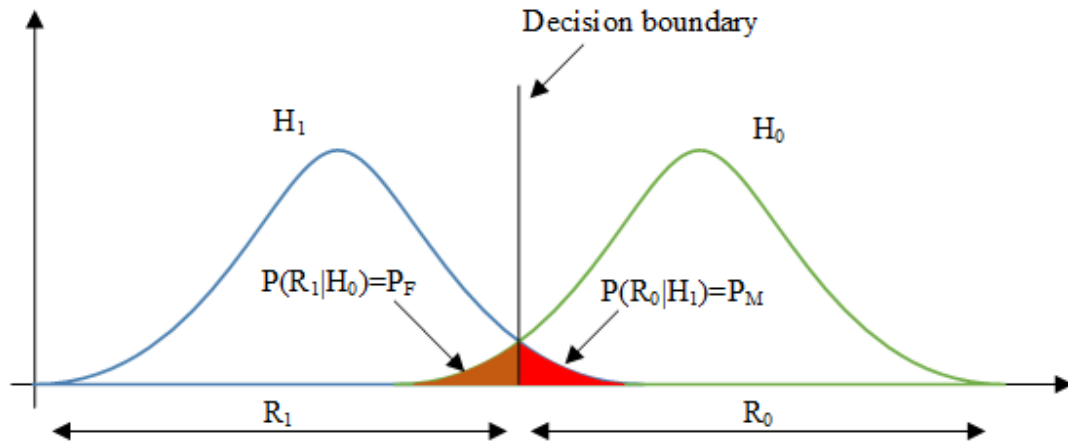
$$R(\delta|H_j) = \sum_{i=0}^1 c_{ij} \mathbb{P}(\mathcal{R}_i|H_j) \quad (4-9)$$

where

$$\mathbb{P}(\mathcal{R}_i|H_j) = \int_{\mathcal{R}_i} f_j(\mathbf{y}) d\mathbf{y} \quad (4-10)$$



(a)



(b)

Figure 4-1. Probability distributions of two classes  $H_0$  and  $H_1$  and decision boundary that separates the 1-D space in two sets  $R_0$  and  $R_1$  (a). Corresponding miss (red color) and false alarm (orange color) probabilities are shown in (b).

For example, the risk under hypothesis  $H_0$  is:

$$R(\delta|H_0) = \sum_{i=0}^1 C_{i0} \mathbb{P}(\mathcal{R}_i|H_0) = C_{00} \mathbb{P}(\mathcal{R}_1|H_0) + C_{10} \mathbb{P}(\mathcal{R}_1|H_0) \quad (4-11)$$

and under hypothesis  $H_1$ :

$$R(\delta|H_1) = \sum_{i=0}^1 C_{i1} \mathbb{P}(\mathcal{R}_i|H_1) = C_{01} \mathbb{P}(\mathcal{R}_0|H_1) + C_{11} \mathbb{P}(\mathcal{R}_1|H_1) \quad (4-12)$$

The average cost of selecting  $\delta$  is:

$$R(\delta) = \sum_{j=0}^1 R(\delta|H_j) \pi_j = \sum_{i=0}^1 \sum_{j=0}^1 C_{ij} \mathbb{P}(\mathcal{R}_i|H_j) \pi_j \quad (4-13)$$

The probabilities that define the Bayesian risk represent frequently used quantities in statistical signal detection and classification. These are the probability of detection, probability of false alarm and probability of miss. The probability of detection is:

$$\mathbb{P}_D = \mathbb{P}(\mathcal{R}_1|H_1) = \int_{\mathcal{R}_1} f_1(y) dy \quad (4-14)$$

The probability of a miss:

$$\mathbb{P}_M = 1 - \mathbb{P}_D = \mathbb{P}(\mathcal{R}_0|H_1) = \int_{\mathcal{R}_0} f_1(y) dy \quad (4-15)$$

The probability of false alarm:

$$\mathbb{P}_F = \mathbb{P}(\mathcal{R}_1|H_0) = \int_{\mathcal{R}_1} f_0(y) dy \quad (4-16)$$

The miss and false alarm probabilities are shown schematically in Figure 4-1b. The overall risk can be expressed in terms of the above probabilities:

$$R(\delta) = C_{00} \pi_0 + C_{01} \pi_1 + (C_{10} - C_{00}) \mathbb{P}_F \pi_0 + (C_{11} - C_{01}) \mathbb{P}_D \pi_1 \quad (4-17)$$

This shows that the overall risk can be written as a function of the pair  $(\mathbb{P}_F, \mathbb{P}_D)$ . For uniform cost the risk is simplified to the probability of error:

$$R(\delta) = \pi_0 \mathbb{P}(\mathcal{R}_1|H_0) + \pi_1 \mathbb{P}(\mathcal{R}_0|H_1) = \pi_0 \mathbb{P}_F + \pi_1 \mathbb{P}_M = \mathbb{P}_{error} \quad (4-18)$$

We seek to find a decision rule that will minimize the risk. In other words:

$$\delta(y) = \underset{\delta}{\operatorname{argmin}} R(\delta) \quad (4-9)$$

Minimizing the risk defined as the expectation of the cost function is analytically very difficult as it involves the minimization of the double integrals. To solve this problem we use the following proposition:

$$\delta(y) = \underset{\delta}{\operatorname{argmin}} \mathbb{E}_{Y\Theta}[C(\delta(Y), \Theta)] = \underset{i}{\operatorname{argmin}} \sum_{j=0}^{M-1} C(i, j) \pi_j(y) \quad (4-20)$$

c. Bayesian monitoring algorithm

A Bayesian monitoring system was developed to classify dry casks based on their content using a decision rule that minimizes the Bayesian risk of making an incorrect decision. The monitoring system takes an input measurement vector, performs feature extraction, and a binary Bayesian classifier that outputs a decision. The classifier block diagram is shown in Figure 4-2. The input measurement vector  $\mathbf{Y}$  contains the muon scattering angles. Processing of scattering angles would result in the extraction of an appropriate feature that captures the behavior of the system, in the present case, the scattering variance. Training data, either simulated or experimental, are needed to train the classifier and determine the decision boundary. Parameter estimation of the underlying distributions can be achieved using any density estimation statistical method, e.g., maximum likelihood estimation. Testing data are used to complete the design, analyze the performance of the classifier and evaluate false alarm rate, detection rate, effect of prior knowledge and cost function. The final outcome of the classifier would be a decision that will allow classification of a dry cask.

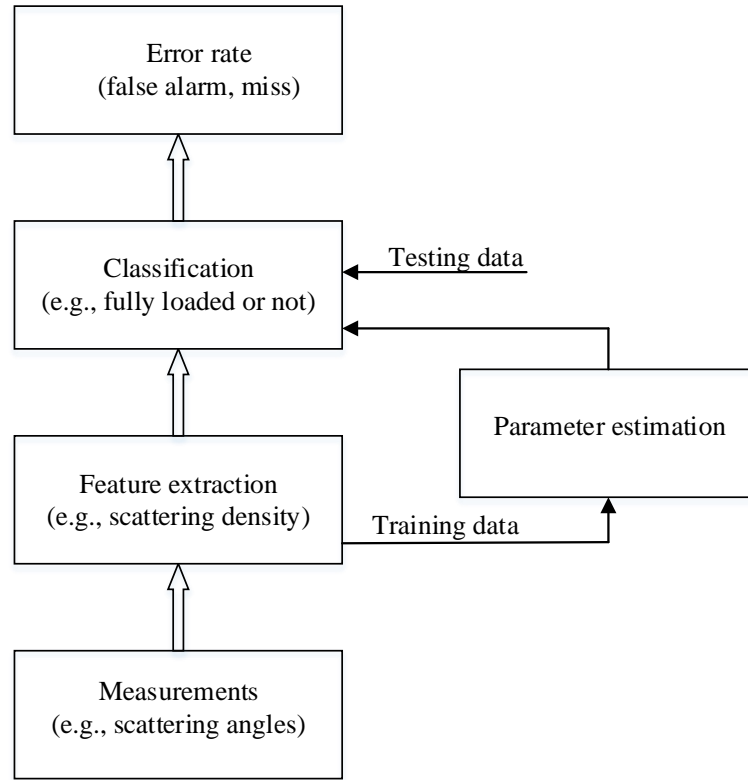


Figure 4-2. Classifier block diagram

The selected decision rule minimizes the risk associated with a decision:

$$R(\delta) = \underset{\delta}{\operatorname{argmin}} \mathbb{E}_{Y\Theta} [C(\delta(Y), \Theta)] \quad (4-21)$$

where  $\mathbf{Y}$  is the accumulated dataset with muon measurements,  $C(\delta(\mathbf{Y}), \Theta)$  is the cost of selecting category  $\delta(\mathbf{Y})$  when the true decision is  $\Theta$ . A sealed container either fully or partially loaded represents two distinct categories. Let the two categories represented as  $H_0$  and  $H_1$ . Samples from a fully loaded cask, i.e., category  $H_0$ , follow distribution  $f_0(y)$  with zero mean, variance  $\sigma_0^2$  and prior probability  $\pi_0$ ,  $H_0: \mathbf{Y} \sim f_0(y)$ . Samples from a partially loaded cask, i.e., category  $H_1$ , follow distribution  $f_1(y)$  with zero mean, variance  $\sigma_1^2$  and prior probability  $\pi_1$ ,  $H_1: \mathbf{Y} \sim f_1(y)$ . The cost for selecting category  $H_i$  when the true



category is  $H_j$  would be  $C_{ij}$ . In this case, the decision rule that minimizes the overall risk is:

$$C_{00}\pi_0(y) + C_{01}\pi_1(y) \leq_{H_1}^{H_0} C_{10}\pi_0(y) + C_{11}\pi_1(y) \Rightarrow \quad (4-22)$$

$$\frac{f_1(y)}{f_0(y)} \leq_{H_1}^{H_0} \frac{(C_{10} - C_{00})\pi_0}{(C_{01} - C_{11})\pi_1} \quad (4-23)$$

Setting the ratio of the likelihood functions to  $L(y)$  and the right hand side of the inequality to  $\tau$ , the decision rule can be written in compact form:

$$\mathcal{L}(y) \leq_{H_1}^{H_0} \tau \quad (4-24)$$

This decision rule suggests that in order to minimize the risk, category  $H_0$  must be selected when the likelihood ratio is smaller than the boundary value  $\tau$  or select category  $H_1$  when the likelihood ratio is larger than the boundary value  $\tau$ . Let  $N$  muon measurements are obtained from muon detectors placed around a dry cask:

$$\mathbf{Y} = [y_1, y_2, \dots, y_N]^T \quad (4-25)$$

These measurements are independent and identically distributed and the likelihood function is:

$$f_j(y) = \prod_{i=1}^N f_j(y_i) = \frac{1}{(2\pi\sigma_j^2)^{N/2}} e^{-\frac{1}{2\sigma_j^2} \sum_{i=1}^N y_i^2} \quad (4-26)$$

Using the likelihood ratio test, the following decision rule can be derived:

$$\sum_{i=1}^N y_i^2 \leq_{H_1}^{H_0} \frac{2\sigma_1^2\sigma_0^2 N \ln \frac{\sigma_1}{\sigma_0}}{(\sigma_1^2 - \sigma_0^2)} + \frac{2\sigma_1^2\sigma_0^2 \ln \tau}{(\sigma_1^2 - \sigma_0^2)} \quad (4-27)$$

This rule depends on the number of measurements  $N$ , the variances  $\sigma_0^2$ ,  $\sigma_1^2$  and value  $\tau$ . Value  $\tau$  includes the cost associated with each decision and the priors. Dividing by the

number of measurements  $N$ , a decision rule that provides an estimate of the scattering variance is derived:

$$\frac{1}{N} \sum_{i=1}^N y_i^2 \leq_{H_1}^{H_0} \frac{2\sigma_1^2 \sigma_0^2 \ln \frac{\sigma_1}{\sigma_0}}{(\sigma_1^2 - \sigma_0^2)} + \frac{2\sigma_1^2 \sigma_0^2 \ln \tau}{N(\sigma_1^2 - \sigma_0^2)} \Rightarrow \quad (4-28)$$

After further rearrangement, this gives:

$$\frac{1}{N} \sum_{i=1}^N y_i^2 \leq_{H_1}^{H_0} \frac{2\sigma_1^2 \sigma_0^2}{(\sigma_1^2 - \sigma_0^2)} \left[ \ln \frac{\sigma_1}{\sigma_0} + \frac{\ln \tau}{N} \right] \quad (4-29)$$

A classifier using the above decision rule is an optimal classifier having a separation boundary that can be written as the sum of two terms, where the first term depends solely on the characteristics of the scattering distribution whereas the second term depends on the number of measurements, the priors and the associated cost for each classification decision. Asymptotically, as the number of input measurements  $N$  approaches infinity the second term decreases and the decision rule will depend only on the first term. Furthermore, for uniform cost and equal priors,  $\tau=1$ , the second term vanishes.

#### d. Performance evaluation

The performance of the Bayesian classifier, for uniform cost, is characterized by the probability of error:

$$\mathbb{P}_{error} = \pi_0 \mathbb{P}(H_1|H_0) + \pi_1 \mathbb{P}(H_0|H_1) = \pi_0 \mathbb{P}_F + \pi_1 \mathbb{P}_M \quad (4-30)$$

where  $\mathbb{P}_F = \mathbb{P}(H_1|H_0)$  is the probability of selecting  $H_1$  when the correct is  $H_0$  and  $\mathbb{P}_M = \mathbb{P}(H_0|H_1)$  is the probability of selecting  $H_0$  when the correct is  $H_1$ . The performance of the algorithm depends on the prior probabilities,  $\pi_0$  and  $\pi_1$ , as well as the probabilities

of false alarm  $P_F$  and miss  $P_M$ . To evaluate the algorithm performance, the GEANT4 scattering variance estimates, calculated in Chapter 3, were used as reference values for the parameters of the scattering variance distributions, i.e.,  $\sigma_0^2$  and  $\sigma_1^2$ .  $\sigma_0^2$  corresponds to a fully loaded dry cask,  $\sigma_1^2$  to a dry cask where fuel assemblies are missing. The larger the difference between these two quantities,  $\sigma_0^2$  and  $\sigma_1^2$ , the larger the separation between the distributions resulting in improved classification. The relative difference between a two dry casks is defined as:

$$d = \frac{\sigma_0^2 - \sigma_1^2}{\sigma_0^2} \times 100\% \quad (4-31)$$

The relative difference ranges from 0, when the variances of  $H_0$  and  $H_1$  are the same, to 50%, when the dry cask is empty. Muons were repeatedly drawn from this distribution and compared to the classifier threshold from equation (4-22). 100,000, 200,000 and 300,000 muons were simulated and the error rate was calculated as a function of the relative difference for priors  $\pi_0=0.9$  and  $\pi_1=0.1$ . 1,000 simulations were used as testing data to calculate the number of misclassifications. The above procedure was repeated 100 times and the resulting error rate was calculated, for two different sets of priors and number of muons, and is shown in Figures 4-3 and 4-4. The results demonstrate that the error rate is decreasing with increasing relative difference between dry casks. The relative difference corresponding to zero error rate decreases with increasing muon measurements. A dry cask that has relative difference more than 1.5% from a fully loaded can be distinguished with zero error rate for as low as  $N=300,000$  muons. Relative difference of 1.5% corresponds to one fuel assembly missing. Relative difference of more than 3% can be correctly identified with even less muons, as low as 100,000. Figure 4-5

shows that the effect of priors diminishes as the relative difference increases beyond 1.5% and 300,000 muons. A relative difference from a fully loaded dry cask in the order of 1.5% or more is needed to reduce the error rate to zero for 300,000 muons. The detection, miss and false alarm rates for 100,000 muons are shown in Figures 4-6 and 4-7. An increasing relative difference results in increased detection rate, which for values higher than 3% approaches 100% independent of the prior. For small relative differences, the miss rate becomes important whereas false alarm rate is remains negligible for  $\pi_1=0.1$  and becomes larger for  $\pi_1=0.5$ . This behaviour recommends that when small quantities of fuel have been removed from a dry cask, there is a considerable probability of not being detected. It is noted that miss rate may represent a more undesirable situation in terms of safeguards and non-proliferation than a false alarm rates.

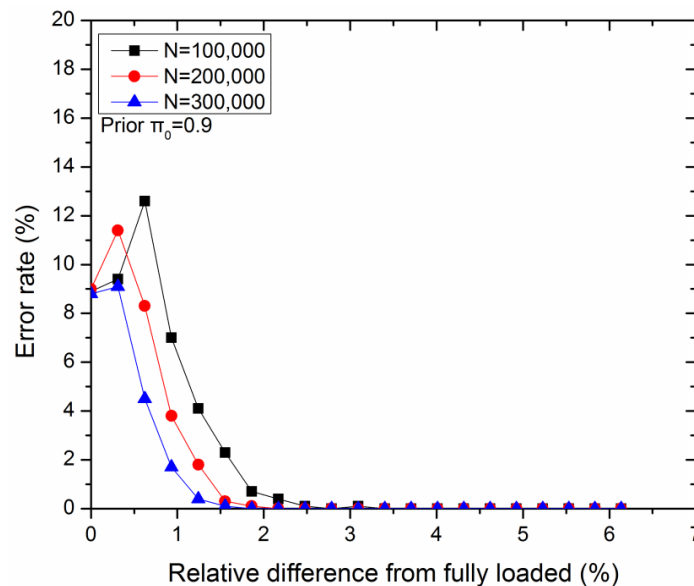


Figure 4-3. Error rate as a function of the relative difference between two dry casks and prior  $\pi_0=0.9$ . Error rate tends to zero with increasing amount of removed material.

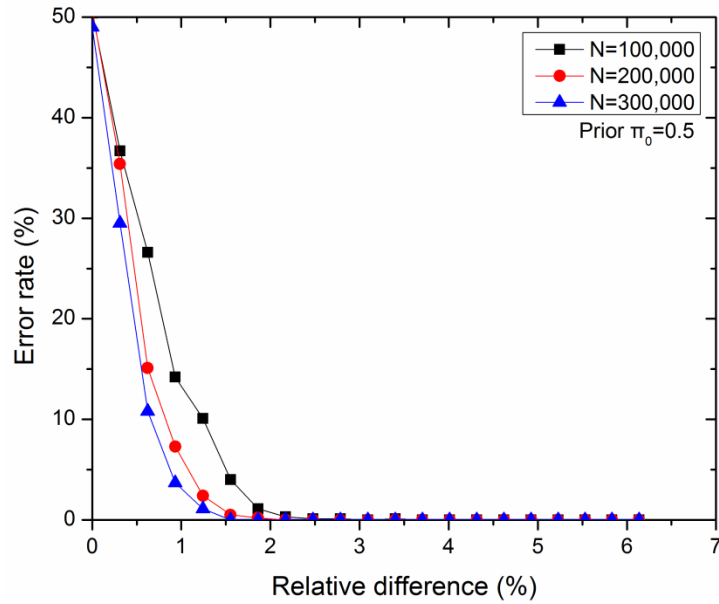


Figure 4-4. Error rate as a function of the relative difference between two dry casks and prior  $\pi_0=0.5$ .

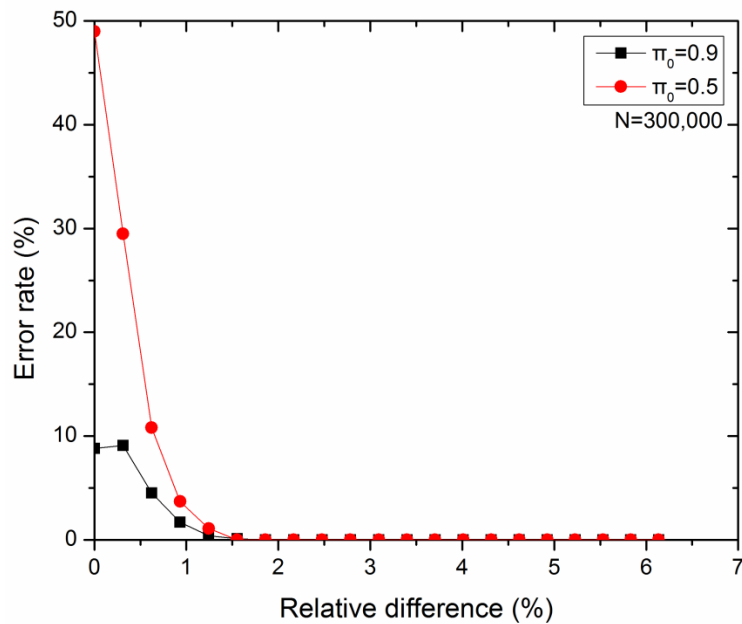


Figure 4-5. Error rate as a function of two different priors,  $\pi_0=0.9$  and  $\pi_0=0.5$ . Error rate tends to zero for relative difference larger than 1.5%.

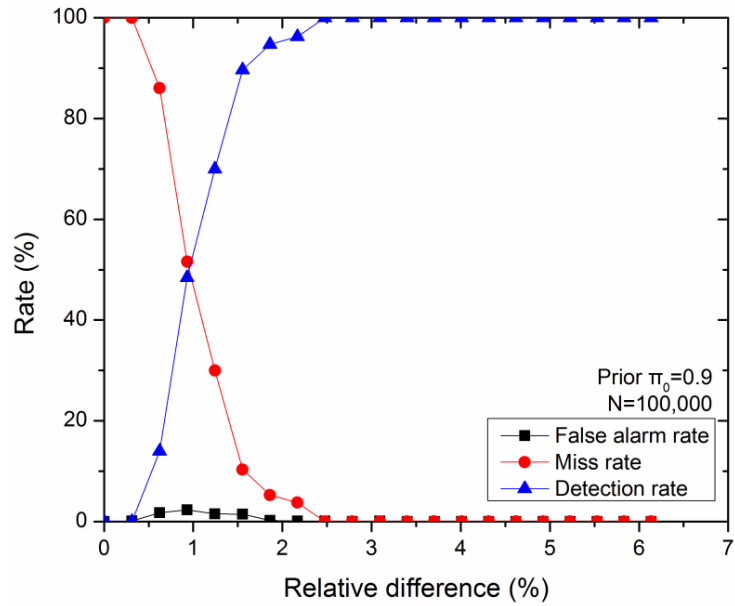


Figure 4-6. Detection, miss and false alarm rate as a function of the relative difference for prior  $\pi_0=0.9$  and  $N=100,000$  muons.

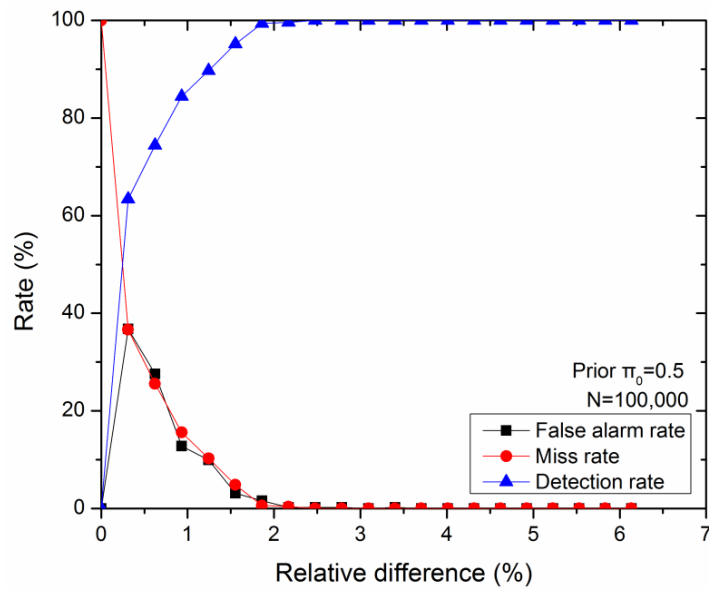


Figure 4-7. Detection, miss and false alarm rate as a function of the relative difference for prior  $\pi_0=0.5$  and  $N=100,000$  muons.

Calculation of the probability of error is not analytically tractable and therefore having an upper bound can become useful. The probability of error is always less than or equal to the upper bound:

$$\mathbb{P}_{error} \leq \mathbb{P}_{upper\ bound} \quad (4-32)$$

Two upper bounds are presented that can be easily calculated and provide estimates of the probability of error. The Chernoff bound [70]:

$$\mathbb{P}_{Chernoff}(\beta) = \pi_0^\beta \pi_1^{1-\beta} e^{-f(\beta)} \quad (4-33)$$

where:

$$f(\beta) = \frac{\beta(1-\beta)}{2} (\mu_1 - \mu_0)^T [\beta \Sigma_0 + (1-\beta) \Sigma_1]^{-1} (\mu_1 - \mu_0) + \frac{1}{2} \ln \left( \frac{|\beta \Sigma_0 + (1-\beta) \Sigma_1|}{|\Sigma_0|^\beta |\Sigma_1|^{1-\beta}} \right) \quad (4-34)$$

For  $0 \leq \beta \leq 1$ . Maximizing the function  $f(\beta)$  one can find the value  $\beta$  which gives the smallest error bound. The Bhattacharyya bound is derived from the Chernoff bound simply by replacing with  $\beta=0.5$  [70]:

$$\mathbb{P}_{Bhattacharyya} \left( \frac{1}{2} \right) = \sqrt{\pi_0 \pi_1} e^{-f(1/2)} \quad (4-35)$$

where:

$$f \left( \frac{1}{2} \right) = \frac{1}{8} (\mu_1 - \mu_0)^T \left[ \frac{\Sigma_0 + \Sigma_1}{2} \right]^{-1} (\mu_1 - \mu_0) + \frac{1}{2} \ln \left( \frac{\left| \frac{\Sigma_0 + \Sigma_1}{2} \right|}{|\Sigma_0|^{\frac{1}{2}} |\Sigma_1|^{\frac{1}{2}}} \right) \quad (4-36)$$

The Chernoff and Bhattacharyya error bounds are shown in Figures 4-8 and 4-9. As expected the Bayesian error is smaller but the difference tends to decrease for larger relative differences.

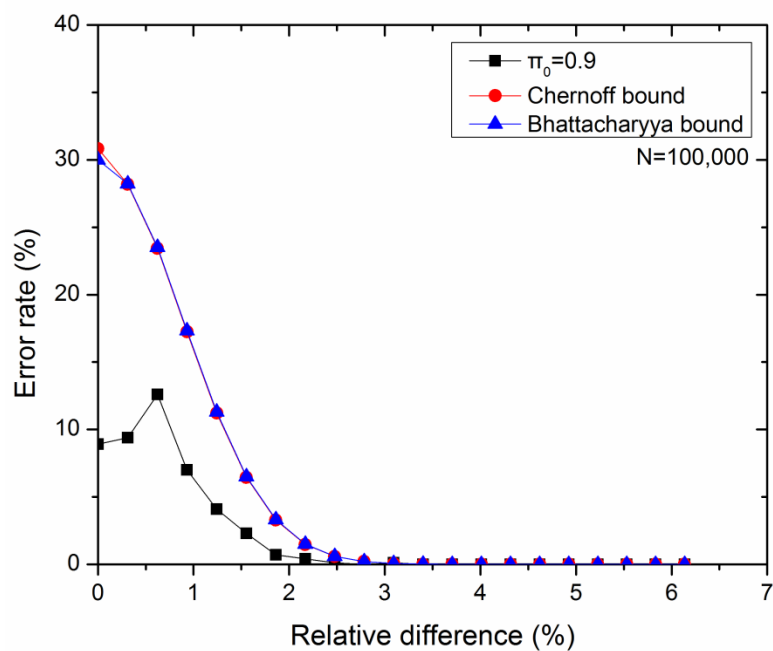


Figure 4-8. Chernoff and Bhattacharyya bounds compared to error rate for prior  $\pi_0=0.9$  and  $N=100,000$  muons.

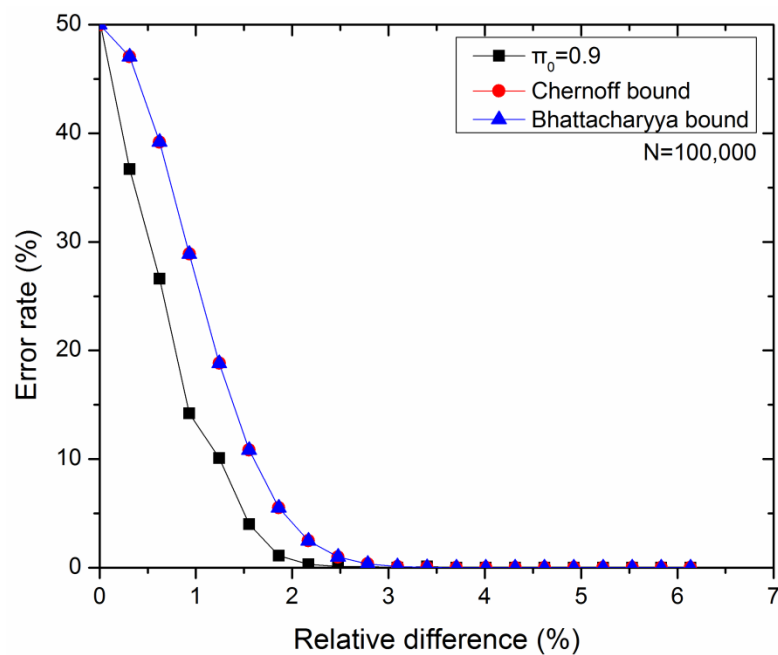


Figure 4-9. Chernoff and Bhattacharyya bounds compared to error rate for prior  $\pi_0=0.5$  and  $N=100,000$  muons.



### e. Receiver Operating Characteristic

The structure of the Bayesian algorithm relies on accurate knowledge of priors and cost function. When this knowledge is not readily available, instead of guessing, we could select the threshold that will maximize the detection rate while keeping the false alarm rate below a preselected value. From equation (4-10) the Bayesian risk is parametrized by the pair  $(P_D, P_F)$  and it would be desirable to select a decision boundary where  $P_D$  is as close to 1 (or 100%) as possible and  $P_F$  as close to zero as possible. The Receiver Operating Characteristic (ROC) is a technique for visualizing the tradeoff between detection and false alarm rates [71]. To obtain the ROC curve the decision boundary  $\tau$  is varied from  $+\infty$  to 0. Each location of the decision boundary generates a different pair  $(P_D, P_F)$ . The decision boundary of  $+\infty$  produces the point (0, 0). As the boundary is further reduced the curve moves up and to the right ending up at the point (1, 1). Figure 4-10 shows one ROC curve for  $N=50,000$  muons and the corresponding decision boundaries for uniform cost. If an acceptable false alarm rate would be  $<10\%$  then the maximum detection rate that can be achieved is  $\sim 90\%$ . Figure 4-11 shows the ROC curve for a relative difference of  $d=1.5\%$  and varying muon measurements. Increasing muon measurements results in smaller false alarm rates and improved detection performance. In this case, a maximum detection rate of 90% can be achieved for a false alarm rate lower than 1%.

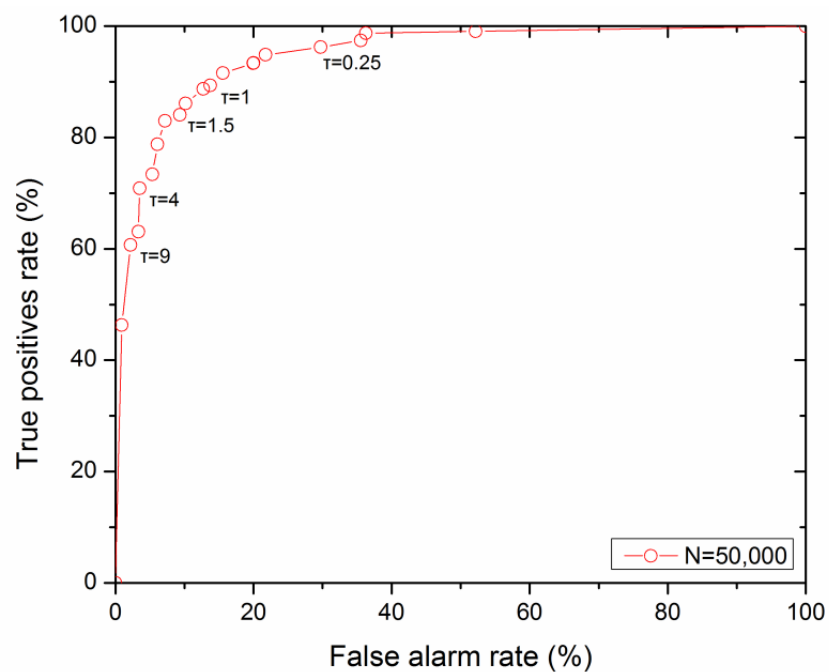


Figure 4-10. ROC curve for 50,000 muons. The threshold values  $\tau$  are also shown.

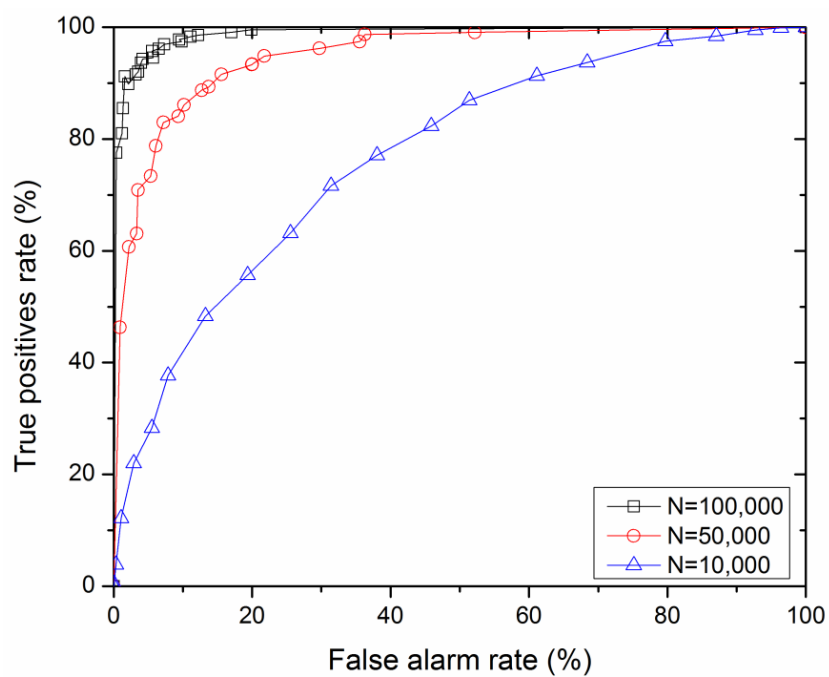


Figure 4-11. ROC curve for 10,000, 50,000 and 100,000 muons.

### f. Minimax hypothesis testing

The Bayesian formulation requires that the prior probabilities ( $\pi_0, \pi_1$ ) are known and can be assigned to the two classes  $H_0$  and  $H_1$ . However, exact knowledge of the prior probabilities is not always available. An alternative to ROC method would be to select a conservative decision boundary for the least favourable choice of priors. The Minimax hypothesis testing assigns priors that will minimize the Bayesian risk independent of the actual priors [69, 70]. The Bayes risk is linear in prior  $\pi_0$  and we seek to find a decision rule and a prior value  $\pi_{0M}$  that will solve the minimax problem [69]:

$$(\delta_M, \pi_{0M}) = \arg \min_{\delta} \max_{0 \leq \pi_0 \leq 1} R(\delta, \pi_0) \quad (37)$$

The error rate for  $d=1.5\%$  was calculated for  $\pi_0$  ranging from 0 to 1. The results for different number of muons are shown in Figure 4-12. The least favorable prior is obtained and is the same for independent of the number of muons,  $\pi_{0M}=0.5$ .

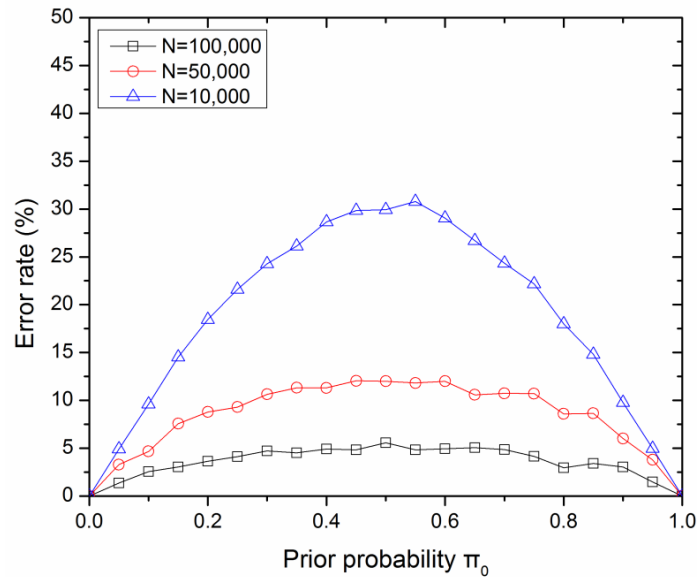


Figure 4-12. Error rate as a function of the prior probability  $\pi_0$  for three different muon measurements.

g. Comparison with other classification algorithms

Two well-known classification algorithms, Support Vector Machines (SVM) and k-Nearest Neighbors (kNN) are compared to the Bayesian monitoring algorithm. SVM [72] and kNN [73] classifiers are simple, widely used and demonstrate good performance over a large number of classification tasks. SVM and kNN algorithms are non-parametric learning algorithms in the sense that no assumption is needed for the underlying distribution or the prior distributions. SVM find the decision boundary that maximizes the distance between the data points of the two classes. SVM can accept several kernel functions, depending on the desired type of the decision boundary. In the present work, SVM with linear kernel function were used as the distributions can be linearly separated. On the other hand, SVM have to be trained with a predetermined set of training points in order to find the optimal decision boundary. The training was performed using 2000 training data randomly drawn from the derived scattering variance probability distributions. The data generated with prior probabilities  $\pi_0=0.9$  and  $\pi_0=0.5$ . The SVM performance was tested with 1000 testing data randomly drawn from the derived scattering variance probability distributions. The error rate was calculated and the process was repeated 100 times to determine the average error rate. The results for  $N=300,000$  muons and two different prior probabilities are shown in Figures 4-13 and 4-14. The calculated error rate from the Bayesian monitoring algorithm is also shown. The SVM algorithm has similar behavior with the Bayesian algorithm, although the Bayesian algorithm slightly outperforms the SVM error rate.

kNN finds the k-th nearest neighbour and does a majority voting. The number of nearest neighbors is pre-determined by the user, for example it can be  $k=1$  or  $k=5$  or higher.

Typically,  $k$  is odd for binary hypothesis testing and the higher it is, the more robust the algorithm is, although this can be quite computationally expensive. In the present work, it was observed that larger  $k$  values lead to improved performance. The value of  $k=5$  was then selected as a compromise between performance and computational complexity. For larger values, the computational time needed becomes significant with only small performance improvement. The metric used to determine the nearest neighbors can vary depending on the data. In the present work, the Euclidean distance was chosen. Similarly to SVN, 2000 training data were used from the derived scattering variance probability distribution. The prior probability with which the data were generated were  $\pi_0=0.9$  and  $\pi_0=0.5$ . The kNN was tested with 1000 testing data. The error rate was calculated and the process was repeated 100 times to determine the average error rate. The results for  $N=300,000$  muons and two different prior probabilities are shown in Figures 4-13 and 4-14 and compared with the error rate from the Bayesian monitoring algorithm. The Bayesian algorithm slightly outperforms the kNN error rate.

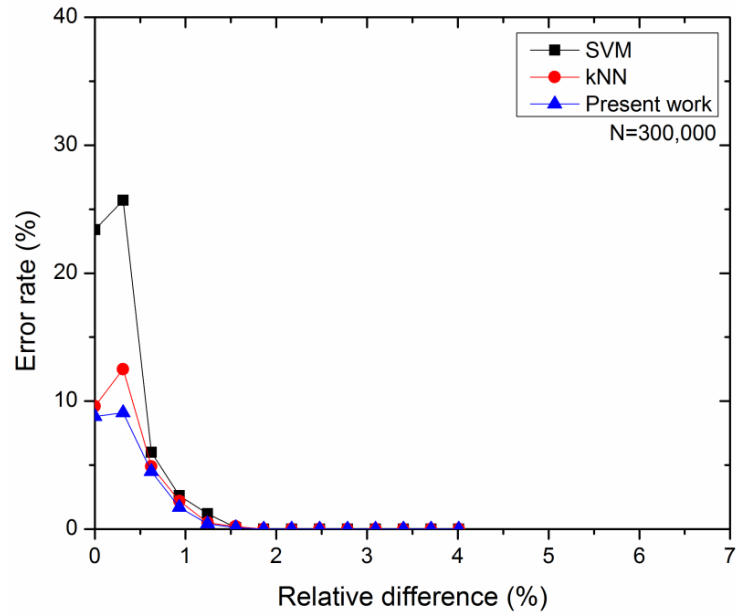


Figure 4-13. SVM and kNN error rate for 300,000 muons and  $\pi_0=0.9$ . The error rate from the Bayesian algorithm is also shown.

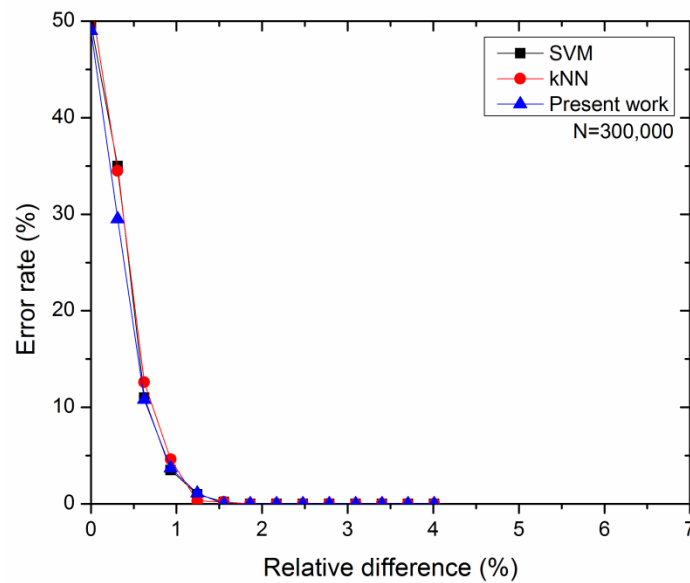


Figure 4-14. SVM and kNN error rate for 300,000 muons and  $\pi_0=0.5$ . The error rate from the Bayesian algorithm is also shown.

## h. Summary

The applicability of muons for monitoring dry casks based on their spent nuclear fuel content was investigated in this chapter. A decision rule to classify dry cask which minimizes the risk of making an incorrect decision was derived using Bayesian principles. The classifier using the derived decision rule can be written as the sum of two terms, where the first term depends solely on the characteristics of the scattering distribution whereas the second term depends on the number of measurements, the priors and the associated cost for each classification decision. The performance of the proposed monitoring algorithm was evaluated in terms of error rate, detection rate, miss and false alarm rate. The results demonstrate that a dry cask that has relative difference more than 1.5% from a fully loaded which corresponds to one fuel assembly missing can be distinguished with zero error rate for as low as  $N=300,000$  muons. Relative difference of more than 3% can be correctly identified with even less muons, as low as 100,000. The Chernoff and Bhattacharyya bounds were calculated and compared with the monitoring algorithm. The ROC and minimax curves were provided as an alternative when prior probabilities and cost function are not known. It was shown that increasing muon measurements results in smaller false alarm rates and improved detection performance and that a maximum detection rate of 90% can be achieved for a false alarm rate lower than 1% with 100,000 muons for a relative difference of  $d=1.5\%$ . Finally, the proposed algorithm was compared with the available from the literature SVM and kNN algorithms. The SVM and kNN algorithms have similar behavior with the Bayesian algorithm, although the Bayesian algorithm slightly outperforms in terms of error rate.

## CHAPTER 5. SPENT NUCLEAR FUEL IMAGING

In this chapter, dry cask imaging using muon scattering and transmission is investigated. The imaging reconstruction framework is outlined in Section 5.1 and the Point of Closest Approach (PoCA) imaging algorithm is presented in Section 5.2. The objective is to design an algorithm that is optimal in the sense it minimizes the overall risk associated with a classification decision. Preliminary results on cubes and simplified dry casks using PoCA are shown in Section 5.3. Full scale dry cask imaging using muon scattering is evaluated in Section 5.4 and imaging using muon transmission is analyzed in Section 5.5. The scenarios include dry casks (a) fully loaded with 24 PWR fuel assemblies, (b) half loaded, (c) one row of fuel assemblies missing, (d) one fuel assembly missing and, (e) empty. The effect of detector size and number of muons measured on image resolution is evaluated. Limitations and improvements are presented and discussed in Section 5.6. The chapter concludes with the main findings in Section 5.7.

### a. Image Reconstruction framework

Image reconstruction of an object refers to the ability to reproduce 2D and 3D images of the illuminated object from measurements. Measurements carry information related to the rays-object interactions. X-ray attenuation or muon scattering can be a dataset of measurements. Obtaining multiple measurements from different directions allows



recovery of cross-sectional images. This process is commonly known as tomography and refers to the reconstruction of an object from projections. The mathematical foundation of reconstruction from projections dates back to Radon transform. Radon derived a solution to the problem of function reconstruction from projections. However, tomographic imaging was significantly improved after Hounsfield's invention of the x-ray computed tomographic scanner. Reconstruction methods have found a wide range of applications in medical imaging and their use is now extended to other areas such as volcano imaging and more recently muon tomography.

Reconstruction algorithms can be classified in two classes: filtered backprojection algorithms (FBP) and algebraic reconstruction techniques (ART). In situations where a large number of evenly spaced projections is not available or significant scattering takes place along the ray path, both necessary conditions for FBP methods, a solution can be provided using algebraic techniques. In the ART approach, a grid is superimposed on top of the object, each grid pixel contains the unknown object function and a set of algebraic equations is set up for the determination of the unknown function. A necessary condition for ART is the correct estimation of the ray paths that between the source and detector. ART are conceptually simpler than the FBP but computationally expensive.

A separate category of reconstruction algorithms, that don't belong to any of the above two methods, are based on geometrical and heuristic ground. The Point of Closest Approach (PoCA) algorithm, developed by LANL, has found useful applications in cargo scanning and reactor imaging with muons. The algorithm is based on the assumption that muons are scattered in a single point which is assigned into a voxel. The algorithm ignores multiple Coulomb scattering and that results in significant blur in the

reconstructed images and presents certain limitations to the image resolution. Although algebraic reconstruction techniques have better resolution are far more computationally demanding than PoCA. PoCA is a relatively fast algorithm compared to other reconstruction algorithms and is suitable for reconstructing large geometries with thousands of voxels, e.g., dry casks, within a reasonable amount of time. However, the image quality in most cases is adequate to discriminate between different materials and identify the location of the object under interrogation. The PoCA algorithm is used herein to reconstruct dry cask loaded with various amounts of spent nuclear fuel.

#### b. Reconstruction using PoCA

The PoCA algorithm determines the point of closest approach between two lines. The POCA processes the accumulated dataset of muon positions and calculates the point where the incoming and outgoing muon trajectories coincide. In our case, these two lines are the incoming and outgoing trajectories of muons. The incoming and outgoing positions of muons are known from detector measurements. The positions are then used to calculate the incoming and outgoing trajectories and compute the scattering angle for each muon. The algorithm calculates the point of closest approach between the incoming and outgoing trajectories which in 2D is the intersection of the two lines. For the 3D case, in which the trajectories may not intersect, the algorithm calculates the minimum distance between the incoming and outgoing muon trajectories. The scattering event is taken at the middle point of that distance and the scattering angle is assigned to a pixel on a 2D grid or a voxel on a 3D grid. The concept is shown in Figure 5-1. The algorithm depends on

the number of muons passing through the object volume and presents computational complexity  $O(N)$  [22].

During the reconstruction, each pixel in 2D (voxel in 3D) contains a parameter associated with the scattering angles of muons passing through that point. This parameter can be the average squared scattering angle, the squared average scattering angle or the median. It is expected that materials with high-Z will appear with higher parameter values in the reconstructed images as a result of increased scattering in this location. Those voxels having high values would represent high-Z materials where muons scattered significantly. The PoCA algorithm used herein can be formulated mathematically as follows. Let  $L_1$  represent the incoming trajectory and  $L_2$  the outgoing trajectory. The algorithm first calculates the minimum distance between the two lines, described mathematically as follows:

$$dist(L_1, L_2) = \min dist(P, Q) \quad (5-1)$$

where P, Q are points on the incoming trajectory  $L_1$  and the outgoing trajectory  $L_2$ , respectively. Applying analytical geometry principles, we find two points where the minimum distance between the two lines occurs:

$$d = dist(L_1, L_2) = |P(s_c) - Q(t_c)| \quad (5-2)$$

The two lines can be written in 3-dimensional space:

$$L_1 := P(s) = P_0 + s(P_1 - P_0) = P_0 + s\mathbf{u} \quad (5-3)$$

$$L_2 := Q(t) = Q_0 + t(Q_1 - Q_0) = Q_0 + t\mathbf{v} \quad (5-4)$$

where  $P_0$  and  $Q_0$  are points on lines  $L_1$  and  $L_2$ , respectively. The direction vectors are  $\mathbf{u}$  and  $\mathbf{v}$ ,  $s$  and  $t$  represent the line parameters. The minimum distance is then given by the following expression:

$$d = \left| (P_0 - Q_0) + \frac{(be - cd)\mathbf{u} - (ae - bd)\mathbf{v}}{ac - b^2} \right| \quad (5-5)$$

where  $a=\mathbf{u}\cdot\mathbf{u}$ ,  $b=\mathbf{u}\cdot\mathbf{v}$ ,  $c=\mathbf{v}\cdot\mathbf{v}$ ,  $d=\mathbf{u}\cdot\mathbf{w}_0$ ,  $e=\mathbf{v}\cdot\mathbf{w}_0$ , and  $\mathbf{w}_0=\mathbf{P}_0-\mathbf{Q}_0$ . The point of the closest approach is located midway through the minimum distance and is associated with a single pixel on a 2D grid or a voxel on a 3D grid (Figure 5-1). At the estimated point of scatter the following signal value is assigned:

$$s_i = \frac{1}{2} \left[ (\theta_x^{out} - \theta_x^{in})^2 + (\theta_y^{out} - \theta_y^{in})^2 \right] \quad (5-6)$$

where  $\theta_x$  and  $\theta_y$  are the projected angles. As more muons pass through the object volume, each pixel (or voxel) is filled with scattering angles. The final value of each voxel is the average scattering angle divided by the voxel size  $L$ :

$$Voxel\ value = \frac{1}{NL} \sum_{i=1}^N s_i \quad (5-7)$$

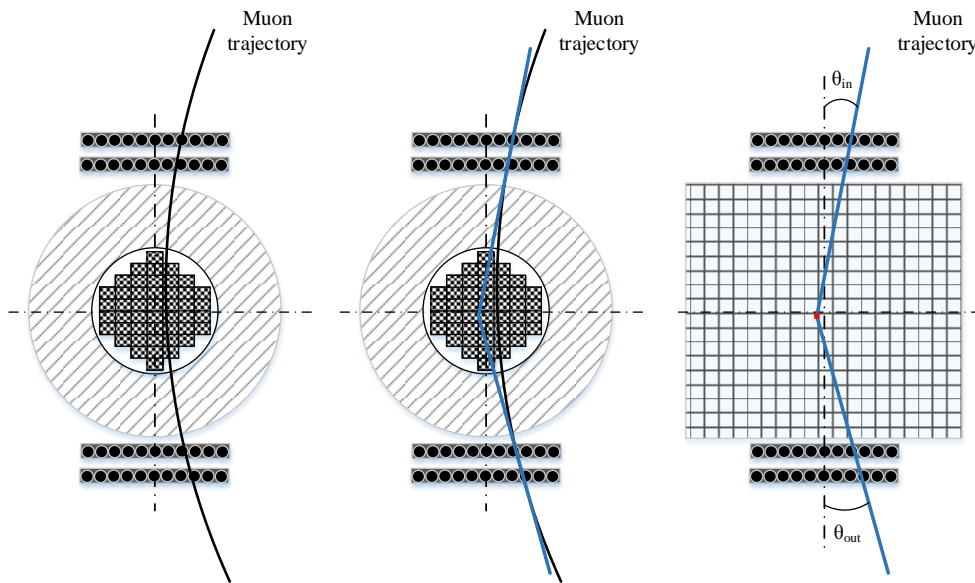


Figure 5-1. PoCA algorithm principle (left: muon trajectory through muon detectors, spent nuclear fuel and dry cask, center: extrapolated linear incoming and outgoing trajectories, right: superimposed grid and assigned scattering point)

### c. Preliminary results using POCA

The PoCA algorithm was initially used to reconstruct simplified GEANT4 models of  $10 \times 10 \times 10 \text{ cm}^3$  cubes made of different materials. 10,000 polyenergetic (1-60 GeV) muons were generated and their interactions with different cubes, made of Al, Fe, Pb and U, were simulated. The incoming and outgoing trajectories were stored and analyzed. The results are shown in Figure 5-2; the color scale represents the magnitude of scattering angles. The algorithm reconstructs correctly the shape of each cube, shown in Figure 5-2 with a white rectangle.

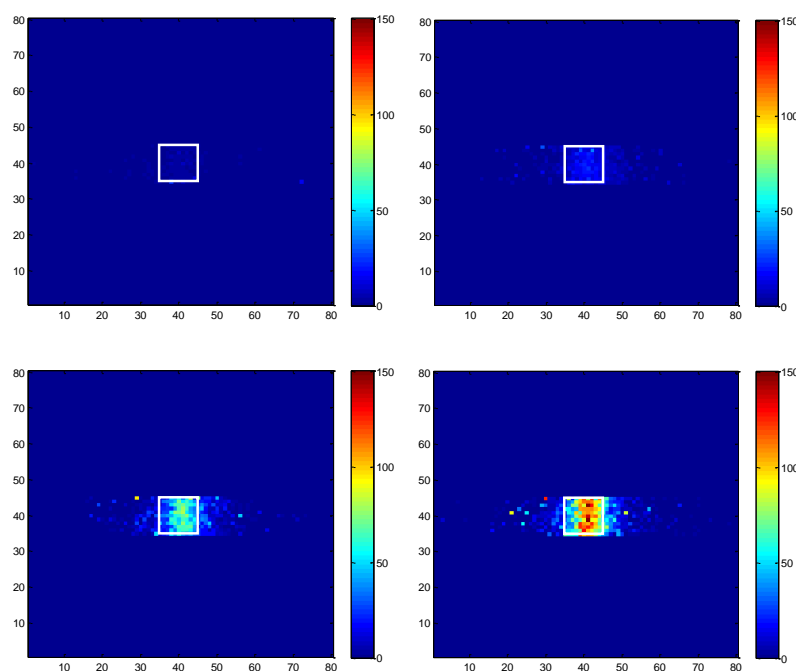


Figure 5-2. PoCA imaging of different cubes (upper left: Al, upper right: Fe, lower left: Pb, lower right: U). The scale represents the strength of the scattering angle.

It is noted that for cubes made of Pb and U, scattering points have been allocated outside the rectangle area. The boundaries of the object cannot be distinguished accurately. This

represents an inherent limitation of the algorithm which allocates points outside the object boundaries due to the single scattering assumption. This effect is shown schematically in Figure 5-3. For all plots shown, Y-axis is oriented vertically, X-axis is oriented parallel to the detector planes and Z-axis is vertical to the detector planes.

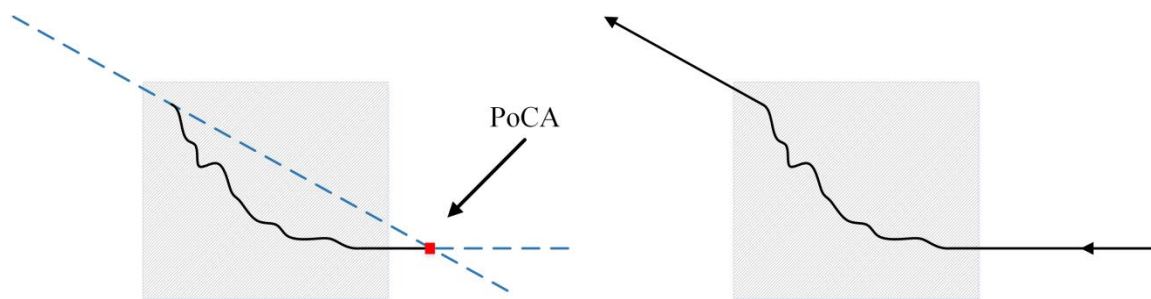


Figure 5-3. Representation of an incorrect scattering point assignment by the PoCA imaging algorithm.

The PoCA algorithm was tested in the reconstruction of simplified vertical and horizontal dry casks to identify additional limitations. A fully loaded dry cask consists of an iron overpack and a cylindrical solid made of  $\text{UO}_2$  located at the center of the overpack. An empty dry cask consists only of the concrete overpack. The detectors (green color) are modeled as parallel planes of drift-wire chambers that can record the position of each muon before and after interaction with the dry cask. Each muon will result in four recorded position measurements, two position before interacting with the object and two after. For the reconstruction,  $10^6$  muons with energies 1-60 GeV and a grid with  $40 \times 40$  pixels of size 10 cm was used. In the upper row of Figure 5-4, the model of a simplified fully loaded dry cask is shown and in the lower row the model of an empty dry cask is shown. In the right column, horizontal slices, parallel to the direction of the muons, using the PoCA imaging algorithm are shown. The slices are taken at the object centerline. The

middle column shows the imaging result if a perfect imaging algorithm was employed. It appears that the PoCA algorithm can correctly reproduce the cylindrical shape and allow differentiation between the overpack (iron) and the fuel. Several points have been assigned to pixels outside the object boundaries but the shape can still be adequately identified. However, for the empty dry cask, the center, which is filled with air, is interpreted incorrectly by the algorithm as iron. Vertical slices are shown in Figure 5-5. The slices are taken at the object centerline. Similarly, the fully loaded cask is correctly reconstructed and the fuel location can be identified. The empty cask is reconstructed incorrectly and shown with its center occupied by the same material as the outside. This effect is shown in Figure 5-6. It appears that for dense multilayered materials the algorithm assigns scattering points outside the material boundaries. This limitation is reduced for horizontal dry casks, as shown in Figure 5-7. In this case, both the fully loaded and empty dry casks are correctly reconstructed. It is therefore expected that better resolution can be achieved when imaging horizontal dry casks than vertical dry casks.

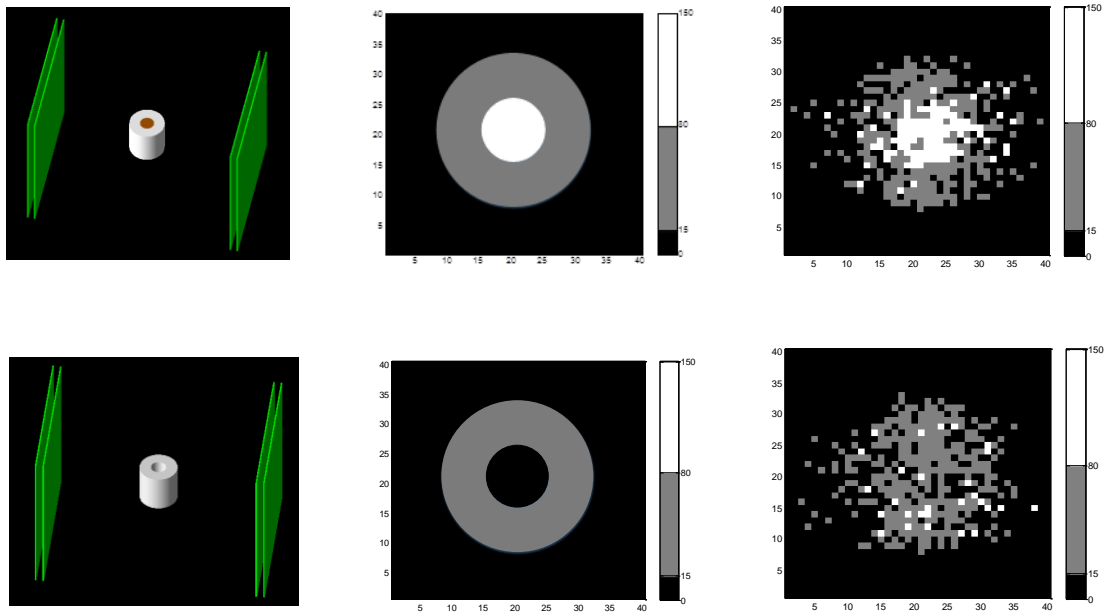


Figure 5-4. Horizontal slices of a simplified vertical dry cask (left: GEANT4 model, center: images using a perfect algorithm, right: obtained images using PoCA).

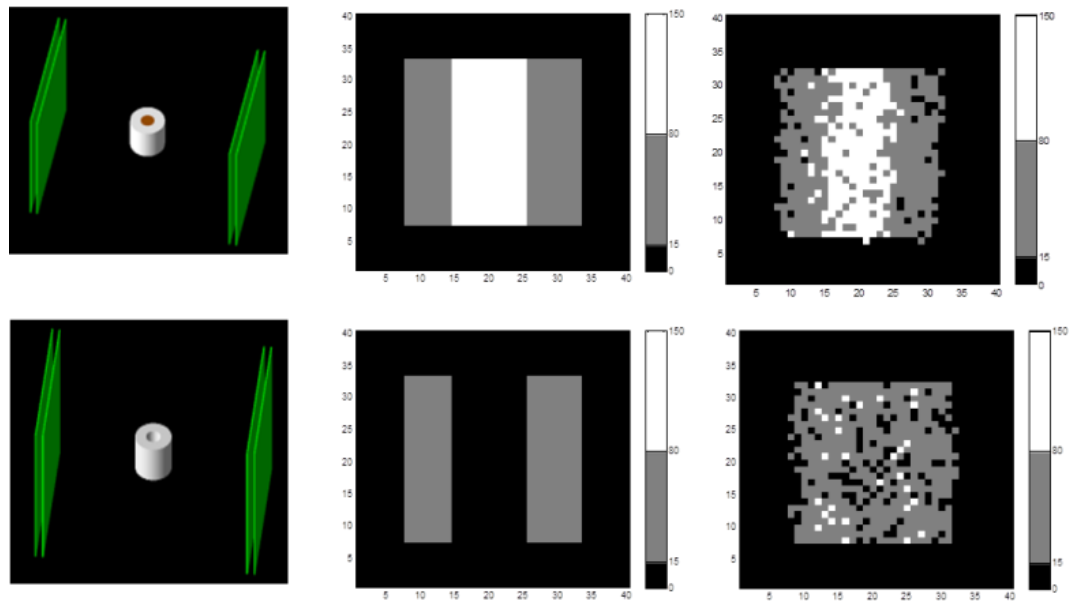


Figure 5-5. Vertical slices of a simplified vertical dry cask (left: GEANT4 model, center: images using a perfect algorithm, right: obtained images using PoCA).



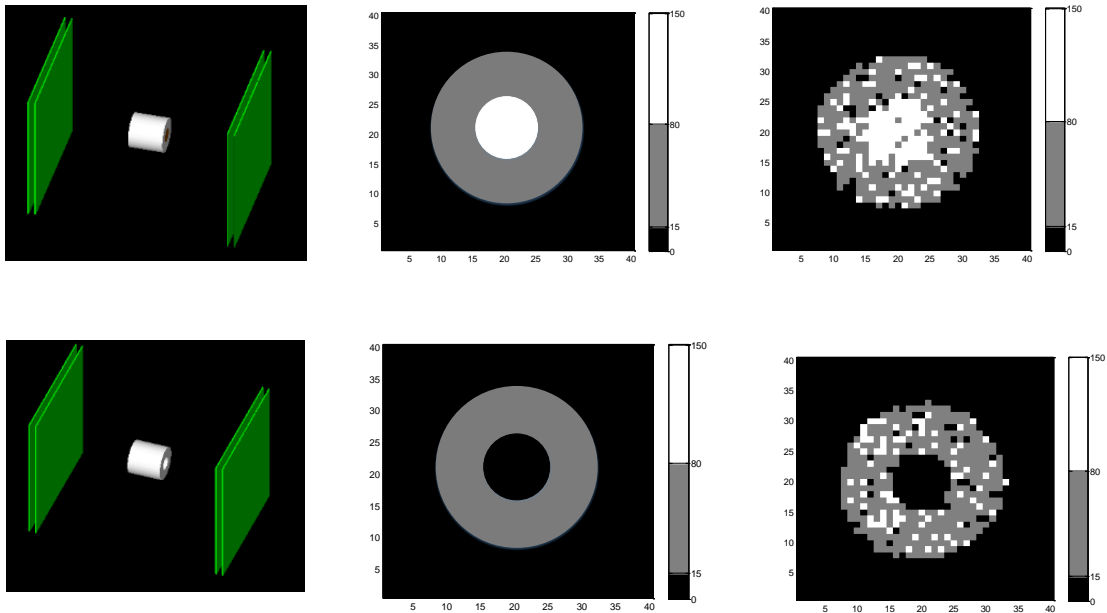


Figure 5-6. Vertical slices of a simplified horizontal dry cask (left: GEANT4 model, center: images using a perfect algorithm, right: obtained images using PoCA).

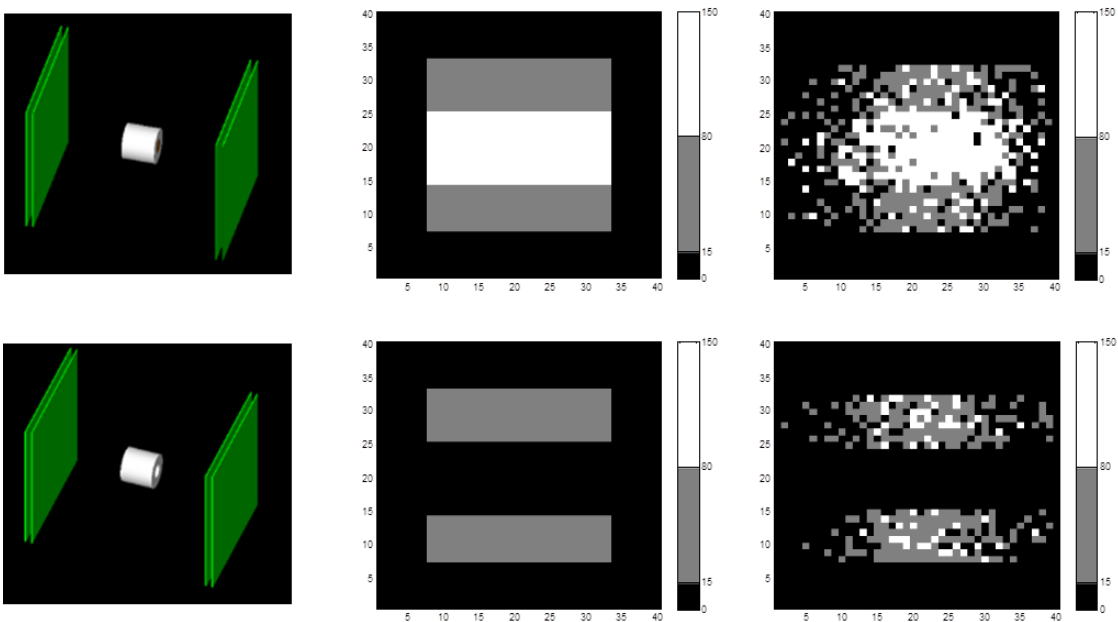


Figure 5-7. Horizontal slices of a simplified horizontal dry cask (left: GEANT4 model, center: images using a perfect algorithm, right: obtained images using PoCA).

#### d. Dry cask imaging

The PoCA algorithm was used for the reconstruction of actual, real size, vertical and horizontal dry casks loaded with different amount of spent nuclear fuel. Three detector sizes (small, medium, large) were used to investigate the effect of detector size on image resolution. Additional simulations and image reconstructions were performed with increasing number of muons. Detector size and number of muons eventually determine the measurement time needed to provide meaningful information about the cask content. For example, large detectors would be preferable since reduced time would be required to obtain the necessary number of muons. On the other hand, large detectors would be more expensive and more difficult to transport on site. For all plots shown, Y-axis is oriented vertically, X-axis is oriented parallel to the detector planes and Z-axis is vertical to the detector planes. Figure 5-8 shows the simulated scenarios. The scenarios include dry casks (a) fully loaded with 24 PWR fuel assemblies, (b) half loaded, (c) one row of fuel assemblies missing, (d) one fuel assembly missing and, (e) empty. To determine the sensitivity of the technique for imaging spent nuclear fuel dry casks simulations performed for  $10^5$ ,  $5 \cdot 10^5$  and  $10^6$  muons and included three detector sizes with active areas  $1.2 \times 1.2 \text{ m}^2$  (small)  $2.4 \times 2.4 \text{ m}^2$  (medium) and  $3.6 \times 3.6 \text{ m}^2$  (large).

The amount of muons passing through the detector planes depends on the size, orientation and detector solid angle. The angular distribution can be approximated by [34]:

$$\frac{dN}{d\Omega} = \frac{3}{\pi} \cos^2 \theta \left( \frac{\text{muons}}{\text{min sr cm}^2} \right) \quad (5-8)$$

where  $\theta$  is the zenith angle. The detector solid angle is:

$$\Omega = \frac{\vec{A} \cdot \vec{n}}{d^2} = \frac{hw \sin \varphi}{d^2} \text{ (sr)} \quad (5-9)$$

where h and w represent the dimensions (width, height) of the detector planes and, d is the distance from the dry cask centerline to the first detector plane (Figure 5-9). The number of muons passing through a detector is:

$$N = \frac{dN}{d\Omega} \Omega (\vec{A} \cdot \vec{n}) = \frac{dN}{d\Omega} \Omega hw \sin \varphi \left( \frac{\text{muons}}{\text{min}} \right) \quad (5-10)$$

The number of muons passing through a detector as a function of the detector size and zenith angle is shown in Table 5-1. For example, horizontal detectors located at zenith angle  $89^\circ$ , vertically oriented with  $\varphi=90^\circ$  and with dimensions  $h=w=3.6$  m and  $d=2.5$  m would require approximately 1 and 10 days to gather  $10^5$  and  $10^6$  muon measurements, respectively. A detector located at smaller zenith angles would require less time to gather the same amount of measurements. This result does not take into account other factors that would increase measurement time, for example background radiation field and detector noise.

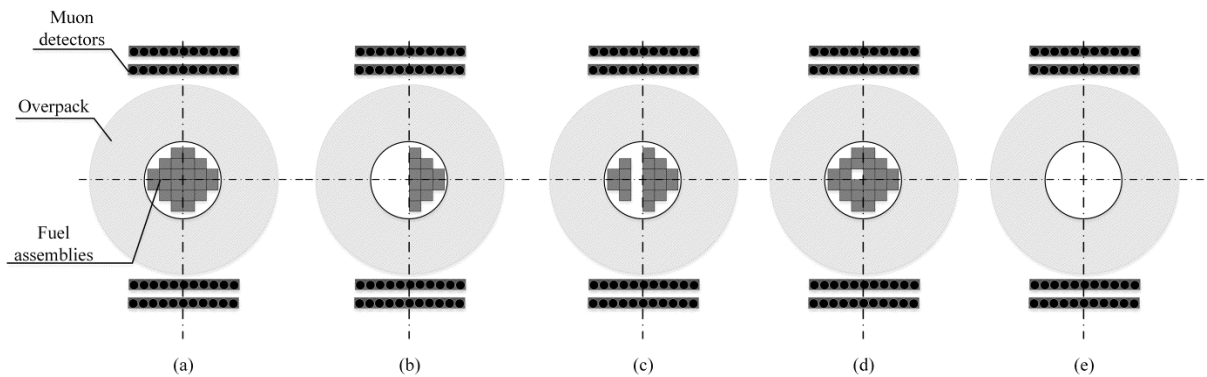


Figure 5-8. Simulated dry cask scenarios; (a) fully loaded, (b) half loaded, (c) row of fuel assemblies missing, (d) one fuel assembly missing and, (e) empty.

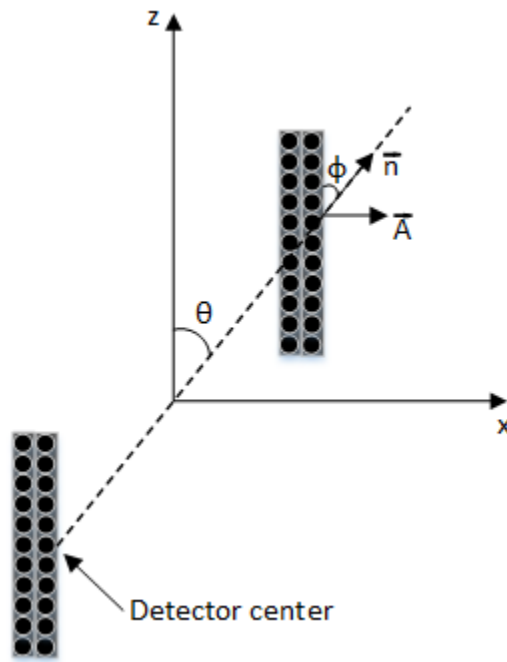


Figure 5-9. Detector geometry, zenith angle and detector plane vectors.

Table 5-1. Muons per minute measured for different detector geometries and zenith angles.

Height h (m)	Width w (m)	Distance d (m)	zenith angle $\theta$ ( $^{\circ}$ )	detector angle $\phi$ ( $^{\circ}$ )	muons/min
1.2	1.2	1.5	0	90	8800.63
			45	45	2200.15
			89	90	2.68
2.4	2.4	1.5	0	90	140810.10
			45	45	35202.52
			89	90	42.88
3.6	3.6	1.5	0	90	712851.17
			45	45	178212.79
			89	90	217.12

Reconstruction images for vertical and horizontal fully loaded dry casks using  $10^5$ ,  $5 \cdot 10^5$  and  $10^6$  muons are shown in in the upper and lower row of Figure 5-10, respectively. The reconstructions were performed for a large detector ( $3.6 \times 3.6 \text{ m}^2$ ) with muons having

energies 1-60 GeV, grid dimension 40x40x40 cm<sup>3</sup> and voxel size 20 cm. Each voxel therefore represent approximately the size of a half fuel assembly. Figure 5-10 shows 2-D vertical slices taken at the x-y plane through the center of the cask. The color scale represents the magnitude of the scattering angles. It is observed that even with muons as low as 10<sup>5</sup> the shape of the cask, the concrete walls that appear with light blue color and the location of spent nuclear fuel that appears with red color can be identified fairly accurately. Increasing the number of muons, the resolution improves considerably and the location and shape of different materials is shown correctly. Although the location of fuel assemblies at the center of the cask is correctly identified, the air gap that exists between the concrete walls and the fuel assemblies is not correctly captured. This is independent of the number of muons. For horizontal dry casks the resolution appears to be somewhat improved and allows identification of the air gap between concrete and fuel assemblies. This can be attributed to the PoCA algorithm which assigns scattering points in between multilayered materials. When multiple layers of materials are stacked vertically to the muon trajectory, the algorithm assigns scattering points between the layers and points are placed in areas where there are no fuel assemblies.

In Figure 5-11, reconstructed images are shown for empty vertical and horizontal dry casks. The cask shape is reconstructed correctly and concrete walls can be identified in all cases. Comparison between Figures 5-10 and 5-11, demonstrates that a fully loaded dry cask can be differentiated against an empty one using as low as 10<sup>5</sup> muons. However, as it will be shown below, this number of muons results in resolution that is too low to allow identification of more complex cases. The fully loaded and empty dry casks can be used as a baseline to compare against other scenarios. An alternative to improve

resolution would be to use smaller voxel size. For a grid with 64000 voxels of size 20 cm each,  $10^6$  muons would result in ~30 muons per voxel. Reducing the voxel size would result in less muons per voxel and to improve statistics a considerably larger number of muons would be needed.

Reconstructions of vertical fully loaded, half loaded and empty dry casks generated using  $10^6$  muons and different detector sizes are shown in Figure 5-12. Different detector sizes cover different areas of the dry cask. A small sized detector would cover only part of the fuel. The reconstructions using small size detectors are shown in the upper row of Figure 5-12. Reconstructed images using medium and large sized detectors are shown in the middle and lower row of Figure 5-12, respectively. Medium and larger sized detectors cover the fuel assemblies and the overpack area which facilitates the image interpretation. The algorithm can reproduce the cylindrical shape and allow differentiation between the concrete walls and the fuel. For the empty dry cask, the center is filled with air which the algorithm incorrectly interprets as concrete. Reconstructed images of horizontal fully loaded, half loaded and empty dry casks are shown in Figure 5-13. The PoCA limitation, described previously for vertically oriented dry casks, is reduced for horizontal dry casks. In this case, both fully loaded and empty dry casks are correctly reconstructed and better resolution is observed for horizontal dry casks than vertical ones. The reconstructed images allow correct identification of the dry cask loading and separation between concrete and fuel assemblies.

Image reconstructions were quantized to investigate the possibility of material classification. The accumulated scattering angles were classified into three categories: low (black color), medium (grey color) and high density (white color) materials.

Scattering of  $20 \text{ mrad}^2/\text{cm}$  or greater is classified as high density material, medium density is shown by scattering in the range  $10\text{-}20 \text{ mrad}^2/\text{cm}$  and low density material by scattering of  $10 \text{ mrad}^2/\text{cm}$ . The results are shown in Figure 5-14 for vertical fully loaded, half loaded and empty dry casks and Figure 5-15 for horizontal fully loaded, half loaded and empty dry casks. The reconstructed images are compared against the reconstructed images that would result from an ideal algorithm with perfect resolution. The processed reconstructed images facilitate differentiation between materials and identification of concrete and fuel assembly location. Air (black color) and concrete (grey color) can be easily separated over fuel assemblies (white color). The algorithm correctly identifies the amount of loading for each of the three cases (fully loaded, half loaded and empty) but misidentifies air as concrete in the case of an empty cask. This limitation is reduced for horizontal geometries where the empty dry cask is correctly classified as having no fuel within.

It was shown that reconstructions using the PoCA algorithm allow fairly accurate differentiation among fully loaded, half loaded and empty dry casks with minimal processing and making use of only one 2-D slice of the 3-D object volume. More information would be needed to allow adequate identification in more complex scenarios where smaller fuel quantities are not present. To assess such scenarios, simulations were performed for dry casks where one row of fuel assemblies was missing. Results are shown in Figures 5-16 and 5-17. Although one 2-D slice can provide information related to missing fuel assemblies, it is not enough to obtain exact location and number of assemblies missing. Using x-y and x-z slices, the missing row of fuel assemblies can be identified with acceptable accuracy. It is noted that this can be achieved only when

enough muons have been collected, in this case more than  $10^6$ . The reconstructed images were processed using heuristics to improve visibility and facilitate differentiation of the important dry cask features. Figure 5-18 shows the aesthetically enhanced images for horizontal and vertical dry casks. The different scenarios can be identified with the exception of the case where one fuel assembly is missing. For vertical dry casks it is not possible to locate the position of the missing fuel assembly. For horizontal dry cask, an indication exists that a fuel assembly is not present, but resolution is not enough to identify exact location. This can be attributed to the single scattering event assumption inherent within the PoCA algorithm. Resolution could be significantly improved with the application of more sophisticated imaging algorithms and via a combination of multiple Coulomb scattering and muon attenuation.



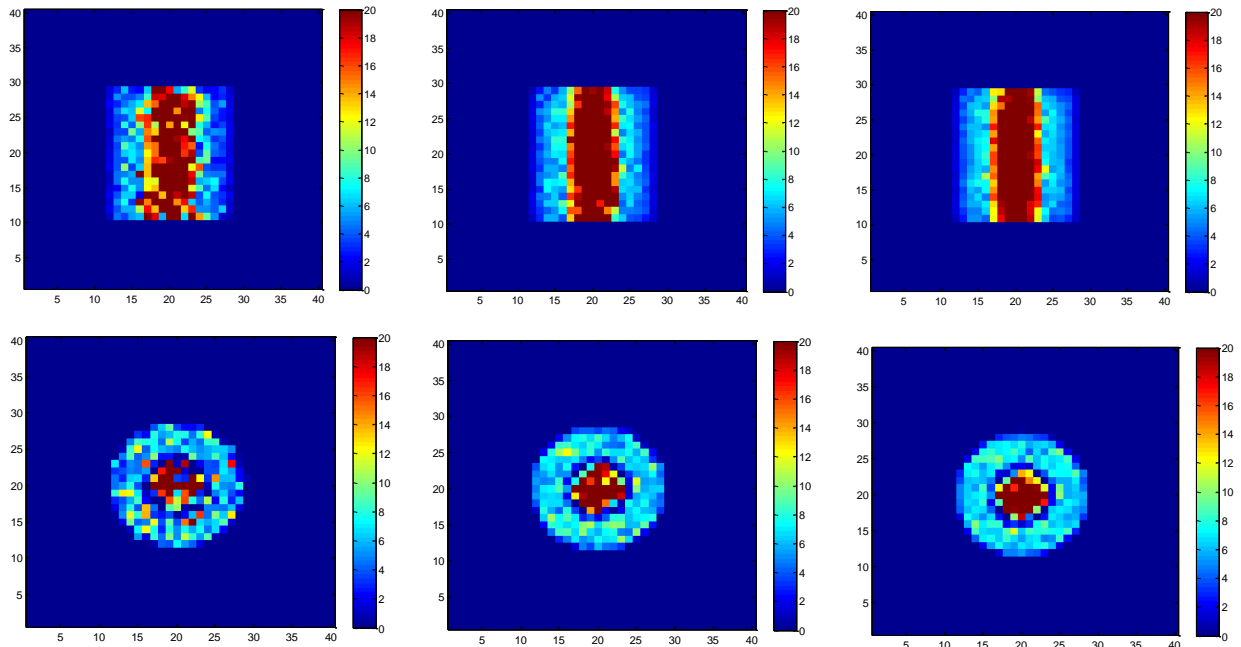


Figure 5-10. Vertical slices of dry casks with different number of muons (upper row: vertical fully loaded dry cask, lower row: horizontal fully loaded dry cask, left column:  $10^5$  muons, center column:  $5 \cdot 10^5$  muons, right column:  $10^6$  muons).

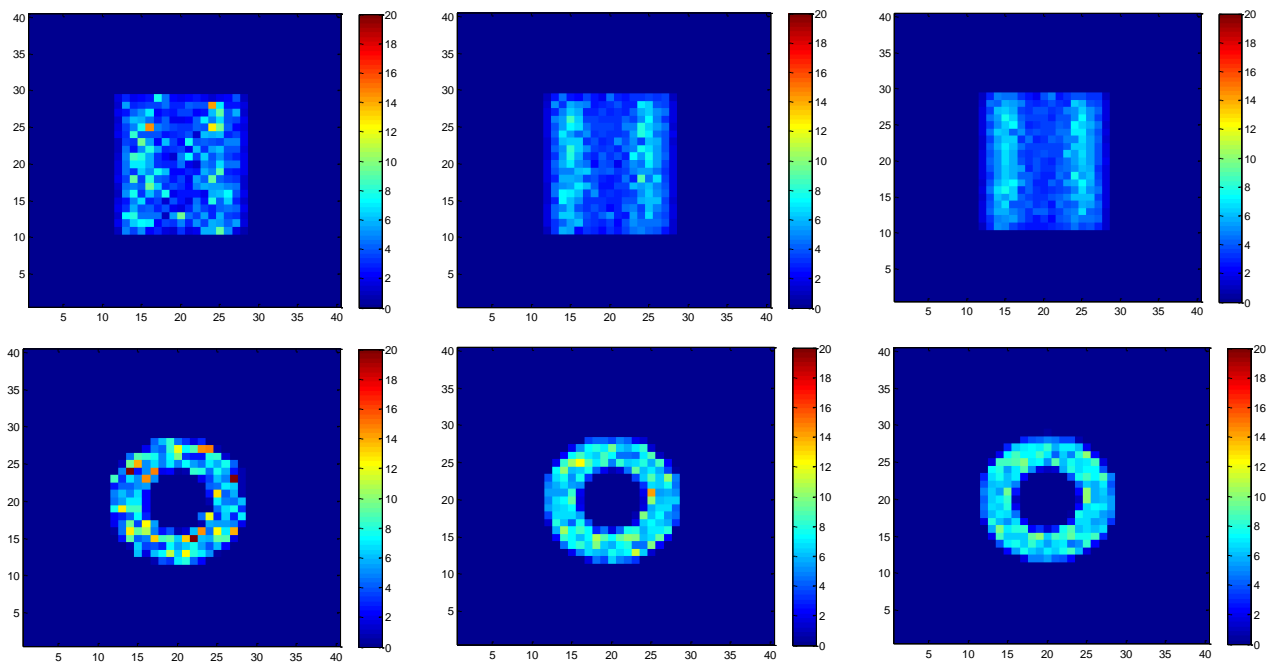


Figure 5-11. Imaging results of vertical dry casks with different number of muons (upper row: vertical empty dry cask, lower row: horizontal empty dry cask, left column:  $10^5$  muons, center column:  $5 \cdot 10^5$  muons, right column:  $10^6$  muons).

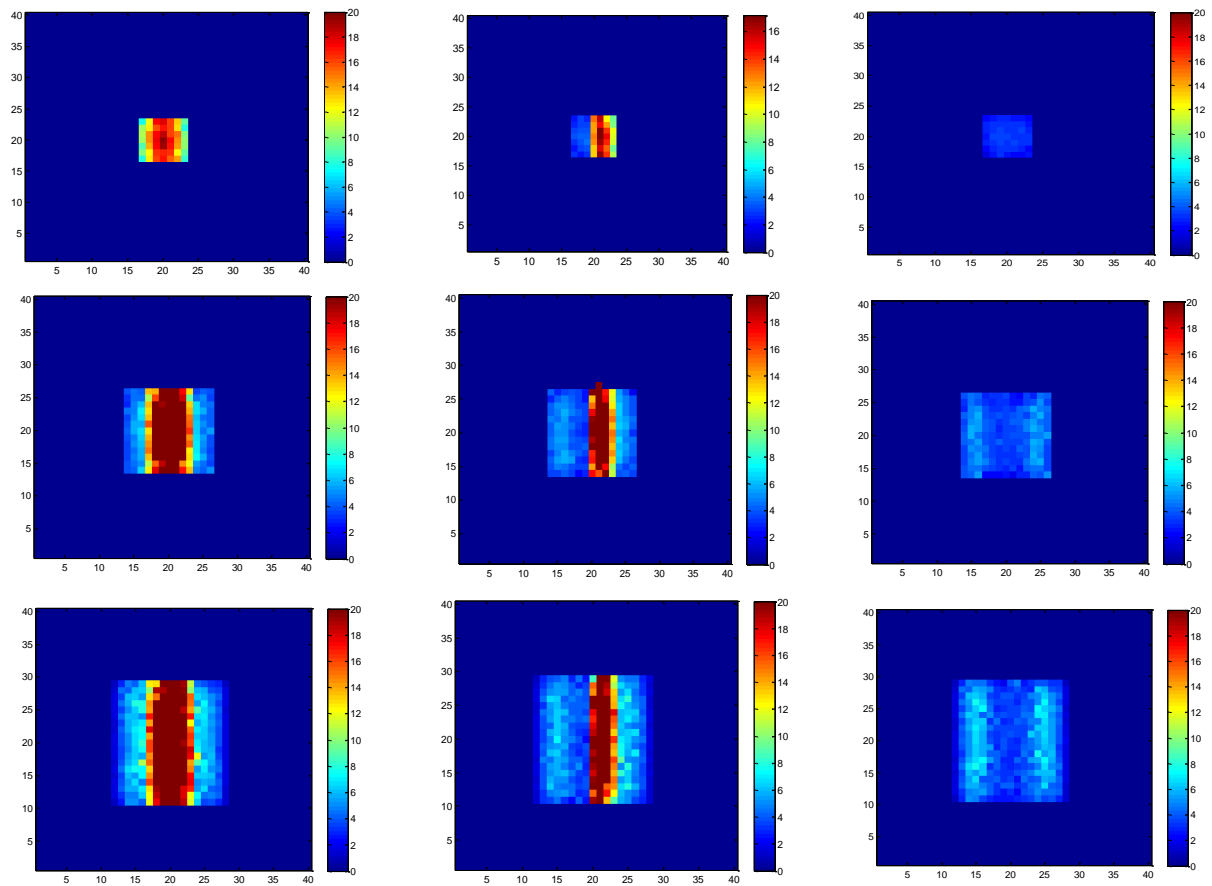


Figure 5-12. Imaging results of vertical dry casks with different muon detector sizes (upper row: small size detector, middle row: medium size detector, lower row: large size detector, left column: fully loaded, center column: half loaded, right column: empty).

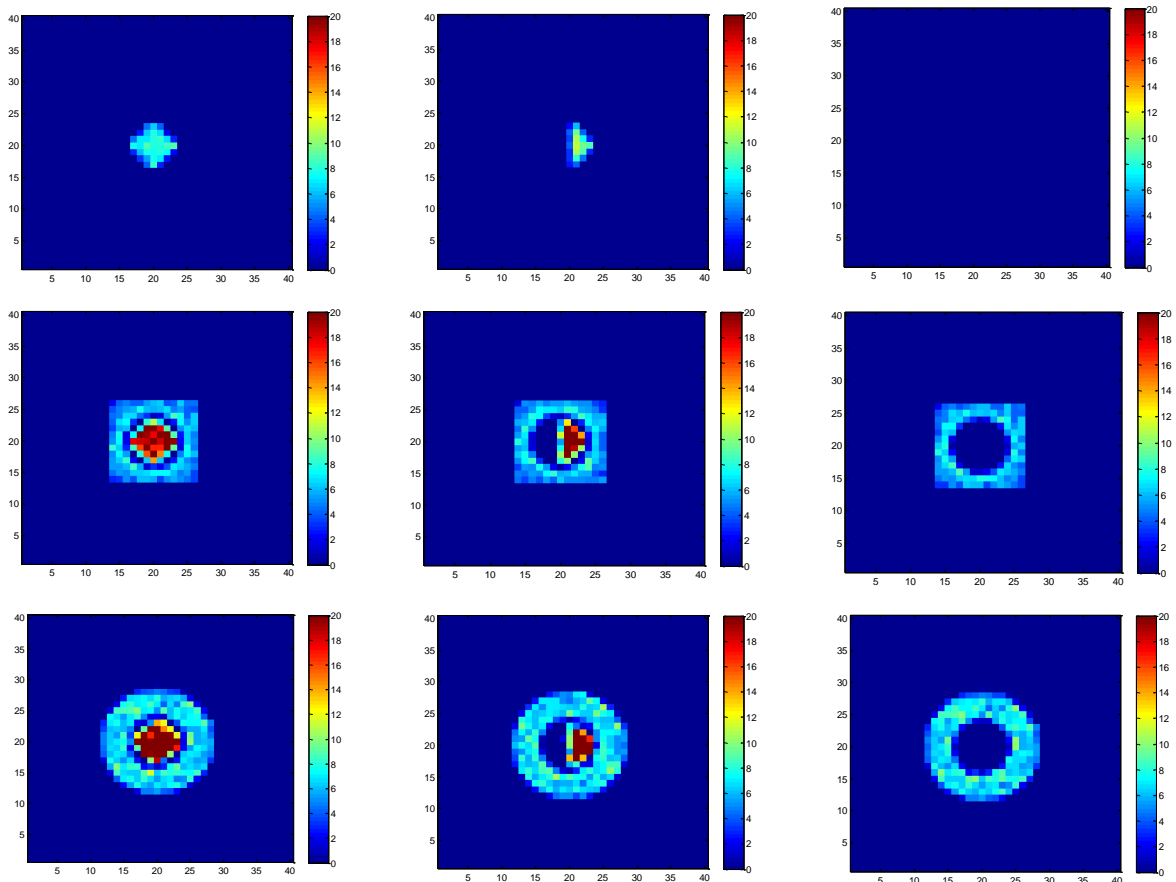


Figure 5-13. Imaging results of horizontal dry casks with different muon detector sizes (upper row: small size detector, middle row: medium size detector, lower row: large size detector, left column: fully loaded, center column: half loaded, right column: empty).

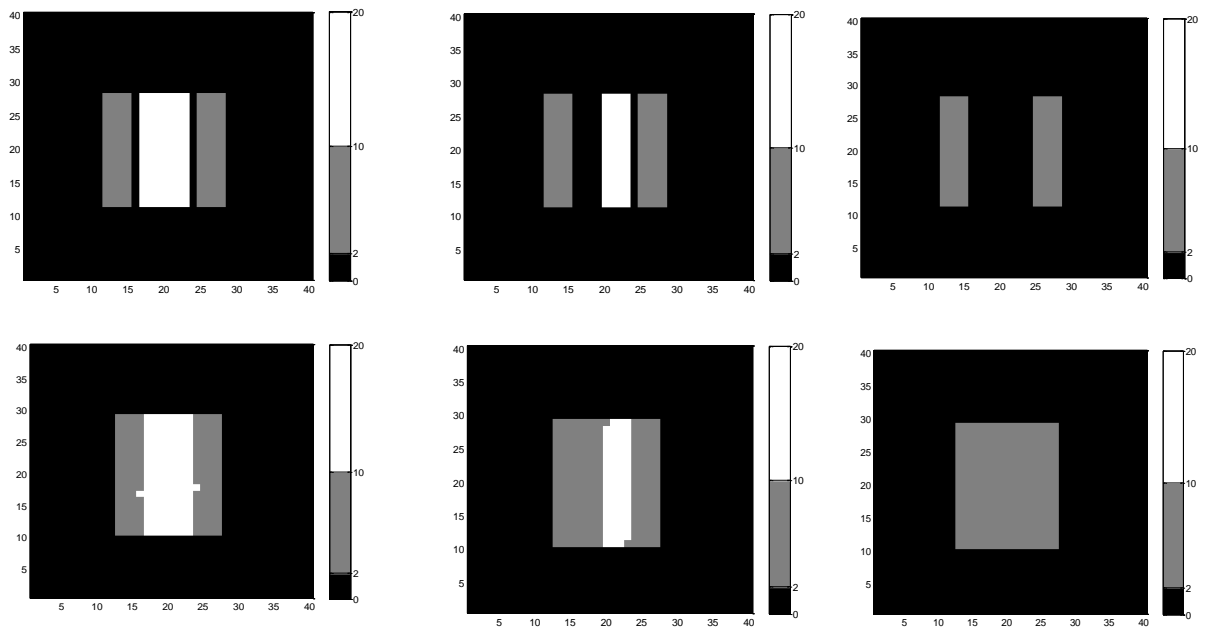


Figure 5-14. Imaging results of a vertical dry cask (upper row: images using a perfect algorithm, lower row: images using PoCA, left column: fully loaded, center column: half loaded, right column: empty).

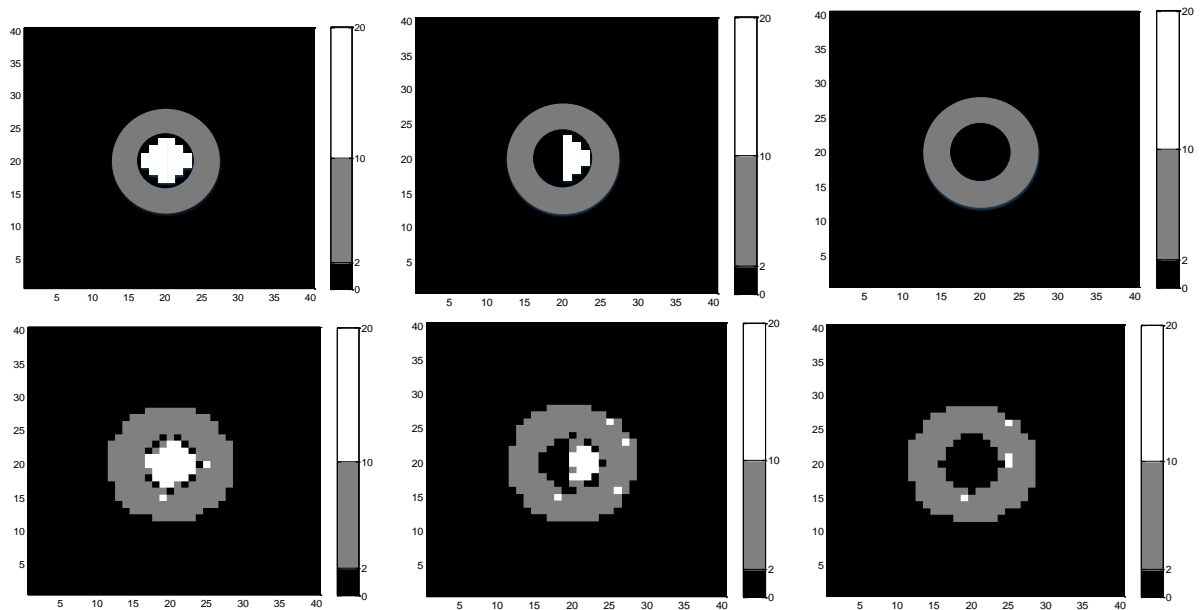


Figure 5-15. Imaging results of a horizontal dry cask (upper row: images using a perfect algorithm, lower row: images using PoCA, left column: fully loaded, center column: half loaded, right column: empty).

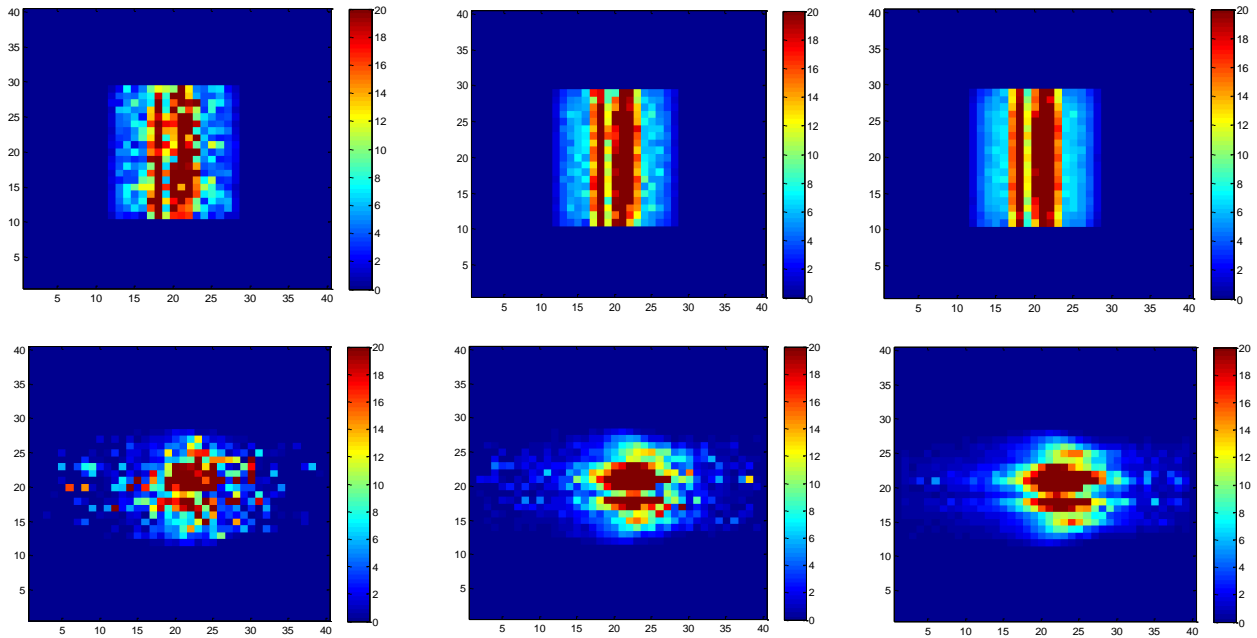


Figure 5-16. Imaging results of vertical dry casks with one row of fuel assemblies missing (upper row: vertical slice, lower row: horizontal slice, left column:  $10^5$  muons, center column:  $10^6$  muons, right column:  $10^7$  muons).

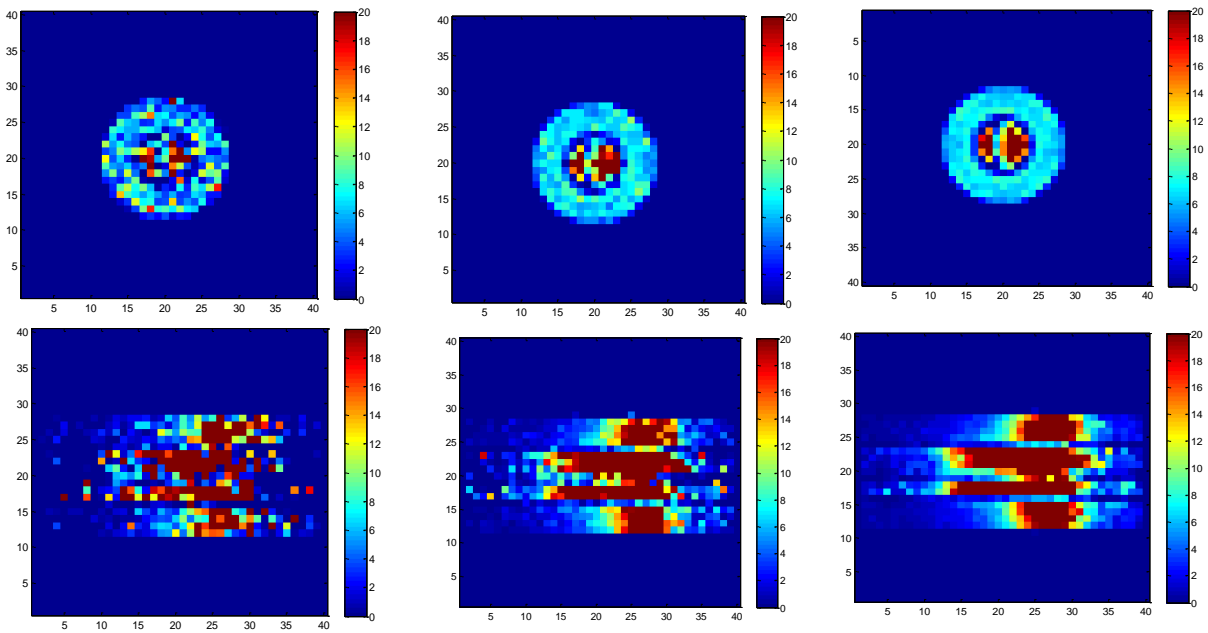


Figure 5-17. Imaging results of horizontal dry casks with one row of fuel assemblies missing (upper row: vertical slice, lower row: horizontal slice, left column:  $10^5$  muons, center column:  $10^6$  muons, right column:  $10^7$  muons).

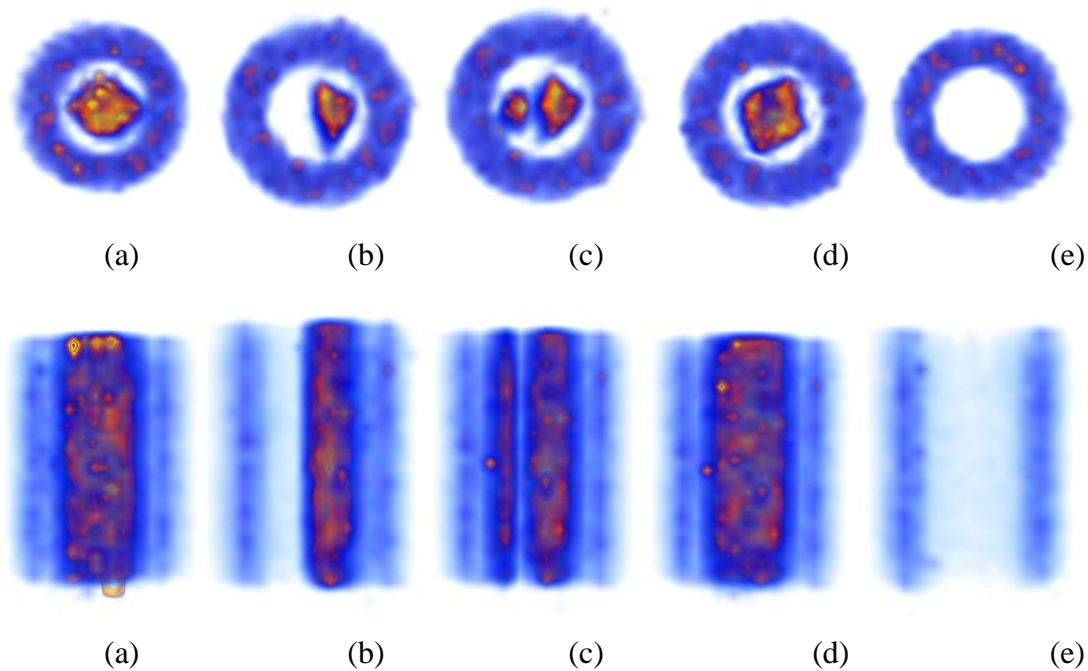


Figure 5-18. Imaging results of horizontal (upper row) and vertical (lower row) dry casks processed for aesthetically improved using heuristics (a: fully loaded, b: half loaded, c: one row is missing, d: one fuel assembly is missing, e: empty).

#### e. Reconstruction using muon transmission

Muons tend to lose on average 2 GeV when passing through a fully loaded dry cask. As a result, a portion of muons entering a dry cask will range out and be detected on the opposite detector. Measuring therefore the number of muons entering and the number of muons exiting a dry cask, we can produce 2-D flux maps showing density variations. However, due to multiple Coulomb scattering muons exiting a dry cask do not follow the same trajectory as the incoming muons. To produce a 2-D flux map, the scattering angles of incoming and outgoing muons were calculated and only muons having scattering angles between  $-10 \leq \theta \leq 10$  mrad were considered. These muons have been scattered only slightly and can be used as a parallel beam to produce a 2-D map similar to x-ray

radiography. Muons passing through less dense materials, i.e., concrete, will have higher counts than muons passing through fuel assemblies.  $10^5$ ,  $5 \cdot 10^5$ , and  $10^6$  muons were simulated and the 2-D maps were produced for a  $3.6 \times 3.6 \text{ m}^2$  detector and the following vertical and horizontal dry cask scenarios; (a) fully loaded, (b) half loaded, (c) row of fuel assemblies missing, (d) one fuel assembly missing and, (e) empty. The results for horizontal and vertical dry casks are shown in Figure 5-19 and 5-20, respectively. Transmission radiography can produce images of acceptable resolution for all scenarios. In the horizontal dry cask case, the all scenarios can be identified immediately and separated adequately. Increasing the number of muons measured, the image resolution improves considerably and for  $10^6$  muons the location of a missing fuel assembly can be identified. In the vertical dry cask case, similar conclusions can be drawn with the exception of the missing fuel assembly. Due to shadowing from other fuel assemblies, the location of a missing fuel assembly cannot be identified in the 2-D transmission map. In figure 5-21, a comparison between horizontal and vertical dry casks for  $10^6$  muons is shown. The difference in the case of a missing fuel assembly is apparent, with the vertical dry cask to appear incorrectly as fully loaded.

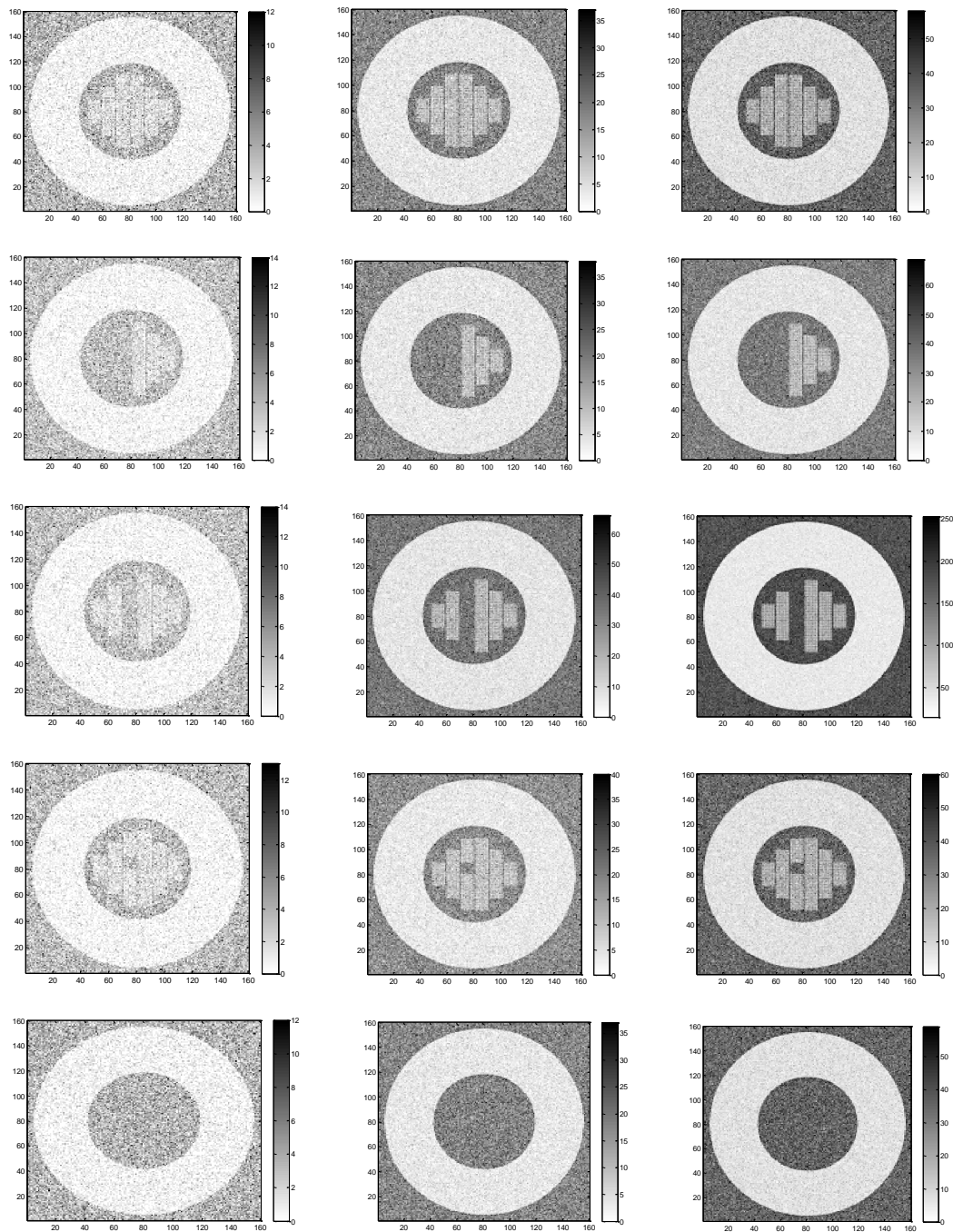


Figure 5-19. Imaging results of horizontal dry casks using muon transmission (from top to bottom: fully loaded, half loaded, row of fuel assemblies missing, one fuel assembly missing and, empty. Left column:  $10^5$  muons, center column:  $5 \cdot 10^5$  muons, right column:  $10^6$  muons).



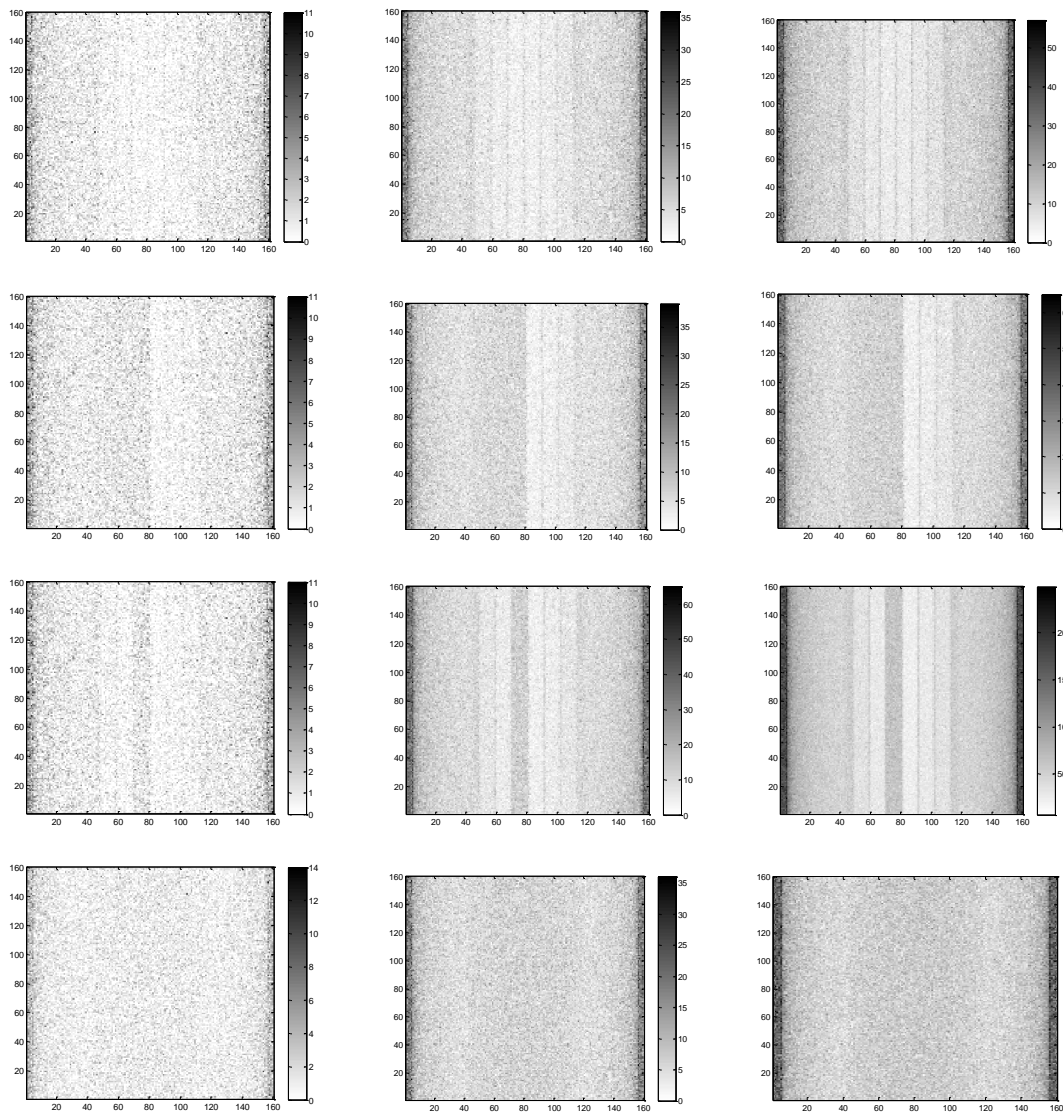


Figure 5-20. Imaging results of vertical dry casks using muon transmission (from top to bottom: fully loaded, half loaded, row of fuel assemblies missing, missing and, empty. Left column:  $10^5$  muons, center column:  $5 \cdot 10^5$  muons, right column:  $10^6$  muons).

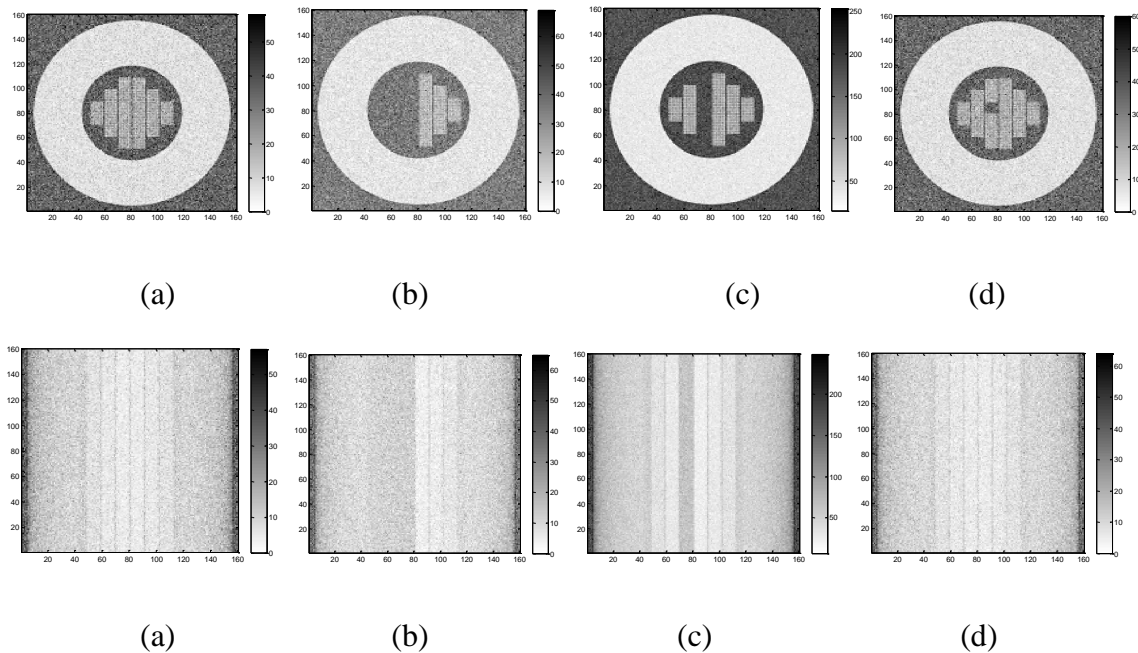


Figure 5-21. Comparison of horizontal (upper row) and vertical (lower row) dry casks using muon transmission. (a) fully loaded, (b) half loaded, (c) row of fuel assemblies missing, (d) one fuel assembly missing).

#### f. Summary

The applicability of muon scattering and transmission for imaging of spent nuclear fuel dry casks is investigated in this Chapter. Monte Carlo simulations of dry casks with different spent nuclear fuel loading are performed to simulate the passage of polyenergetic muons having energies in the range of 1-60 GeV through matter.

Calculations of muon scattering were performed for various scenarios, including vertical and horizontal fully loaded dry casks, half loaded dry casks, dry casks with one row of fuel assemblies missing, dry casks with one fuel assembly missing and empty dry casks. The PoCA algorithm was used for the reconstruction of vertical and horizontal dry casks with different amount of spent nuclear fuel loading. A “Muon Generator” was coupled with the Monte Carlo code GEANT4 and muon interactions through a commercial dry

cask loaded with PWR fuel assemblies were simulated. Cladding, Pu and fission products were neglected. Different detector sizes ( $1.2 \times 1.2 \text{ m}^2$ ,  $2.4 \times 2.4 \text{ m}^2$  and  $3.6 \times 3.6 \text{ m}^2$ ) and number of muons ( $10^5$ ,  $5 \cdot 10^5$ , and  $10^6$ ) were used to assess the effect on image resolution. It was shown that reconstructions using the PoCA algorithm allow fairly accurate differentiation among fully loaded, half loaded and empty dry casks with minimal processing and making use of only one 2-D slice of the 3-D object volume. A fully loaded dry cask can be correctly identified and differentiated against an empty one with muons as low as  $10^5$ . Improved resolution was obtained for horizontal dry casks and for larger number of muons which even allowed identification of the air gap between fuel assemblies and dry cask walls. A missing row of fuel assemblies was identified adequately using two 2-D slices and when enough muons have been collected, in this case more than  $10^6$ . Multiple Coulomb scattering allows identification of all scenarios with the exception of the case where one fuel assembly is missing. In this case only an indication exists that a fuel assembly is not present, however resolution was not enough to identify exact location. 2-D images were produced using muon transmission and it was shown that for horizontal dry cask case, all scenarios can be identified immediately and separated adequately. Increasing the number of muons measured, the resolution improves considerably and for  $10^7$  muons the location of a missing fuel assembly can be identified. Similarly, in the vertical dry cask case, all cases were correctly identified with the exception of a missing fuel assembly.

## CHAPTER 6. CONCLUSION

### a. Summary

The reliable and safe management of spent nuclear fuel is among the critical tasks to be addressed for the advancement of fission-based nuclear energy. There is a steady increase in the volume of spent nuclear fuel stored on-site (at reactor) as currently there is no permanent disposal option. No alternative disposal path is currently available and storage of spent nuclear fuel in dry cask storage containers is anticipated for the near future. In this dissertation a capability to monitor spent nuclear fuel stored within dry casks using cosmic ray muons is developed. The motivation stems from the need to investigate whether the stored content agrees with facility declarations to allow proliferation detection and international treaty verification. Cosmic ray muon imaging is a potential next generation technology in non-destructive evaluation and it was shown that muons can play a central role in monitoring nuclear waste and spent nuclear fuel stored in dense well shielded containers.

Chapter 2 presented background information on spent nuclear fuel, its storage and main characteristics of commercial dry casks. Cosmic ray muons and their properties were outlined and what has been attempted in this area using muons was discussed. In Chapter 3, it was established that the scattering variance follows Gamma distribution and the maximum likelihood estimator was shown to be minimum variance unbiased estimator. It is shown that the scattering distributions between a fully loaded dry cask and one with a fuel assembly missing initially overlap significantly but their distance eventually

increases with increasing number of muons. One missing fuel assembly can be distinguished from a fully loaded cask with a small overlapping between the distributions which is the case of 300,000 muons. The Bayesian monitoring framework was established in Chapter 4, a Bayesian monitoring algorithm was derived and its performance was evaluated. The results demonstrate that a dry cask that has relative difference more than 1.5% from a fully loaded which corresponds to one fuel assembly missing can be distinguished with zero error rate for as low as  $N=300,000$  muons. Relative difference of more than 3% can be correctly identified with even less muons, as low as 100,000. The imaging framework was presented in Chapter 5 and algorithms based on muon scattering and transmission were developed to reconstruct the contents of dry casks. Multiple Coulomb scattering allows identification of all scenarios with the exception of the case where one fuel assembly is missing. In this case only an indication exists that a fuel assembly is not present, however resolution was not enough to identify exact location. 2-D images that were produced using muon transmission showed that for horizontal dry cask case, all scenarios can be identified immediately and separated adequately.

#### b. Future work

Work on spent nuclear fuel monitoring continues with the objective to improve monitoring capabilities and image resolution. Monitoring can be improved through regularization. Neural networks could offer useful alternatives to existing methods. Measurement time could also be reduced incorporating momentum measurement and improving detector resolution. Images that can resolve fuel rod location could be useful

for investigation of fuel rod integrity following transportation or accidents. Imaging nuclear waste containers beyond dry casks could be helpful for content identification and legacy waste characterization. Applications of the Bayesian monitoring algorithm can be extended to homeland security, cargo scanning and treaty verification where a fast decision is a priority rather than a high quality image.

## LIST OF REFERENCES

## LIST OF REFERENCES

- [1] Olive, K.A. et al. (Particle Data Group), Chin. Phys. C, 38, 090001, 2014.
- [2] Cecchini, S., Spurio, M., “Atmospheric muons: experimental aspects”, Geoscientific Instrumentation, Methods and Data Systems, Volume 1, pp. 185–196, 2012.
- [3] George, E. P., “Cosmic rays measure overburden of tunnel”, Commonwealth Engineer, pp. 455-457, 1955.
- [4] Alvarez, L. et al., “Search for hidden chambers in the pyramids”, Science, Volume 167, pp. 832-839, 1970.
- [5] Borozdin, K. N. et al., “Radiographic imaging with cosmic ray muons”, Nature, Vol. 422, p. 277, 2003.
- [6] Gustafsson, J., “Tomography of canisters for spent nuclear fuel using cosmic ray muons”, Diploma thesis, UU-NF 05#08, Uppsala University, Sweden, 2005.
- [7] Schultz, L. J., “Cosmic ray muon radiography”, Thesis dissertation, Portland State University, 2003.
- [8] Perry, J. O., “Advanced applications of cosmic-ray muon radiography”, Thesis dissertation, The University of New Mexico, 2013.
- [9] IAEA, “Design measures to facilitate implementation of safeguards at future water cooled nuclear power plants”, Technical Report Series No. 392, International Atomic Energy Agency, Vienna, 1998.



- [10] Cox, L., “Cosmic ray muon scattering tomography for security applications”, National Nuclear Security Division, AWE, UK, 2010.
- [11] P. M. Jeneson, “Large vessel imaging using cosmic ray muons,” Nucl. Instr. Methods Phys. Res. A, vol. 525, 346-351, 2004.
- [12] Blue Ribbon Committee, “Blue Ribbon Commission on America’s Nuclear Future”, Report to the Secretary of Energy, 2012.
- [13] Alvarez, R., “Spent nuclear fuel pools in the US: Reducing the deadly risks of storage”, Institute for Policy Studies, 2011.
- [14] National Academy of Sciences, “Safety and Security of Commercial Spent Nuclear Fuel Storage”, Public report, 2005.
- [15] Kadak A. C., Yost, K., “Key issues associated with interim storage of used nuclear fuel”, Massachusetts Institute of Technology, MIT-NFC-TR-123, 2010.
- [16] Nuclear Waste Technical Review Board, “Evaluation of the Technical Basis for Extended Dry Storage and Transportation of Used Nuclear Fuel”, 2010.
- [17] Lamarsh, J. R., Baratta, A. J., “Introduction to Nuclear Engineering”, Prentice Hall, 3rd edition, 2001.
- [18] EPRI, “Industry Spent Fuel Handbook,” Techn. Rep. 1021048, 2010.
- [19] Allkofer, O. C., “Introduction to cosmic radiation”, K. Thiemig, 1975.
- [20] Grieder, P.K.F, “Cosmic rays at Earth”, Gulf Professional Publishing, 2001.
- [21] Nagamine, K., “Introductory muon science”, Cambridge University Press, 2003.
- [22] Abdel-Monem, M. S. E, “Cosmic ray muon spectrum and charge ration”, Thesis Dissertation, University of Houston, 1974.

- [23] Nandi, B. C., Sinha, M. S., “The momentum spectrum of muons at sea level in the range 5-1200 GeV/c”, J. Phys. A: Gen. Phys., vol. 5, pp. 1384-1394, 1972.
- [24] Tsuji, S. et al., “Measurements of muons at sea level”, J. Phys. G: Nucl. Part. Phys. 24, pp. 1805–1822, 1998.
- [25] Haino, S. et al., “Measurements of Primary and Atmospheric Cosmic-Ray Spectra with the BESS-TeV Spectrometer”, Physical Letters B594, pp. 35-46, 2004.
- [26] Jokisch, H. et al., “Cosmic-ray muon spectrum up to 1 TeV at 75° zenith angle”, Physical review D, vol. 19, pp. 1368-1372, 1979.
- [27] Baber, S. R. et al., “ The momentum spectrum of muons at sea-level in the range 3-1000 GeV/c”, Nuclear Physics B4, pp. 539-548, 1968.
- [28] Allkofer, O. C. et al., “The absolute cosmic ray muon spectrum at sea level”, Physics Letters, vol. 36B, pp. 425-427, 1971.
- [29] Allkofer, O. C. and Dau, W. D., “The muon charge ratio at sea level in the low momentum region”, Physics Letters, vol. 36B, pp. 439-440, 1972.
- [30] Ayre, C. A. et al., “Precise measurement of the vertical muon spectrum in the range 20-500 GeV/c”, J. Phys. G: Nucl. Phys., vol. 1, pp. 584-600, 1975.
- [31] Baxendale, J. M. et al., “Precise measurement of the sea level muon charge ratio”, J. Phys. G: Nucl. Phys., vol. 1, pp. 781-788, 1975.
- [32] Kellogg, R. G. and Kasha, H., “Momentum spectra, charge ratio, and zenith-angle dependence of cosmic-ray muons”, Physical review D, vol. 17, pp. 98-113, 1978.
- [33] Rastin, B. C., “An accurate measurement of the sea-level muon spectrum within the range 4 to 3000 GeV/c”, J. Phys. G: Nucl. Phys. 10, pp. 1609-1628, 1984.

- [34] Matsuno et al., “Cosmic-ray muon spectrum derived from the transferred energy spectrum of bursts observed by the Mutron calorimeter”, *Il nuove cimento*, vol. 73, pp. 209-234, 1983.
- [35] De Pascale, M. P. et al., “Absolute spectrum and charge ratio of cosmic ray muons in the energy region From 0.2 GeV to 100 GeV at 600 m above sea level”, *Journal of Geophysical Research*, vol. 98, pp. 3501-3507, 1993.
- [36] Kremer, J. et al., “Measurements of ground-level muons at two geomagnetic locations”, *Physical Review Letters*, vol. 83, pp. 4241-4244, 1999.
- [37] L3+C collaboration, “The atmospheric muon momentum spectrum”, *Nuclear Physics B*, 145, pp. 136-140, 2005.
- [38] J. A. Green et al., “Optimizing the Tracking Efficiency for Cosmic Ray Muon Tomography,” *IEEE Nucl. Sci. Symp. Conf. Rec.*, 1-6, 285-288, 2006.
- [39] R. C. Hoch, *Advances in cosmic ray muon tomography reconstruction algorithms*, M.S. thesis, Florida Institute of Technology, 2009.
- [40] L. Cox et al., “Detector requirement for a cosmic ray muon scattering tomography system,” *IEEE Nucl. Sci. Symp. Conf. Rec.*, 706-710, 2008.
- [41] H. Miyadera et al., “Imaging Fukushima Daiichi reactors with muons,” *AIP Adv.*, vol. 3, 052133, 2013.
- [42] L. J. Schultz et al., “Statistical reconstruction for cosmic ray muon tomography,” *IEEE Trans. Im. Proc.*, vol. 16 (8) 1985-1993, 2007.
- [43] Morris, C. L. et al., “Tomographic Imaging with Cosmic Ray Muons. *Science and Global Security*, Vol. 16, Issue 1-2, pp. 37-53, 2008.

- [44] S. Riggi et al., “Muon tomography imaging algorithms for nuclear threat detection inside large volume containers with the Muon Portal detector,” arXiv: 1307.0714v1, 2013.
- [45] K. Nagamine, “Geo-tomographic Observation of Inner-structure of Volcano with Cosmic-ray Muons,” *J. of Geogr.*, vol. 104(7) 998-1007, 1995.
- [46] C. J. Rhodes, “Muon tomography: looking inside dangerous places,” *Science Progress*, vol. 98(3) 2910299, 2015.
- [47] C. L. Morris et al., “Obtaining material identification with cosmic ray radiography,” *AIP Adv.*, vol. 2, 042128, 2012.
- [48] T. Sugita et al., “Cosmic-ray muon radiography of UO<sub>2</sub> fuel assembly,” *J. Nucl. Sci. and Technol.*, vol 51, 1024-1031, 2014.
- [49] C. L. Morris et al., “Analysis of muon radiography of the Toshiba nuclear critical assembly reactor,” *App. Phys. Lett.*, vol. 104, 024110, 2014.
- [50] C. Jewett et al., “Simulation of the use of cosmic rays to image nuclear waste and verify the contents of spent fuel containers,” in *Proc. of the Waste Management*, 2011.
- [51] G. E. Hogan, et al., “Detection of High-Z Objects using Multiple Scattering of Cosmic Ray Muons,” in *AIP Conf. Proc.*, vol. 698(1) 755-758, 2004.
- [52] L. J. Schultz et al., “Image reconstruction and material Z discrimination via cosmic ray muon radiography,” *Nucl. Instr. Methods Phys. Res. A*, vol. 519(3) 687, 2004.
- [53] S. Chatzidakis et al., “A Bayesian approach to monitoring spent fuel using cosmic ray muons,” *Trans. Am. Nucl. Soc.*, vol. 111, 369-370, 2014.
- [54] S. Chatzidakis et al., “Monte-Carlo simulations of cosmic ray muons for dry cask monitoring,” *Trans. Am. Nucl. Soc.*, vol. 112, 534-536, 2015.

- [55] S. Chatzidakis et al., “Interaction of Cosmic Ray Muons with Spent Nuclear Fuel Dry Casks and Determination of Lower Detection Limit,” Nucl. Instr. Methods Phys. Res. A, to be published.
- [56] Nastazi, M. et al., “Ion-solid interactions: Fundamentals and applications”, Cambridge University Press, 1996.
- [57] Bethe, H. A., “Moliere's Theory of Multiple Scattering”, Physical Review, Vol. 89, Issue 6, pp. 1256-1256, 1953.
- [58] Rossi, B., and Greisen, K., “Cosmic-ray theory”, Reviews of Modern Physics 13(4) 240, 1941.
- [59] Highland, V. L., “Some practical remarks on multiple scattering,” Nucl. Inst. Meth., 129, pp. 497-499, 1975.
- [60] Lynch, G. R. & Dahl, O. I., “Approximations to multiple Coulomb scattering”, Nuclear Instruments and Methods in Physics Research B, 58, pp. 6-10, 1991.
- [61] Tsai, Y.-S., “Pair production and bremsstrahlung of charged leptons:, Reviews of Modern Physics 46(4), 815, 1974.
- [62] S. Agostinelli et al., “GEANT4 – A simulation toolkit,” Nucl. Instr. Methods Phys. Res. A, vol. 506, 250–303, 2003.
- [63] Allison, J., et al., “Geant4 developments and applications”, IEEE Transactions on Nuclear Science, 53(1) pp. 270-278, 2006.
- [64] Bogdanov, A. G., et al. “Geant4 simulation of production and interaction of muons”, IEEE Transactions on Nuclear Science, 53(2) pp. 513-519, 2006.

- [65] S. Chatzidakis et al., “Developing a cosmic ray muon sampling capability for muon tomography and monitoring applications,” Nucl. Instr. Methods Phys. Res. A, vol. 804, 33-42, 2015.
- [66] Smith, J. A. and Duller, N. M., “Effects of pi meson decay-absorption phenomena on the high-energy mu meson zenithal variation near sea level”, Journal of Geophysical Research, vol. 64, pp. 2297-2305, 1959.
- [67] C. Hagmann, et al., “Cosmic-ray shower generator (CRY) for Monte Carlo transport codes”, Proceedings of the IEEE Nuclear Science Symposium Conference Record, vol. 2, pp. 1143–1146, 2007.
- [68] Bishop, C. M., “Pattern Recognition and Machine Learning”, Springer-Verlag, London, 2006.
- [69] Levy, B. C., “Principles of signal detection and parameter estimation”, Springer Science & Business Media, 2008.
- [70] Duda, R. O., Hart, P.E., & Stork, D.G., “Pattern classification”, John Wiley & Sons, 2012.
- [71] Fawcett, T., “An introduction to ROC analysis”, Pattern recognition letters, vol. 27(8), pp. 861-874, 2006.
- [72] Vapnik, V. N., and Vapnik, V., “Statistical learning theory”, Vol. 1. New York: Wiley, 1998.

## APPENDICES

### Appendix A: Calculation of radiation length for commercial dry casks

Radiation length is a characteristic amount of matter, usually measured in  $\text{g}/\text{cm}^2$  or  $\text{cm}$ , and represents the average distance required for an electron to lose  $1/e$  of its energy. In the present work, radiation length was calculated using [61]:

$$\frac{1}{X_0} = 4\alpha r_e^2 \frac{N_A}{A} \{Z^2 [L_{rad} - f(Z)] + Z L'_{rad}\} \quad (\text{A-1})$$

where  $Z$ ,  $A$ ,  $r_e$ ,  $N_A$  are the atomic number, atomic mass, Bohr radius and Avogadro number, respectively and:

$$L_{rad} = \ln(184.15Z^{-1/3}) \quad (\text{A-2})$$

$$L'_{rad} = \ln(1194Z^{-2/3}) \quad (\text{A-3})$$

for materials relevant to sealed containers. The function  $f(Z)$  is an infinite sum but for elements up to Uranium can be accurately represented by:

$$f(Z) = \alpha^2 [(1 + \alpha^2)^{-1} + 0.20206 - 0.0369\alpha^2 + 0.0083\alpha^4 - 0.002\alpha^6] \quad (\text{A-4})$$

For compounds, i.e.,  $\text{UO}_2$ , the radiation length can be determined using:

$$\frac{1}{X_0} = \sum_i \frac{w_i}{X_i} \quad (\text{A-5})$$

where  $w_i$  and  $X_i$  are the weight fraction and radiation length of the  $i$ -th element. For multiple layers of materials, as is the case of a spent nuclear fuel dry cask, the combined radiation length is calculated using:

$$\frac{d_0 \rho_0}{X_0} = \sum_j \frac{d_j \rho_j}{X_j} \quad (\text{A-6})$$

where  $d_j$ ,  $\rho_j$  and  $X_j$  are the thickness, density, and radiation length of the  $j$ th layer.

Radiation length follows a decreasing trend with increasing material density, and



therefore it is expected that the more dense the material the larger the scattering angle.

This indicates that a partially loaded container would result in a smaller than normal scattering angle than a fully loaded. Parameters used for radiation length calculation are shown in Table A-1.

Table A-1. Parameters used for radiation length calculation

	Z	A	$L_{\text{rad}}$	$L'_{\text{rad}}$	$f(Z)$
Oxygen	8	15.9994	4.522	5.698	0.004
Iron	26	55.845	4.129	4.913	0.042
Zirconium	40	91.224	3.986	4.625	0.095
Uranium	92	238.02891	3.708	4.070	0.395

Dry casks loaded with spent nuclear fuel are comprised of multiple layers of inhomogeneous materials. To compare the effect of different dry casks on the muon scattering variance, the radiation length number is defined:

$$R = \frac{X}{X_0} \quad (\text{A-7})$$

The radiation length number is the ratio of the overall path traversed by a muon,  $X$ , divided by the overall radiation length,  $X_0$ , of the dry cask. This dimensionless number suggests that dry casks with the same radiation length number would result in the same scattering variance for muons passing through them and having identical energies.

Radiation length numbers for six common dry cask designs have been calculated using equations (3-10) to (3-15). The first three belong to the class of casks having a concrete overpack, i.e., VSC-24, HI-STORM, NUHOMS, and the rest are casks with metallic body, i.e., CASTOR, TN, HI-STAR. The dry casks are considered to consist of the cask body and the spent nuclear fuel assemblies. Canister structure and inner basket have been neglected due to their small thickness. The characteristics used for a fully loaded dry cask

are shown in Tables A-2 to A-4. Two reference casks, one that corresponds to casks with concrete overpack and a second one corresponding to casks with metallic body, have been constructed in such a way that would provide similar radiation length number to the actual ones. It appears that dry casks have an overall ratio  $X/X_0$  ranging from 10 when empty up to 180 when fully loaded (Figure 3-5).

Table A-2. Fully loaded dry cask properties summary

	Overpack thickness (cm)	Overpack material	Overpack density $\rho_1$ (g/cm <sup>3</sup> )	Canister diameter (cm)	Fuel Material	Fuel density $\rho_2$ (g/cm <sup>3</sup> )
VSC-24	78	Concrete	2.3	154	UO <sub>2</sub>	10.3
HI-STORM	80	Concrete	2.3	171	UO <sub>2</sub>	10.3
NUHOMS	61	Concrete	2.3	171	UO <sub>2</sub>	10.3
CASTOR	38	SS	7.87	152.4	UO <sub>2</sub>	10.3
TN-32	31.7	SS	7.87	175	UO <sub>2</sub>	10.3
HI-STAR	34.5	SS	7.87	171	UO <sub>2</sub>	10.3
Ref. cask 1	70	Concrete	2.3	170	UO <sub>2</sub>	10.3
Ref. cask 2	40	SS	7.87	160	UO <sub>2</sub>	10.3

Table A-3. Properties of the dry cask layers

	$X_1$ (g/cm <sup>2</sup> )	$X_2$ (g/cm <sup>2</sup> )	$\rho_0$ (g/cm <sup>3</sup> )	$X_0$ (cm)	$X_0$ (g/cm <sup>2</sup> )	R (-)	Angle (mrad)
VSC-24	26.57	6.65	5.23	8.409	1.608	152.902	66.770
HI-STORM	26.57	6.65	5.18	8.450	1.631	153.248	66.850
NUHOMS	26.57	6.65	5.70	8.052	1.413	149.959	66.083
CASTOR	13.83	6.65	9.187	8.350	0.908	182.646	73.390
TN-32	13.83	6.65	9.295	8.126	0.874	175.476	71.844
HI-STAR	13.83	6.65	9.245	8.227	0.889	178.663	72.534
Ref. cask 1	26.57	6.65	5.18	8.450	1.631	153.248	66.850
Ref. cask 2	13.83	6.65	9.156	8.417	0.919	184.922	73.875

Table A-4. Radiation length number R and scattering angle for different dry casks

	$X_1$ (g/cm <sup>2</sup> )	$X_2$ (g/cm <sup>2</sup> )	$\rho_0$ (g/cm <sup>3</sup> )	$X_0$ (cm)	$X_0$ (g/cm <sup>2</sup> )	R (-)	Angle (mrad)
VSC-24	26.57	6.65	2.3	26.57	11.552	13.503	18.306
HI-STORM	26.57	6.65	2.3	26.57	11.552	13.850	18.556
NUHOMS	26.57	6.65	2.3	26.57	11.552	10.560	16.051
CASTOR	13.83	6.65	7.87	13.83	1.757	43.248	34.080
TN-32	13.83	6.65	7.87	13.83	1.757	36.077	30.939
HI-STAR	13.83	6.65	7.87	13.83	1.757	39.264	32.368
Ref. cask 1	26.57	6.65	2.3	26.57	11.552	13.850	18.556
Ref. cask 2	13.83	6.65	7.87	13.83	1.757	45.524	35.025

## Appendix B: A Geant4-MATLAB Muon Generator for Monte-Carlo Simulations

The GEANT4 Monte Carlo code [62] was used to perform muon simulations and estimate muon paths through spent nuclear fuel dry casks. GEANT4 is a Monte Carlo code developed for use by the High Energy Physics community. It is designed for tracking high energy subatomic particles and their interactions with matter. Its object-oriented philosophy, flexibility and functionality have enabled its use in other physics domains with applications ranging from medical physics to space science and engineering. GEANT4 is the successor of the GEANT3 developed in the early 1990s at CERN and KEK. Currently, GEANT4 is an open source code based on C++, freely available, developed and maintained by a large international collaboration known as the “GEANT4 collaboration group” with participating scientists, researchers and engineers from Europe, Japan, United States and Canada. In this collaboration, dedicated working groups are responsible for the continuous testing, quality assurance and documentation of the code. GEANT4 has been successfully used for detailed modeling of instruments and detectors in the framework of the Large Hadron Collider experiment, simulation of the BaBar experiment and the ATLAS experiment.

A variety of physics models are provided to simulate the interaction of particles with matter over a wide range of energies. A number of tools, such as storage of events and particle tracks as well as visualization of the particle trajectories, facilitate the detailed modeling for a variety of detectors, geometries and processes. The level of customization that can be put in the model can provide for extremely detailed simulations. Input parameters include: the geometry of the system, the materials involved, fundamental

particles of interest, generation of primary particles of events, tracking of particles through materials and external electromagnetic fields, the physics processes governing particle interactions, the response of sensitive detector components, the generation of event data, the storage of events and tracks, the visualization of the detector and particle trajectories, and the capture for subsequent analysis of simulation data at different levels of detail and refinement [62, 63].

GEANT4 physics processes cover diverse interactions over an extended energy range, from optical photons and thermal neutrons to the high energy collisions at the Large Hadron Collider (LHC) and in cosmic ray experiments. Particles tracked include leptons, photons, hadrons and ions [63]. Electromagnetic, weak and nuclear interactions are described by theoretical models from very low to high energies. Cross-sections and physical data are extracted from evaluated data libraries, ENDF/B-VI, EPDL97, EEDL and EADL. GEANT4 offers a large database of geometry options and readily available materials, elements and chemical compounds. However, the users have the option to create their own geometrical shapes and materials. As a result, GEANT4 is a recognized code by the High Energy Physics community, and its unique characteristics make the code ideal for use in the modeling of muon interaction with dry casks.

In GEANT4, a particle that flies through a detector is treated as a classical particle, i.e. not a wave function, but a point-like object which has a well-defined momentum at each instant. This is a reasonable approximation, given that in most practical situations particles are seen as “tracks” in macroscopic detectors. GEANT4 is based on a semi-classical approach, because the particles are treated classically, but their interactions - cross sections and final states - often take into account the results of quantum-mechanical

effects. The code simulates one particle at the time and then breaks down the life of the particle into steps. For each step, the step length is determined by the cross sections of the physics processes and the geometrical boundaries; if new particles are created, the code adds them to the list of particles to be transported; if the particle is destroyed by an interaction, or it reaches the end of the apparatus, or its energy is below a (tracking) threshold, then the simulation of this particle is over. Ionization accounts for the main energy loss in energies below 100GeV. For  $0.2 < E < 1 \text{ GeV}$  the Bethe-Bloch formula with shell and density corrections is implemented. For  $E > 1 \text{ GeV}$  radiative corrections are additionally applied to the Bethe-Bloch formula. The statistical nature of energy loss is represented by a Gaussian distribution for thick absorbers and by a Landau distribution for the case of thin absorbers. It appears that the accuracy of these implementations is on the order of a few percent [64].

GEANT4 does not provide a built in library with muon energy and angular distributions. To generate muons from the actual measured muon spectrum a cosmic ray muon sampling capability, a “Muon Generator”, was developed [65]. The “Muon Generator” is based on a phenomenological model that captures the main characteristics of the experimentally measured spectrum coupled with a set of statistical algorithms is developed. The muons generated can have zenith angles in the range  $0-90^\circ$  and energies in the range 1-100 GeV. The muon angular and energy distributions are reproduced using the “Muon Generator” and integrated into GEANT4. The “Muon Generator” offers a way to allow easy coupling with GEANT4 interface. It generates the necessary user-defined histograms for use with the GEANT4 *G4GeneralParticleSource* macro file. Using the “Muon Generator”, simulations of muon-dry cask interactions can be performed.

The Smith & Duller [66] phenomenological model describes the muon energy spectrum and provides an overall description of the pion and muon interactions as they propagate through the atmosphere. It includes zenith angle and energy dependencies:

$$N_{\mu}(E_{\pi}, \theta) = \frac{AE_{\pi}^{-\gamma} P_{\mu} \lambda_{\pi} b j_{\pi}}{E_{\pi} \cos \theta + b j_{\pi}} \quad (\text{B-1})$$

where  $N_{\mu}$  is the muon differential intensity and  $E_{\pi}$  is the pion energy that generated a muon with ground level energy  $E_{\mu}$ . The parameters  $A$  and  $\gamma$  were obtained from a fit to the experimental measurements of Nandi & Sinha [23] and the resulting parameters  $A$  and  $\gamma$  with 95% confidence intervals are shown in the following Table B-1.

Table B-1. Best fit parameters and confidence intervals [5]

Parameter	A (95% CI)	$\gamma$ (95% CI)
Value	0.002382 (0.002075, 0.002688)	2.645 (2.594, 2.697)

The phenomenological model using the above parameters was tested and evaluated against the experimental datasets of Jokisch et al., Tsuji et al., and Haino et al. which cover a large range of energies, from 0.5 GeV to 1100 GeV and a wide range of zenith angles ( $0^{\circ}$ ,  $30^{\circ}$ ,  $60^{\circ}$ ,  $75^{\circ}$ ) [6][7][8]. The present fitted phenomenological model was also compared to a recently developed parametric model proposed by Reyna [9]. The graphical representation of the present model and its behavior against various experimental measurements for different levels of energy and zenith angle is shown in Figure B-1. The phenomenological model appears to capture correctly the different features of the muon spectrum even in large zenith angles [10].

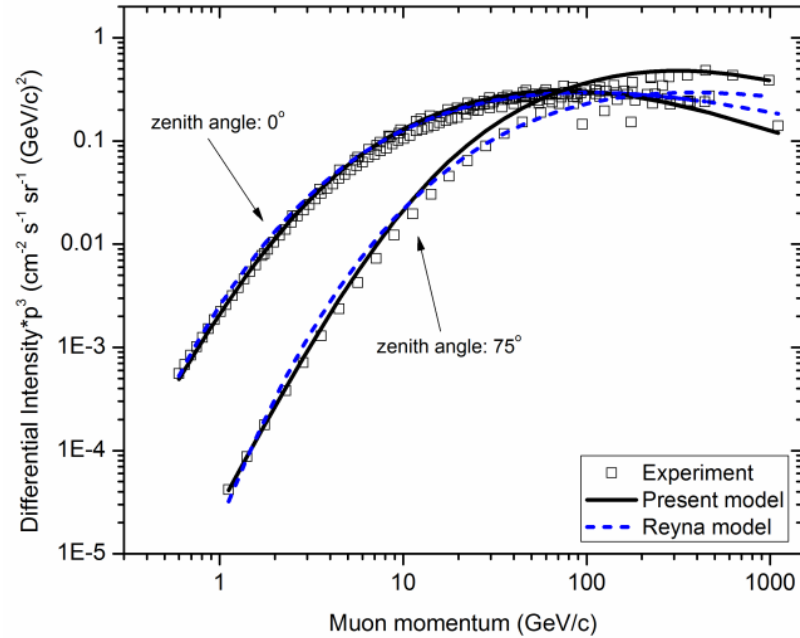


Figure B-1. Model vs. experimental measurements [10].

The inverse transform method is used to obtain random samples from the muon angular distribution and subsequently the Acceptance-Rejection (A-R) method is used to generate samples from the muon energy distribution described by the previously mentioned phenomenological model. The output is a vector containing the sampled muon angles and energies. 100,000 samples were randomly selected and the resulting distribution is compared against experimental measurements and estimates from the software library CRY [67]. This output when included in the GEANT4 macro file will generate primary particles with the desirable muon distribution. GEANT4 generated distributions are shown in Figure B-2 for 100,000 muons with energies 1-60 GeV and 0-90° zenith angle. Good agreement is observed with CRY.



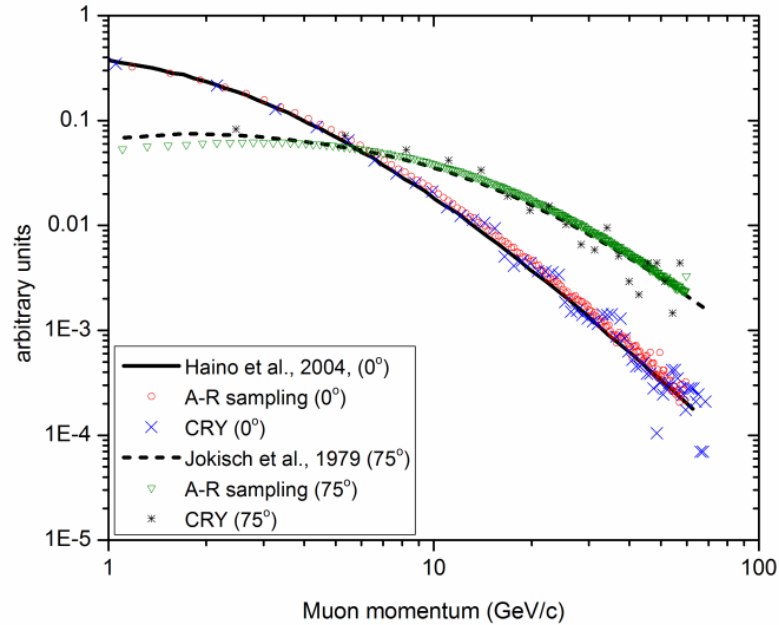


Figure B-2. Muon energy distribution using A-R [10].

For non-standard energy and angular distributions Geant4 requires the utilization of the General Particle Source module which via the *G4GeneralParticleSource* class allows specification of user defined angular and energy distributions. The user defined histograms are specified in macro files using the following commands [2]:

- |   |                                |
|---|--------------------------------|
| 1. <i>/gps/particle mu+</i>                           | (specify particle type)        |
| 2. <i>/gps/ang/type user</i>                          | (user defined histogram)       |
| 3. <i>/gps/hist/type theta</i>                        | (zenith angle histogram)       |
| 4. <i>/gps/hist/point B<sub>t</sub> W<sub>t</sub></i> | (angular histogram values)     |
| 5. <i>/gps/ene/type Arb</i>                           | (user defined histogram)       |
| 6. <i>/gps/hist/type arb</i>                          | (point-wise energy spectrum)   |
| 7. <i>/gps/hist/point E<sub>h</sub> H<sub>h</sub></i> | (energy spectrum values)       |
| 8. <i>/gps/hist/inter Lin</i>                         | (interpolation scheme: Linear) |
| 9. <i>/run/beamOn 1000</i>                            | (number of particles)          |

where a short explanation of each command appears in parentheses. The histograms represent differential functions and must be included one bin at a time. Angular histogram is described using the bin upper boundary and the area of the bin. Energy

spectrum (point-wise) is described using the bin center and the height of the bin. The first value of each histogram must be the lower boundary of the bin and a dummy value that is not used.

A MATLAB script has been developed to facilitate the generation of the energy and angular histograms using the “muon generator” output and the macro command for the Geant4 file. The script generates a look-up table that contains the sampled muon angles and energies as well as histograms for muon angular and energy distributions. The script output has the following formatting:

```
/gps/hist/point 1317.60000 0.0
/gps/hist/point 1317.60568 0.13389
/gps/hist/point 1952.65036 0.13287
.  
.  
.  
/gps/hist/point 5762.91847 0.079852
```

This output when included in the Geant4 macro file (in place of command 4 for angular distribution and command 7 for energy spectrum) will generate primary particles with the desirable muon distribution. Geant4 generated distributions are shown in Figures B-3 and B-4 for 100,000 muons with energies 1-60 GeV and 0-90° zenith angle. Good agreement is observed with CRY.

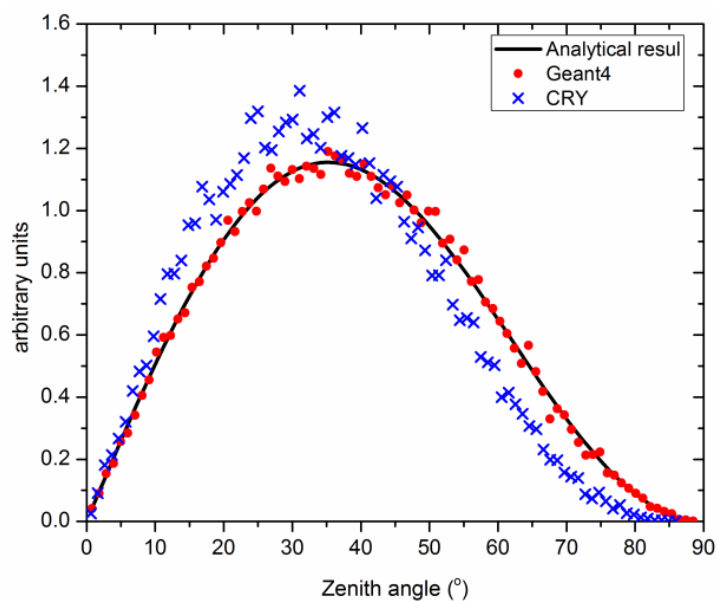


Figure B-3. Geant4 muon particles angular distribution

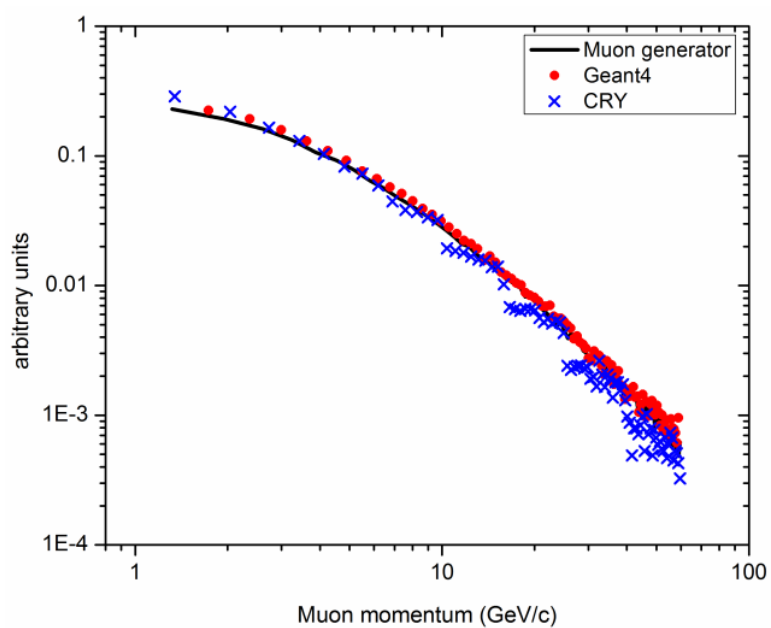


Figure B-4. Geant4 muon particles energy distribution

## Appendix C: Derivation of the scattering variance distribution

This measured variance of scattering angles is a function of random variables and therefore is a random variable itself. For every measurement of  $N$  scattering angles, an estimate of the scattering variance is calculated. To calculate the behavior of the scattering variance estimator and identify the number of muons that need to be simulated in order to get an acceptably accurate estimate, the Gamma distribution needs to be introduced:

$$Gamma(\alpha, \beta) = \frac{\beta^\alpha y^{\alpha-1}}{\Gamma(\alpha)} e^{-\beta y}, \alpha, \beta > 0, y \geq 0 \quad (C-1)$$

The expected value and variance of the Gamma distribution with parameters  $\alpha, \beta$  is given by:

$$\mathbb{E}[Y] = \frac{\alpha}{\beta} \quad (C-2)$$

$$Var[Y] = \frac{\alpha}{\beta^2} \quad (C-3)$$

Using moment generating functions, the square of a normal random variable follows Gamma distribution with parameters:

$$Y^2 \sim Gamma\left(\frac{1}{2}, \frac{1}{2\sigma^2}\right) \quad (C-4)$$

An estimator for the scattering variance based on the collected measured scattering angles can be obtained using maximum likelihood. Let  $D$  the measurement vector:

$$D = [y_1, y_2, \dots, y_N] \quad (C-5)$$

The likelihood function given the scattering variance is:

$$P(D|0, \sigma_{\Delta\theta}^2) = \prod_{i=1}^N \frac{1}{\sqrt{2\pi\sigma_{\Delta\theta}^2}} e^{-\frac{1}{2\sigma_{\Delta\theta}^2} \sum_{i=1}^N y_i^2} \quad (\text{C-6})$$

The estimator can be obtained by maximizing the log-likelihood function:

$$\hat{\sigma}_{\Delta\theta}^2 = \operatorname{argmax} \ln P(D|0, \sigma_{\Delta\theta}^2) \quad (\text{C-7})$$

The estimator is found to be:

$$\hat{\sigma}_{\Delta\theta}^2 = \frac{1}{N} \sum_{i=1}^N y_i^2 \quad (\text{C-8})$$

The estimator of the scattering variance is a function of the sum of squared random variables:

$$Z = \sum_{i=1}^N Y_i^2 \quad (\text{C-9})$$

The moment generating function for the Gamma distribution is:

$$M_Y(t) = \mathbb{E}[e^{tY}] = \left( \frac{\beta}{\beta - t} \right)^\alpha \quad (\text{C-10})$$

The distribution of the random variable  $Z$  can be derived using the moment generating function:

$$M_Z(t) = \mathbb{E}[e^{tZ}] = \mathbb{E}\left[e^{t \sum_{i=1}^N Y_i^2}\right] = \prod_{i=1}^N \mathbb{E}\left[e^{tY_i^2}\right] = (M_Y(t))^N = \left( \frac{\beta}{\beta - t} \right)^{N\alpha} \quad (\text{C-11})$$

Therefore, the random variable  $Z$  is distributed according to Gamma distribution with parameters:

$$Z = \sum_{i=1}^N Y_i^2 \sim \text{Gamma}\left(\frac{N}{2}, \frac{1}{2\sigma^2}\right) \quad (\text{C-12})$$

The expected value and variance of random variable  $Z$  are:

$$\mathbb{E}[Z] = N\sigma^2 \quad (\text{C-13})$$

$$\text{Var}[Z] = 2N\sigma^4 \quad (\text{C-14})$$

Setting a new random variable  $W$  dividing  $Z$  by  $N$ , the distribution is scaled:

$$W = \frac{Z}{N} \sim \text{Gamma}\left(\frac{N}{2}, \frac{N}{2\sigma^2}\right) \quad (\text{C-15})$$

The random variable  $W$  represents the scattering density with expected value and variance:

$$\mathbb{E}[W] = \sigma^2 \quad (\text{C-16})$$

$$\text{Var}[W] = \frac{2\sigma^4}{N} \quad (\text{C-17})$$

The scattering variance estimator can be shown to be unbiased:

$$\mathbb{E}[W] = \mathbb{E}\left[\frac{1}{N} \sum_{i=1}^N Y_i^2\right] = \frac{1}{N} \mathbb{E}\left[\sum_{i=1}^N Y_i^2\right] = \frac{N}{N} \mathbb{E}[Y_i^2] = \sigma^2 \quad (\text{C-18})$$

The mean square error is then equal the the variance:

$$\text{MSE} = \mathbb{E}[(W - \sigma^2)^2] = \text{Var}(W) - \text{bias} = \text{Var}(W) \quad (\text{C-19})$$

The Cramer-Rao Lower Bound (CRLB) provides a lower bound on the variance of an estimator. If the estimator variance is equal to the CRLB then this is the minimum variance an estimator can achieve. The CRLB for an estimator  $\theta$  is given by:

$$\text{Var}(\hat{\theta}(\mathbf{Y})) = -\frac{1}{\mathbb{E}\left[\frac{d^2 \ln f(\mathbf{Y}|\theta)}{d\theta^2}\right]} = \frac{2\sigma^4}{N} \quad (\text{C-20})$$

The CRLB is equal to the variance of the estimator. Therefore, the scattering variance estimator is a minimum variance unbiased estimator (MVUE). Let an estimator with a parameter  $\alpha$ :

$$\hat{\lambda}_1(\mathbf{Y}) = \frac{a}{NL} \sum_{i=1}^N Y_i^2 \quad (\text{C-21})$$

The MSE is given by:

$$MSE = \mathbb{E} \left[ \left( \hat{\lambda}_1(\mathbf{Y}) - \sigma^2 \right)^2 \right] = a^2 \mathbb{E} \left[ \left( \hat{\lambda}_1(\mathbf{Y}) \right)^2 \right] + \sigma^4 (1 - 2a) \quad (\text{C-22})$$

Replacing expectation by variance:

$$Var \left( \hat{\lambda}_1(\mathbf{Y}) \right) = \mathbb{E} \left[ \left( \hat{\lambda}_1(\mathbf{Y}) \right)^2 \right] - \sigma^4 \quad (\text{C-23})$$

The MSE can be written as follows:

$$MSE = a^2 \left( Var \left( \hat{\lambda}_1(\mathbf{Y}) \right) + \sigma^4 \right) + \sigma^4 (1 - 2a) = a^2 Var \left( \hat{\lambda}_1(\mathbf{Y}) \right) + \sigma^4 (1 - a)^2 \quad (\text{C-24})$$

Differentiate MSE with respect to  $\alpha$ :

$$\frac{dMSE}{da} = 0 \Rightarrow a = \frac{\sigma^4}{Var \left( \hat{\lambda}_1(\mathbf{Y}) \right) + \sigma^4} \quad (\text{C-25})$$

The value that minimizes MSE is:

$$a = \frac{N}{2 + N} \quad (\text{C-26})$$

Since the number of muon measurements  $N$  is considerably larger than 2,  $\alpha$  approaches 1.

This means that the scattering variance estimator also minimizes the MSE.